UNIVERSITY OF TRENTO - Italy
Department of Civil, Environmental and Mechanical Engineering

Doctoral School in Civil, Environmental and Mechanical Engineering

Curriculum “Modelling and Simulation” - XXXIII cycle - 2017/2021

Doctoral Thesis – February 2021

Osman Sayginer

Modelling and simulation of novel optoacoustic sensors for monitoring crack growth in pressure vessel steels

Supervisors

Prof. Oreste S. Bursi, University of Trento, Italy

Dr. Alessandro Chiasera, IFN-CNR Trento CSMFO Lab. Italy

To my family

If you want to find the secrets of the universe,

think in terms of energy, frequency and vibration.

Nikola Tesla

Acknowledgments

I would like to thank my supervisors Alessandro Chiasera, Maurizio Ferrari, and Oreste S. Bursi for their great attitude, friendly approach, and endless support throughout my doctoral career. Without their guidance, valuable scientific advice, and constructive feedback, this thesis would not be achieved as it is now.

I would like to thank all the colleagues from the University of Trento and IFN-CNR CSMFO Lab. Trento, Italy who have helped and supported me. In particular, I would like to thank Stefano Varas, Rocco di Filippo, Patrick Covi, Alessandro Carpentiero, Lidia Żur, Serena degli Avancini, Cristina Armellini, and Andrea Chiappini for their support.

Abstract

The acoustic emission technique is an effective way to acquire crack information from material bodies at the microscopic level. Monitoring of the acoustic emission events provides a deeper understanding regarding the structural health status of critical constructions such as bridges, railways, pipelines, pressure vessels, etc. Thanks to the acoustic emission monitoring systems, it is possible to avoid catastrophic events and save lives, time, and money. For this reason, efforts to develop new acoustic emission sensor technologies, as well as the use of current acoustic emission sensors in new research fields, will contribute to the limited literature sources.

Optical sensing systems provide good alternatives to the existing sensing technologies because of their wide range of detection bandwidths, adaptation to harsh environments, and low sensitivity to electromagnetic interference. For this reason, the first part of this thesis demonstrates an optoacoustic sensing methodology that enables the detection of acoustic emissions by optics. This sensing system consists of thin-film optical filters (TFOF) and an elastic microcavity layer. The sensing mechanism is similar to the Fabry Perot structures and it relies on resonance shifts of the cavity when there is a change in the cavity thickness similar to the Fabry Perot structures. Thus, the design, fabrication, and demonstration steps of a Fabry Perot elastic microcavity have been presented. Throughout the fabrication efforts, a new deposition protocol was developed. This deposition technique has enabled the deposition of TFOF on flexible substrates via the RF-sputtering technique. Thus, a new sensing configuration has been developed using flexible optical components.

In the second chapter, an optical sensing methodology based on tunable spectral filters and flexible optical components is introduced. The design, fabrication, realization, and characterization of a proof-of-concept optomechanical sensor have been presented. The design step includes optical, mechanical, and optoacoustic correlation simulations using the Transfer Matrix Method, finite element analysis, and analytical models. Moreover, the fabrication part includes multilayer deposition on silica and flexible substrates using the RF-Sputtering technique and integration of these optical components into a 3D-printed housing together with electronic components. Eventually, the performance evaluation of the optomechanical sensor has been carried out and the experimental results showed that the sensor resonance frequency is around 515 Hz and the sensor is capable of detecting static loadings from 50 Pa to 235 Pa values.

In the fourth chapter, seismic vulnerability analysis of a coupled Tank-Piping System has been performed using traditional acoustic emission sensors. Real-time performance evaluation of the pipeline as well as the structural health status of the critical parts were

monitored. As a result, deformation levels of each critical part were investigated, and the processing of acoustic emission signals provided a more in-depth view of damage level of the analyzed components.

Throughout the thesis, TFOFs are an integral part of this thesis. Therefore, both the design and simulation of TFOFs play a crucial role throughout this research work. The Transfer Matrix Method is used to simulate the optical performance of TFOFs.

Moreover, in the final chapter, an automated design framework is presented for the design of TFOFs using a nature-inspired machine learning approach called Genetic algorithm. This design approach enables the design of sophisticated geometric configurations with unique optical capabilities. Therefore, not only the improvement of sensor response but also the new ways in the development of novel optical systems are demonstrated in this final chapter.

GRAPHICAL ABSTRACT

Thesis

Chapter 1 *(Sensing Idea 1)* **[J1]**

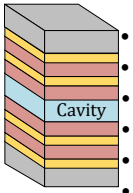

- *1-D Elastic Fabry Perot Microcavity*
- *SiO_2/TiO_2 multilayers*
- *PDMS microcavity*
- *Fabrication by RF Sputtering Deposition*
- *TMM modeling*
- *Testing under static loading*

Chapter 2 *(Sensing Idea 2)* **[J2],[C1],[C2]**

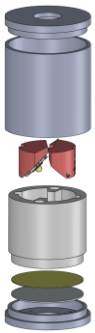

- *Development of Flexible Optical Components*
- *Proof of concept device*
- *TMM modeling*
- *Finite Element Simulations*
- *Testing under static loading*
- *Modal Analysis: Experiment and Simulation*
- *Optomechanical modelling*
- *515 Hz Resonance Frequency*
- *50 Pa to 235 Pa static response*

Chapter 3 *(Use of current sensors)* **[J3],[C3]**

- *Vulnerability investigation*
- *A realistic tank-piping system*
- *Hybrid simulation and acoustic emission*
- *Seismic and Monotonic synthetic ground motions*
- *Crack localization*
- *Determination of critical components*
- *Determination of Plasticity level of the system*

Chapter 4 *(Supplementary Topics)*

Modeling of Thin Film Optical Filters using Transfer Matrix Method

- *TMM: Transfer Matrix Method*
- *Mathematical Derivation of TMM*
- *Formulation of the TMM*

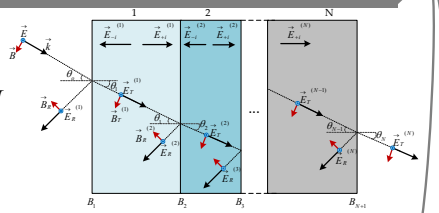

Design and Optimization of Thin Film Optical Filters

- *A novel design framework for optical filters*
- *Genetic Algorithm based optimization*
- *Formulation for 3 different design problems*
- *3 Optical design for Chapter2*
- *Development of an objective function for each design problem*

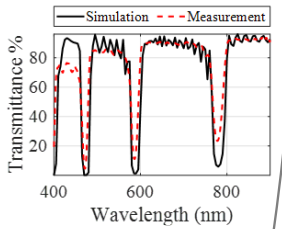

Design of a Resonant Fabry Perot Structure

- *An improved design for Chapter 1*
- *Finite Element simulations*
- *Structural dynamics simulations*
- *Resonance Frequency at 65 kHz*

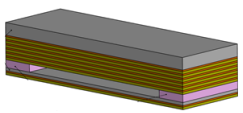

Frequency Tuning for the Sensor in Chapter 2

- *Frequency Tuning for Chapter 2*
- *Finite Element simulations*
- *Eigenfrequency analysis*
- *Frequency domain analysis*
- *Time domain analysis*
- *Resonance Frequency at 55 kHz*

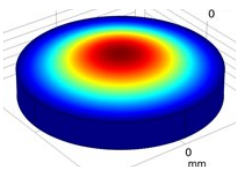

Publications

As a result of the research work that is conducted through doctorate, the following publication outcomes have been produced:

Journal publications

J1. **O. Sayginer**, A. Chiasera, L. Zur, S. Varas, L. T. N. Tran, C. Armellini, M. Ferrari, and O. S. Bursi, "Fabrication, Modelling and Assessment of Hybrid 1-D Elastic Fabry Perot Microcavity for Mechanical Sensing Applications" Ceram. Int., 2019.

J2. **O. Sayginer**, A. Chiasera, S. Varas, M. Ferrari, and O. S. Bursi, "Design, Fabrication and Assessment of an Optomechanical Sensor for Pressure and Vibration Detection using Flexible Glass Multilayers" *Opt. Mat., 2021*

J3. **O. Sayginer**, R. di Filippo, A. Lecoq, A. Marino, and O. S. Bursi, "Seismic Vulnerability Analysis of a Coupled Tank-Piping System by Means of Hybrid Simulation and Acoustic Emission" Exp. Tech., 2020.

Conference proceeding publications

C1. **O. Sayginer**, A. Chiasera, S. Varas, A. Lukowiak, M. Ferrari, and O. S. Bursi, "Design and fabrication of multilayer-driven optomechanical device for force and vibration sensing" International Society for Optics and Photonics SPIE, 2020.

C2. A. Chiasera and **O. Sayginer** et al., "Flexible photonics: RF-sputtering fabrication of glass-based systems operating under mechanical deformation conditions", International Society for Optics and Photonics SPIE, 2020.

C3. R. Filippo, G. Abbiati, **O. Sayginer**, O. S. Bursi, "Numerical metamodelling of a coupled tank-piping system for seismic fragility analysis with artificial waveforms", ASME PVP, 2019.

C4. **O. Sayginer**, C. Meroni, A. Chiasera, F. Scotognella, A. Lukowiak, . Speranza, S. Varas, L. Zur, G. C. Righini, R. Ramponi, O. Bursi, M. Ferrari, "Er3+ 1-D photonic bandgap structure for photonic band edge assisted spontaneous emission enhancement", 1st International Conference on Dielectric Photonic Devices and Systems Beyond Visible, Bari, Italy, 1-2 October 2018

Contents

List of Abbreviations			
1DPC	*1-D photonic crystal*	*NIR*	*Near-infrared*
AE	*Acoustic emission*	*NS*	*Numerical substructure*
AET	*Acoustic emission technique*	*OMS*	*Optomechanical sensor*
AFM	*Atomic force microscopy*	*PDMS*	*Polydimethylsiloxane*
BFJ	*Bolted flange joints*	*PMMA*	*Polymethyl methacrylate*
EMC	*Elastic microcavity*	*PS*	*Physical substructure*
FE	*Finite element*	*PSHA*	*Probabilistic seismic hazard analysis*
FEM	*Finite element Method*	*PZT*	*Piezoelectric*
FFT	*Fast Fourier transform*	*RF*	*Radiofrequency*
FPI	*Fabry Perot interferometer*	*SDoF*	*Single degree of freedom*
GA	*Genetic algorithm*	*SHM*	*Structural health monitoring*
HS	*Hybrid simulation*	*TFOF*	*Thin-film optical filters*
LoC	*Loss of containment*	*TMM*	*Transfer matrix method*
NDT	*Non-destructive testing*	*UV*	*Ultraviolet*

Introduction

Background & Motivation

The acoustic emission technique (AET) is a method of listening for mechanical changes in material structures at a microscopic level. In other words, when an irreversible deformation occurs through a solid material domain, such as a crack growth, deformation energy releases as a form of elastic wave propagation (called acoustic emission (AE)) through the material body. Each crack formation acts as a signal source and shows a transient-signal behavior. Depending on the signal-form of an elastic-wave, further information can be extracted regarding the health status of the material, for instance, amount of level deformation, crack location, etc. Thus, AET is also known as passive non-destructive-testing-technique (NDT). With the use of AE systems, the real-time crack evolution of structures and, thus the deformation level can be monitored. The use of AET for the purpose of crack-growth on a civil structure is commonly called structural health monitoring (SHM) [1].

Some advantages of AET play an important role in the increase of its popularity. Mainly, the AET is capable of providing simultaneous information on crack growth in a structure without interrupting the process of the structure. Thus, it allows us to track the lifetime, material condition as well as to observe the design-originated behavior of a structure. In addition to that, post-processing of the AE signals enables the detection of the crack-source location through the structure [1]–[3]. As a result, AE has a broad spectrum of application areas such as; civil structures, seismology, composite materials, railways, mines, pressure vessels, etc. [2], [4]–[7].

Traveling acoustic emission signals through a material body can be detected by AE sensors. The most common type of acoustic sensors relies on piezoelectric (PZT) transducers. PZT sensors show good performance for AE signal detection with desired features such as low cost, high sensitivity, wide detection bandwidth, and simplicity for applications [8], [9]. For these reasons, PZT sensors have been an integral part of AE detection since they were discovered [10], [11].

Alternatively, an increasing development trend in recent years in the field of optical materials, fiber optics, and photonics has shifted the interest in optical sensors [12], [13]. In particular, for acoustic wave detection purposes, optical sensing techniques offer some advantages; which are wide detection bandwidths, higher signal-to-noise-ratio comparing to PZT sensors, and immunity to electromagnetic interference [14]. Thus, the development of an optoacoustic sensor plays an important role in contributing to different research fields such as structural health monitoring, biomedical imaging, and noncontact measurements.

In particular, a Fabry Perot interferometer (FPI) can be a good candidate for detection of the acoustic vibrations. More precisely, FPI is an optical sensing technique that involves the interaction and interference of multiple beams through two optical plates that are separated from each other with a cavity layer. The sharper fringe feature of the FPI improves both the accuracy and resolution of the measurements [15], [16], thus, FPI is a good candidate for acoustic sensing purposes. Several studies have studied the FPI for acoustic sensing purposes. Some of the selected studies can be summarized as follows.

Thomson et al. [17] demonstrated the visualization of acoustic surface vibration fields. They showed the basic operation of an FPI system and presented a formulation to calculate detection sensitivity.

Beard et al. [18] proposed a Polyethylene terephthalate thin-film sensing element acting as an FPI. Therefore, they realized their idea and the sensing element was tested to detect the pressure waves in water. Some metrics regarding the sensing element, such as transfer function, sensitivity, and frequency response were shown.

Zhang et al. [19] showed an FPI structure where a polymeric microcavity made by Parylene C was sandwiched by two dichroic mirrors. They demonstrated that that structure was useful for biomedical imaging purposes.

Morris et al. [20] showed an FPI on a fiber-integrated ultrasonic hydrophone for real-time measurement of acoustic pressure and temperature too.

Last but not least, Wissmeyer et al. [14] presented an extended review article that summarizes the current status of optical ultrasound sensors and their future potential; in particular, the field of biomedical imaging was examined in depth.

The optical plates of FPIs are the important components needed to define the sensing capabilities. The optical plates are expected to have special coatings that can enhance the reflectance of an FPI structure at the desired spectrum bands. Hence, 1-D photonic crystal (1DPC), also known as Bragg reflector can be used for filtering light. More precisely, 1DPC is a photonic element, that contains alternating material layers with different refractive indices. Thus, the periodic distribution of the materials acts as a bandpass filter and the spectral behavior of the light can be tuned by the designing of the 1DPC layers [21], [22].

On the one hand, for the design of a Bragg reflector, the important design parameters are the refractive indices of the 1DPCs, the thicknesses of the 1DPCs, and the number of 1DPC layers. Using these design parameters, the spectral response of a Bragg reflector can be simulated using the transfer matrix method (TMM) [23]–[26]. TMM is an effective route to calculate the propagation of electromagnetic waves in different dielectric media.

On the other hand, a proper fabrication protocol is important to fabricate a Bragg reflector that satisfies the design parameters. Some of the widely used fabrication methods for 1DPCs are sol-gel deposition [27], electron-beam evaporation [28], ion implantation [29], and radiofrequency (RF) sputtering [30]. The important factors for the fabrication process are the control of the thickness and material homogeneity and the reproducibility [31]. Therefore, the fabrication process is required to be reliable, and flexible enough to satisfy requirements of structures based on different materials and operating in different spectral ranges. If the refractive index change between deposited layers is relatively low, then the control of the deposition rate becomes an important parameter for the fabrication. For this reason, monitoring the deposition rate plays an important role in the thorough deposition process. Moreover, to obtain well-tailored, uniform systems, it is necessary both precision and sensitivy in design [32], [33].

By taking into account all of this background information, the first chapter of this thesis presents the design, fabrication, and evaluation of an FBI with an elastic microcavity (EMC). In particular, an EMC layer was fabricated by Polydimethylsiloxane (PDMS) and was sandwiched by two Bragg reflectors. The purpose of adding an elastic cavity layer was to observe most of the deformation through the cavity layer rather than the rigid Bragg reflectors. Thus, two Bragg reflectors were fabricated using the RF sputtering technique. In order to integrate an EMC in between two Bragg reflectors and perform the parallel alignment, a fabrication protocol was developed. A simulation study was also performed using TMM, for both Bragg reflectors and the FPI sample. The displacement of the cavity thickness under loading conditions and its effect on the optical response were investigated. In order to do that, the sample was compressed via a specially designed apparatus. The change in the optical spectrum was measured using a spectrophotometer.

The results have shown that the optical response of the structure was not only influenced by the change in the cavity thickness but also the refractive index of the PDMS. For this reason, a new structure was designed and presented in Subsection 4.3. In the new design configuration, the cavity layer was made by air and the structure was designed as a both-ends-fixed beam. This new configuration aimed to avoid the change in the refractive index under loading and also to obtain a resonant structure that works at desired detection frequencies. Thus, a finite element model (FE) model was developed using COMSOL

Multiphysics [34] and the dynamic behavior of the structure was determined via simulation work.

In order to fabricate the new both-end-fixed design, the development of a suitable fabrication protocol was crucial. In particular, having a flexible sample that can operate without damaging the thin-film layer was required. As a result of the development on this matter, an innovative fabrication protocol was developed which enables the deposition of optical thin films on flexible substrates easily and cost-effectively using the current RF sputtering technique.

The development of flexible optical components brings some advantages over the traditional optical material technologies as well as optical device implementations. More precisely, the fragility of current glass-ceramic based optical components brings some difficulties for the implementation of optical components on thin and deformable structures such as membranes, beams, and cantilevers. Thus, the development of new fabrication protocols for optical materials, in particular flexible optical components, offers new device developments for mechanical sensing applications [35]. For instance: gratings, channel waveguides, also solar cells, and protective coatings can offer unique performance characteristics as compared to their rigid classical structures [36].

In addition, as a consequence of an increasing trend in flexible electronics, adding mechanical flexibility to the optical components became a popular subject in the field of optics and photonics. Moreover, the integration of optical structures on deformable polymer substrates has given birth to flexible photonics, a field that has rapidly emerged in recent years to the forefront of photonics. Owing to the addition of mechanical flexibility to planar photonic structures, the wide range of application acquired increasing popularity. To date, flexible planar photonic devices were almost exclusively fabricated using polymeric substrates, which do not offer high refractive indices that are necessary for strong optical confinement. It is also worthy to note that Corning [37] and Schott [38] have recently presented ultra-thin flexible glasses, therefore, there is a chance of future development for an all-glass flexible photonics component that should operate in several deformation conditions, i.e. bending, folding, rolling, twisting, stretching, and compression [39].

Taking advantage of the developments in the fabrication of flexible optical structures, the second chapter of the thesis presents a new sensing method based on tunable spectral filters by using flexible optical components. In particular, the sensing methodology relies on the optical interaction between two multilayer components: one of the components is called reflector while the other one, filter. The reflector is a flexible Bragg reflector that is attached to a single-degree-of-freedom (SDoF) contact-layer for the purpose of one-directional reflection and mechanical tunability of the contact-layer without making a compromise on the reflection spectrum. A full-spectral-width light source in the visible range illuminates the reflector. The reflected spectrum is, then, filtered by a filter and the final transmitted light is detected by a photodiode. In other words, the overlapping area of the reflectance and transmittance spectrum defines the area that will be detected by a photodiode. Based on this sensing methodology a cost-effective and easily implementable proof-of-concept device was demonstrated. The device was tested under static and dynamic conditions. It was found that the device can be used for pressure and vibration detection. In addition to that, the optomechanical sensor response was also investigated. An optomechanical calculation schema was developed that couples the mechanical response of the structure together with the optical response. Therefore, the optomechanical response of the device can be predicted.

The sensing performance of the given optomechanical device is strongly dependent on the membrane geometry and the spectral behavior of the optical components. On the one hand, the membrane influences the dynamic behavior of the device. Radius, thickness, and the stiffness of the membrane are the fundamental parameters to define the resonance frequency, thus, the dynamic response of the sensor. In addition to the sensor design given in Chapter 2, a further design is presented in Chapter 4.4 to increase the working frequency of the sensor by redesigning the membrane geometry.

On the other hand, the spectral response of the two optical components defines the final output signal of the device. For this reason, a proper methodology to design the optical components including the thin-film composition, not only improve sensor response but also contribute to the design of novel optical structures involving the metamaterial concept. In short, the metamaterial is the concept of functionally designed material sub-structures with superior properties that performs beyond the existing materials [40]. This concept relies on the manipulation of the wave-phenomenon systems by engineering the sub-wavelength material topologies. The metamaterial topologies can be distributed in space as 1D (Bragg mirrors), 2D (metasurfaces), and 3D. Furthermore, most of these topologies are designed as periodic structures by intuition. However, as also in this thesis, recent advances in computational design algorithms (inverse design and topology optimization) enable the performance improvement of the periodic structures as well it offers the design of exotic non-periodic topologies [41].

In this context, an automated design framework was developed for a single Bragg reflector, as well as for two Bragg reflectors in interaction considering the geometric optics. More precisely, to find the best combination of the design parameters, design variables such as; layer thickness, the number of layers, and the refractive index of each material layer, a TMM-integrated Genetic Algorithm was employed. The details of this study are presented in Subsection 4.2.

The third chapter of the thesis shows seismic vulnerability analysis of a coupled tank-piping system using traditional PZT acoustic emission sensors for the detection of most vulnerable components, i.e., pipe bends and welding points. Determination of the critical components is an important step to prevent leakage events. A methodology based on a stochastic seismic ground motion model, hybrid simulation, and acoustic emission is presented. The seismic model can generate synthetic ground motions coherent with site-specific analysis. In a greater detail, the coupled tank-piping system is composed of a steel slender tank, i.e., the numerical substructure, and a piping network connected through a bolted flange joint, i.e., the physical substructure. To monitor the seismic performance of the pipeline and harness the use of current PZT sensor technology, acoustic emission sensors are placed through the pipeline. Thus, real-time acoustic emission signals of the system under study are acquired using acoustic emission sensors. Deformation levels of each critical component were investigated, and the processing of acoustic emission signals provided a more in-depth view of the damage of the analyzed components.

Scope

This thesis focuses on the development of an optical sensing technique for the detection of elastic waves propagating in a solid medium for structural health monitoring applications. More precisely, the final goal is to demonstrate optomechanical modeling, design, and simulation approaches for the detections of acoustic emission signals from a crack release through a piping system. However, considering the complexity and the wide extent of the research field, it is necessary to draw the borders of the content and to define the scope.

On one hand, an acoustic emission signal content includes an envelope of high-frequency components that are typically in the ultrasound range, i.e. above 20 kHz. The high-frequency nature of an acoustic emission signal shows some challenges in sampling, processing, and visualization. Independently from a sensing element, specially designed electronic equipment, such as; amplifier, computer software, etc. is also necessary for complete monitoring. Due to the fact that these challenges, the sensor fabrication and realization parts of this thesis are limited to lower frequency devices. Nevertheless, modeling and design approaches are demonstrated for higher frequency applications. On the other hand, depending on the material properties of a propagation medium, an elastic wave can travel in different forms such as pressure waves, shear waves, Rayleigh waves, Love waves, and Lamb waves. In addition, an acoustic signal can also change its waveform properties through a test structure and an acoustic emission sensor due to an impedance mismatch. Since the elastic wave propagation through different media is itself an independent research subject, the scope of this thesis is limited for the sensor structure only, by considering Rayleigh wave-like periodic surface excitations.

The first chapter of the thesis demonstrates a sensing technique using a Fabry Perot interferometry approach with an elastic microcavity made by PDMS and sandwiched by two Bragg reflectors. In this work, only the experimental investigation of the static behavior of the structure was shown. In the following part, a resonant structure with the same sensing approach was designed and simulated for acoustic emission applications. The design frequency was chosen for 50 kHz and above frequency values.

Throughout the research journey of the thesis, an innovative fabrication approach was discovered for the deposition of thin-film coatings on flexible substrates. Therefore, the sensing approach was evolved into a new sensing methodology using flexible optical components.

In the second chapter of the thesis, a new sensing approach based on tunable spectral filters is demonstrated. Similar to the first chapter, modeling, simulation, and design stages were also performed on this new sensing approach. The designed components were also fabricated and a proof-of-concept device was demonstrated. This device was tested under loading conditions and also impact test. The working frequency of the device was found around 515 Hz. Though the sensor frequency is very low with respect to the acoustic emission applications, further modeling and simulation studies thar are given in Chapter 4.4, demonstrates the possibility to adopt this technique for higher frequencies.

The third chapter of the thesis shows seismic vulnerability analysis of a coupled tank-piping system using traditional PZT acoustic emission sensors for the detection of most vulnerable components.

The fourth chapter presents supplementary topics that covers modelling of thin-film optical filters, a design framework for thin-film optical filters and two additional topics. They demonstrate further design and simulation studies that serve Chapter 1 and Chapter 2, respectively.

Structure of the thesis

The content of the thesis is composed of four chapters. The first three chapters are intended to be published as journal articles. The fourth chapter presents four supplementaries to cover the thesis content more in depth. They are preceeded by a Section Introduction and followed by a closing Section that contains the Subsections Summary, Conclusions and Future perspectives.

- Chapter 1 presents a sensing scheme based on Fabry Perot Interferometry using thin-film optical filters. More precisely, a proof-of-concept sample was fabricated and simulated using an elastic microcavity made by a PDMS layer. The displacement in the thickness of the cavity layer due to static loadings was determined experimentally, as a change in the optical spectrum through spectrophotometer measurements. The results of this research work were published in Ceramics International with the title: *Fabrication, Modelling, and Assessment of Hybrid 1-D Elastic Fabry Perot Microcavity for Mechanical Sensing Applications.*
- Chapter 2 presents a new optical sensing approach based tunable spectral filter using flexible optical components. This chapter presents an extended work in analytical modeling, simulation, design, and characterization of a proof-of-concept sensor. The content of the study also includes the determination of the static and also dynamic investigation of the sensor response. The result of this research work was submitted in Optical Materials with the title: *Design, Fabrication, and Assessment of an Optomechanical Sensor for Pressure and Vibration Detection using Flexible Glass Multilayers*.
- Chapter 3 presents the seismic vulnerability analysis of a coupled tank-piping system using traditional PZT acoustic emission sensors for the detection of most vulnerable components. A methodology based on a stochastic seismic ground motion model, hybrid simulation, and acoustic emission is presented. The real-time acoustic emission monitoring of the tank-piping system was presented. Deformation levels of each vulnerable component were investigated, and the processing of acoustic emission signals provided a more in-depth view of the damage level of the analyzed components. The result of this research work was published in Experimental Techniques with the title: *Seismic Vulnerability Analysis of a Coupled Tank-Piping System by Means of Hybrid Simulation and Acoustic Emission*.
- Chapter 4 includes supplementary topics for the development of an optical sensor for force and vibration detection. The topics cover what follows: i) The theory and the background information regarding the transfer matrix method for the modelling of thin-film optical filters. ii) A design and optimization framework for thin-film optical filters to tailor the optical response of the optical structures using the Genetic algorithm. iii) Design and simulation of a sensor structure based on the idea in Chapter 1 for vibration detection above 50 kHz

values. iv) Design and simulation of a sensor structure based on the idea in Chapter 2 for vibration detection above 50 kHz values.

References

[1] C. U. Grosse and M. Ohtsu, Acoustic emission testing. Springer Science \& Business Media, 2008.

[2] A. Nair and C. S. Cai, “Acoustic emission monitoring of bridges: Review and case studies,” Eng. Struct., vol. 32, no. 6, pp. 1704–1714, 2010.

[3] K. Ohno and M. Ohtsu, “Crack classification in concrete based on acoustic emission,” Constr. Build. Mater., vol. 24, no. 12, pp. 2339–2346, 2010.

[4] R. Di Filippo, G. Abbiati, O. Sayginer, P. Covi, O. S. Bursi, and F. Paolacci, “Numerical surrogate model of a coupled tank-piping system for seismic fragility analysis with synthetic ground motions,” in American Society of Mechanical Engineers, Pressure Vessels and Piping Division (Publication) PVP, 2019, vol. 8.

[5] O. Sayginer, R. di Filippo, A. Lecoq, A. Marino, and O. S. Bursi, “Seismic Vulnerability Analysis of a Coupled Tank-Piping System by Means of Hybrid Simulation and Acoustic Emission,” Exp. Tech., 2020.

[6] G. Manthei and K. Plenkers, “Review on in situ acoustic emission monitoring in the context of structural health monitoring in mines,” Appl. Sci., vol. 8, no. 9, 2018.

[7] C. Barile, C. Casavola, G. Pappalettera, and V. P. Kannan, “Application of different acoustic emission descriptors in damage assessment of fiber reinforced plastics: A comprehensive review,” Eng. Fract. Mech., p. 107083, 2020.

[8] L. Zhang, H. Yalcinkaya, and D. Ozevin, “Sensors and Actuators A : Physical Numerical approach to absolute calibration of piezoelectric acoustic emission sensors using multiphysics simulations,” vol. 256, pp. 12–23, 2017.

[9] K. Marschall, “Processing Technology In-Process Monitoring with Piezoelectric Sensors,” vol. 44, pp. 345–352, 1994.

[10] W. P. Mason, H. J. Mcskimin, and W. Shockley, “Ultrasonic Observation of Twinning in Tin,” Phys. Rev., vol. 73, no. 10, pp. 1213–1214, May 1948.

[11] N. Thompson and D. J. Millard, “XXXVIII. Twin formation, in cadmium,” London, Edinburgh, Dublin Philos. Mag. J. Sci., vol. 43, no. 339, pp. 422–440, 1952.

[12] N. Sabri, S. A. Aljunid, M. S. Salim, R. B. Ahmad, and R. Kamaruddin, “Toward Optical Sensors: Review and Applications,” J. Phys. Conf. Ser., vol. 423, p. 12064, Apr. 2013.

[13] A. Theodosiou and K. Kalli, “Recent trends and advances of fibre Bragg grating sensors in CYTOP polymer optical fibres,” Opt. Fiber Technol., vol. 54, p. 102079, 2020.

[14] G. Wissmeyer, M. A. Pleitez, A. Rosenthal, and V. Ntziachristos, “Looking at sound: optoacoustics with all-optical ultrasound detection,” Light Sci. Appl., vol. 7, no. 1, p. 53, 2018.

[15] A. Macleod, Thin-Film Optical Filters, vol. 53, no. 4. 2012.

[16] J. H. Z. Christi K. Madsen, Optical Filter Design and Analysis. .

[17] J. K. Thomson, H. K. Wickramasinghe, and E. A. Ash, “A Fabry-Perot acoustic surface vibration detector - Application to acoustic holography,” J. Phys. D. Appl. Phys., vol. 6, no. 6, pp. 677–687, 1973.

[18] P. C. Beard, “Transduction mechanisms of the Fabry-Perot polymer film sensing concept for wideband ultrasound detection,” IEEE Trans. Ultrason. Ferroelectr. Freq. Control, vol. 46, no. 6, pp. 1575–1582, 1999.

[19] E. Zhang, J. Laufer, and P. Beard, “Backward-mode multiwavelength photoacoustic scanner using a planar Fabry-Perot polymer film ultrasound sensor,” Appl. Opt., vol. 47, no. 4, pp. 561–577, 2008.

[20] P. Morris, A. Hurrell, A. Shaw, E. Zhang, and P. Beard, “A Fabry–Pérot fiber-optic ultrasonic hydrophone for the simultaneous measurement of temperature and acoustic pressure,” J. Acoust. Soc. Am., vol. 125, no. 6, pp. 3611–3622, 2009.

[21] M. Bellingeri, A. Chiasera, I. Kriegel, and F. Scotognella, “Optical properties of periodic, quasi-periodic, and disordered one-dimensional photonic structures,” Opt. Mater. (Amst)., vol. 72, pp. 403–421, 2017.

[22] K. O. Hill and G. Meltz, “Fiber Bragg grating technology fundamentals and overview,” J. Light. Technol., vol. 15, no. 8, pp. 1263–1276, Aug. 1997.

[23] S. Larouche and L. Martinu, “OpenFilters: open-source software for the design, optimization, and synthesis of optical filters,” Appl. Opt., vol. 47, no. 13, p. C219, 2008.

[24] D. M. Topasna and G. A. Topasna, “Numerical modeling of thin film optical

filters," Educ. Train. Opt. Photonics, no. October, p. EP5, 2009.

[25] G. F. Burkhard, E. T. Hoke, and M. D. McGehee, "Accounting for Interference, Scattering, and Electrode Absorption to Make Accurate Internal Quantum Efficiency Measurements in Organic and Other Thin Solar Cells," Adv. Mater., vol. 22, no. 30, pp. 3293–3297, Aug. 2010.

[26] Y. G. Boucher, J. Le Rouzo, I. Ribet-Mohamed, and R. Haïdar, "Modified form birefringence in periodic multilayer structures including uniaxial anisotropic materials," J. Opt. Soc. Am. B, vol. 25, no. 5, pp. 777–784, May 2008.

[27] Y. Li, L. M. Fortes, A. Chiappini, M. Ferrari, and R. M. Almeida, "High quality factor Er-doped Fabry-perot microcavities by sol-gel processing," J. Phys. D. Appl. Phys., vol. 42, no. 20, 2009.

[28] G. Ma, J. Shen, Z. Zhang, Z. Hua, and S. H. Tang, "Ultrafast all-optical switching in one-dimensional photonic crystal with two defects," Opt. Express, vol. 14, no. 2, pp. 858–865, Jan. 2006.

[29] H. Rigneault et al., "Spontaneous emission into planar multi-dielectric microcavities: Theoretical and experimental analysis of rare earth ion radiations," Opt. Mater. (Amst)., vol. 11, no. 2–3, pp. 167–180, Jan. 1999.

[30] S. Valligatla et al., "High quality factor 1-D Er^3+-activated dielectric microcavity fabricated by RF-sputtering," Opt. Express, vol. 20, no. 19, p. 21214, Sep. 2012.

[31] A. Chiasera et al., "Hybrid 1-D dielectric microcavity: Fabrication and spectroscopic assessment of glass-based sub-wavelength structures," Ceram. Int., vol. 41, no. 6, pp. 7429–7433, 2015.

[32] T. P. Burg et al., "Weighing of biomolecules, single cells and single nanoparticles in fluid," Nature, vol. 446, no. 7139, pp. 1066–1069, 2007.

[33] R. Raiteri and H. J. Butt, "Measuring electrochemically induced surface stress with an atomic force microscope," J. Phys. Chem., vol. 99, no. 43, pp. 15728–15732, 1995.

[34] "COMSOL Multiphysics® v. 5.4. www.comsol.com. COMSOL AB, Stockholm, Sweden." Stockholm, Sweden.

[35] O. Sayginer, A. Chiasera, S. Varas, A. Lukowiak, M. Ferrari, and O. S. Bursi, "Design and fabrication of multilayer-driven optomechanical device for force and vibration sensing," in Fiber Lasers and Glass Photonics: Materials through

Applications II, 2020, vol. 11357, pp. 328–337.

[36] H. Sun and X. Li, “Recent Advances on III-Nitride Nanowire Light Emitters on Foreign Substrates – Toward Flexible Photonics,” Phys. status solidi, vol. 216, no. 2, p. 1800420, Oct. 2018.

[37] “Corning Willow Glass Laminates | Ultra-thin, Bendable, Flexible Glass | Corning.” [Online]. Available: https://www.corning.com/worldwide/en/innovation/corning-emerging-innovations/corning-willow-glass.html. [Accessed: 09-Jan-2021].

[38] “Let the future evolve in your hands - Schott Innovation.” [Online]. Available: https://www.us.schott.com/innovation/ultrathinglass/. [Accessed: 09-Jan-2021].

[39] D. W. Mohammed, R. Waddingham, A. J. Flewitt, K. A. Sierros, J. Bowen, and S. N. Kukureka, “Mechanical properties of amorphous indium--gallium--zinc oxide thin films on compliant substrates for flexible optoelectronic devices,” Thin Solid Films, vol. 594, pp. 197–204, 2015.

[40] M. Kadic, G. W. Milton, M. van Hecke, and M. Wegener, “3D metamaterials,” Nat. Rev. Phys., vol. 1, no. 3, pp. 198–210, 2019.

[41] S. Molesky, Z. Lin, A. Y. Piggott, W. Jin, J. Vucković, and A. W. Rodriguez, “Inverse design in nanophotonics,” Nat. Photonics, vol. 12, no. 11, pp. 659–670, 2018.

Chapter 1

1 Fabrication, Modelling, and Assessment of Hybrid 1-D Elastic Fabry Perot Microcavity for Mechanical Sensing Applications

Abstract

1-D multilayer dielectric films consisting of seven pairs of SiO_2 and TiO_2 alternating layers are deposited on a SiO_2 substrate using the radio frequency sputtering technique. The thicknesses of the film layers are chosen to reflect the visible radiation around 650 nm. An elastic microcavity layer made of Polydimethylsiloxane was sandwiched between two Bragg reflectors. A fabrication process was then developed for elastic microcavity in order to tailor the thickness, establish the surface planarity, and increase the reproducibility of the samples. Optical transmittance of the single Bragg reflector and the microcavity were both simulated and measured. A comparison between measurement data and Transfer Matrix Method calculations shows a favorable correlation. Furthermore, in order to assess the suitability of the microcavity as a force sensor, transmittance measurements were carried out as a function of the applied forces. The change in the elastic microcavity thickness due to applied forces resulted in cavity resonance peak shifts proportional to the applied forces.

1.1 Introduction

Force and displacement sensors are widely used devices in many fields such as the aerospace, robotics, and automotive industry. These sensors aim to detect the distance between two reference points. Then, the displacement and the magnitudes of the subjected forces can be derived using the distance information. Most sensors in the market today rely on one of several sensing approaches, which vary depending on their principles of physics, such as optical beam, piezoelectricity, capacitance, resistivity, and electron tunneling [1].

Recent developments in laser and photonics technologies have opened new horizons for the traditional sensors in the market. High sensitivity and accuracy, low power consumption, immunity to electromagnetic interference, chemical resistance, and operation at high temperatures are only some of the advantages of these optical sensors [2]. However, fabrication difficulties, alignment problems, and mechanical fragility issues are some of the challenges which need to be addressed carefully while designing an optical system.

1-D photonic crystal (1DPC) is a photonic component, composed of layers of alternating material layers with different refractive indices. The periodicity of the materials behaves as a bandpass filter and the incident light spectrum can be tailored through the different configurations of the 1DPC layers [3]. The structures, consisting of the layers of 1DPC, are also known as Bragg reflectors. In order to design a Bragg reflector for a light filtering purpose in the desired spectral range, important design parameters are the refractive indices of the 1DPCs, the thicknesses of the 1DPCs, and the number of 1DPC layers. In addition, another requirement to fabricate a Bragg reflector that satisfies the design parameters is a proper fabrication approach.

There are several fabrication methods widely used for 1DPCs such as ion implantation [4], sol-gel deposition [5], electron-beam evaporation [6], and radiofrequency (RF) sputtering [7, 8]. The key points for the fabrication are to control the thickness and material homogeneity and to have reproducibility [9]. For this reason, the fabrication process is required to be reliable, and to flexible enough to adapt the needs and requirements of structures based on different materials and operating in various spectral ranges. When refractive index change between deposited layers is relatively low, control of the deposition rate becomes an important parameter. For this reason, monitoring the deposition rate plays an important role in the deposition process. Moreover, in order to obtain well-tailored, uniform systems, it is also necessary that the design be precise and sensitive [10, 11]. The optical response of a fabricated system strongly depends on its material properties.

Among the different materials, the performance of oxide-based dielectric materials is a well-known substance for Bragg reflectors thanks to their high transparency from the ultraviolet (UV) to the near-infrared (NIR) wavelengths, as well as their resistance to thermal alteration, corrosion, and radiation-induced modifications [10, 12].

Two Bragg reflectors and an elastic medium between these reflectors can mimic a Fabry Perot interferometer on the microscale. An elastic layer can act as a cavity and creates resonance peaks through the optical spectra. Thus, a change in the optical path of the cavity layer can result in a change in the intensity and shifts on the cavity peaks.

In this paper, we have designed, simulated, and fabricated a Bragg reflector consisting of multilayers of SiO_2 and TiO_2 thin layers using the RF sputtering technique. A fabrication scheme was developed for a micron-scale thick, Polydimethylsiloxane (PDMS) elastic cavity layer. The elastic microcavity (EMC) was sandwiched by two Bragg reflectors. The optical transmittance measurements were performed for both the single Bragg reflector and the sandwich sample. A Transfer Matrix Method (TMM) [13] based on simulations were developed and computed.

In order to investigate the mechanical response of the EMC for potential sensing applications, the sample was tested under various compression forces. The change in the optical response due to the different loadings is reported. It was found that the increase in the magnitude of the applied force resulted in a shift to a higher wavelength and increased the intensity of the optical response.

1.2 Fabrication details

1.2.1 Bragg Reflector Fabrication

The Bragg reflector was designed using SiO_2 and TiO_2 alternating layers with an optical thickness that optimized to operate at a wavelength of 650 nm. The layer thicknesses were defined according to the quarter wave design approach. Thus, Thicknesses of SiO_2 and TiO_2 layers were chosen as 105 nm and 65 nm respectively. A TMM based on simulation model was created by considering the wavelength-dependent refractive indices. In order to maximize the reflection while keeping the number of layers as minimum as possible, stack numbers were optimized via TMM simulations. Reduction in the number of stack layers is also beneficial to improve the fabrication quality and enhance the speed of the deposition process. The Bragg reflectors were fabricated by RF sputtering technique. The silica substrates were physically cleaned at first and then cleaned inside of the multi-target RF sputtering chamber for 30 minutes while heating up the temperature to 120 °C. The deposition was performed using silica and titania guns with an equal target size of 5 x 15 cm^2. Throughout the deposition, Argon pressure was kept at 5.4×10^{-3} mbar while the plasma power of the silica and titania targets were 150W and 130 W respectively without any reflected power. The chamber temperature was kept stable while the sample holder was reached at 30 °C maximum. The deposition rates were monitored for two targets separately using two quartz microbalances from Veeco instruments (Model number: QM311). The effective thickness of the final resolution was derived as 1 Å from the quartz microbalances. The deposition process was completed in 12 hours. A more detailed fabrication protocol can be found in [9].

1.2.2 Elastic microcavity fabrication

Sylgard 184 Silicone Elastomer was mixed with the curing agent at 10:1 weight ratio for 5 minutes and kept at room temperature for 30 minutes to avoid the air bubbles in the mixture. One drop of PDMS mixture about 6 mg was placed on top of the 25×25 mm^2 Bragg reflector surface by contacting to the TiO_2 layer faces as it is shown in Fig. 1.1. Two Bragg reflectors were mechanically pressed for 15 minutes at room temperature by placing 500 gr weight on top of the samples. The aim of the applied weight was to tailor the thickness of the PDMS and to align two Bragg's parallelly. The sample under applied weight was cured at 80 °C for 30 minutes. At the end of the curing procedure, residual PDMS was scratched from the edges and the sample was cleaned with ethanol and optical tissue.

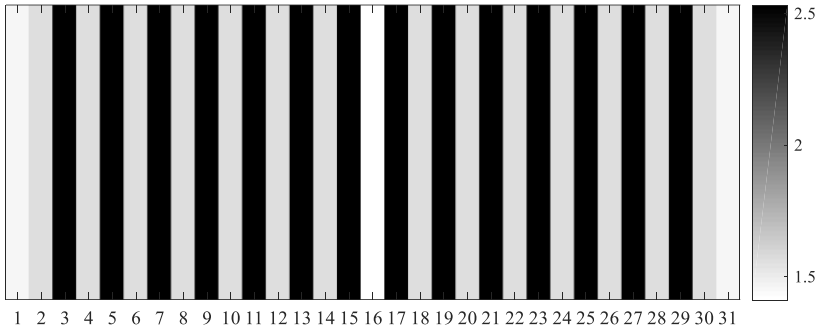

Figure 1.1 Refractive index distribution of the sandwich sample at 650 nm. (1st and 31st layers: silica substrates, 16th layer: PDMS, black layers: TiO_2 and grey layers: SiO_2.)

1.2.3 Optical characterization and transfer matrix calculations

Optical characterizations of the single Bragg reflector and the microcavity were performed using Varian Cary mod.5000 double-beam spectrophotometer in the visible range from 400 nm to 900 nm with a resolution of 2 nm. The TMM simulation model was employed with zero-degree incident angle and wavelength dependent refractive indices were used which taken from the measurements [14,15].

1.3 Results

We fabricated two Bragg reflectors, each one consisting of seven couples of SiO_2 and TiO_2 layers, using multitarget RF sputtering. An elastic microcavity layer made of PDMS was placed between the two Bragg reflectors like a sandwich. The sandwich structure was then subjected to different loadings with a specially designed apparatus.

In Fig. 1.2, comparison of the transmittance measurement and the results of the TMM simulation for the Bragg reflectors are presented.

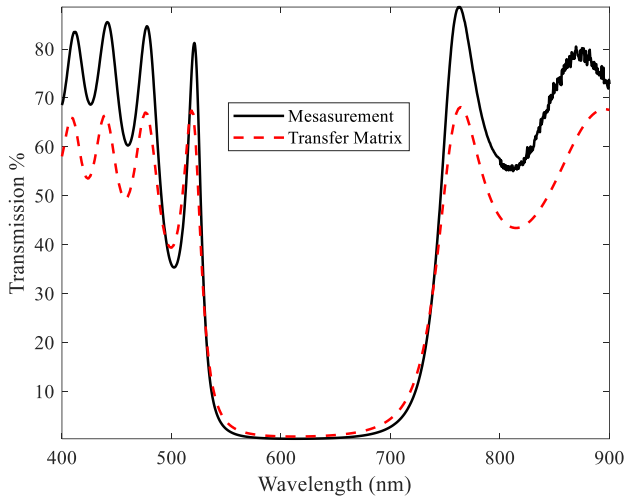

Figure 1.2 Transmission spectrum of the Bragg reflector consisting of seven couples of SiO_2-TiO_2 layers plotted in the black curve. The TMM simulation of the single Bragg reflector is plotted in the red dashed curve.

A similar spectra measurement for the sandwich sample was performed. The TMM model was modified for the sandwich sample. The thickness of the PDMS layer was estimated from the cavity oscillations on the transmission spectra using Eq. (1.1), then plugged into the TMM model.

$$\Delta\lambda = \frac{\lambda_0^2}{\ell 2 n_g \cos\theta + \lambda_0} \approx \frac{\lambda_0^2}{\ell 2 n_g \cos\theta} \tag{1.1}$$

where θ is the incident angle, ℓ is the cavity length, λ_0 is central wavelength between peaks, $\Delta\lambda$ is the distance between the peaks and n_g is group refractive index of PDMS. As a result, the cavity thickness was calculated to be about 10 μm.

Using the estimated cavity thickness, transmission response of the sandwich sample was simulated and compared with the measurement as shown in Fig. 1.3.

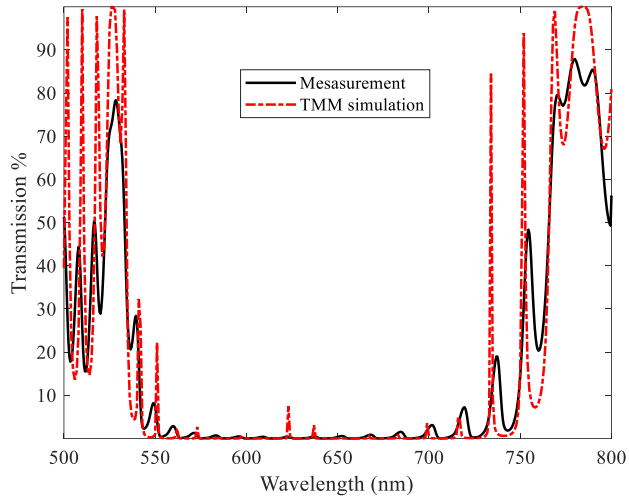

Figure 1.3 The transmission spectrum of the sandwich sample consisting of a 10 μm thick elastic microcavity layer placed in between two identical Bragg reflectors.

In order to observe the optical behaviours of the sandwich sample under compression, three different forces were applied, 20 N, 80 N and 100 N. A specially-designed compression setup consisting of four tunable springs and two parallel plates was used to measure the transmittance, using the Varian Cary mod.5000 apparatus, of the sandwich sample under loading without changing the orientation of the sample. The applied forces were tuned through four pre-calibrated springs by changing the length of springs with bolts. The illustration of the compression setup is given in Fig. 1.4. After the compression tests, the applied forces were removed to verify if the optical features returned to their initial position. Throughout the measurements, particular attention was paid to keeping the sample fixed on the apparatus without any movement that can deflect the light.

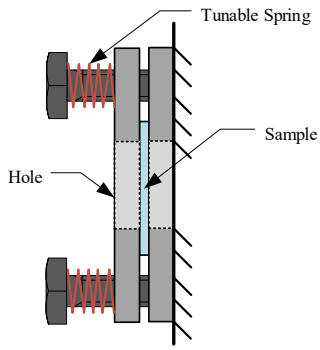

Figure 1.4 Illustration of the Compression System: Optical Characterization of the Sandwich sample under different forces was performed using a specially-designed apparatus. Two plates were located in parallel to each other, and a hole was placed at the centre of the plates to transmit light.

The transmittance measurement of the microcavity under different loadings is reported in Fig. 1.5.

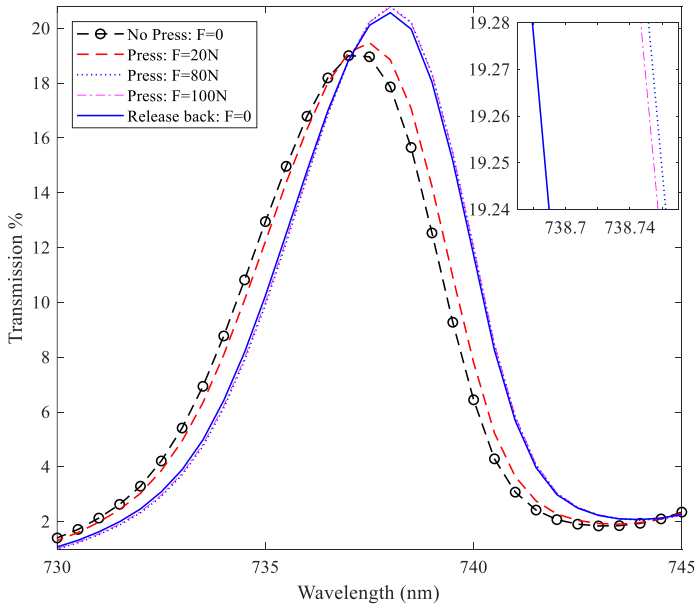

Figure 1.5 The spectral response of the sandwich sample under different compression forces.

Fig. 1.5 highlights that the cavity peak was shifted to higher wavelengths proportional to the magnitude of the applied forces. As expected, that the maximum displacement can be observed under has 100 N while the 20 N is the smallest. However, this shift does not seem to be linear with the applied force. The shift, in fact, in the optical spectra from 80 N to 100 N was not as significant as the shifts between 20 N to 80 N or 20 N to 100 N. The transmittance measurement was repeated after removing the last applied 100 N force. Despite the fact that, after all the forces were removed and the sample was expected to return back to its initial position, it settled in a position between plots of 20 N and 80 N. This is an indication that at these forces the viscoelastic features of PDMS layer become important.

The applied forces were caused mechanical deformations through the all layers, but in particular on the EMC layer because it has the lowest rigidity with respect to the other glass thin layers and substrates. The change in the thickness of the EMC due to the applied forces was simulated using the COMSOL Multiphysics software. The simulation results of the applied forces versus displacements on the EMC layer are shown in Fig. 1.6.

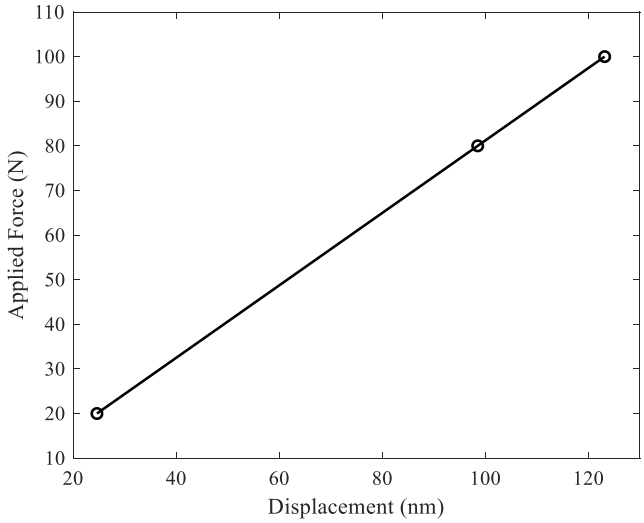

Figure 1.6 Simulation results of applied force versus displacement in the EMC layer considering only the thickness variation of the PDMS layer.

During the loading event, not only the mechanical deformations but also a change in the optical properties were observed. The loading triggered a change in the refractive index value and the absorption coefficient of the PDMS cavity layer [16] where this change can be explained by the Clausius-Mosotti equation [17].

In order to understand the optical response of the sandwich sample as a result of changes in the EMC thickness and the EMC refractive index, additional TMM simulations were employed.

On the one hand, a TMM simulation was performed considering the refractive index of the PDMS layer constant and the thickness of the EMC layer was decreased according to the Fig. 1.6. The peak behaviours were showed a trend to shift to the lower wavelengths.

On the other hand, another TMM simulation was performed. In this case, the thickness of the EMC layer was considered constant. Then the refractive index of the PDMS layer was increased according to the proportional increase in the stress [16]. The peak behaviours showed a trend to shift to the higher wavelengths.

So that, the additional TMM simulations showed that the shifting behaviour of the EMC was primarily influenced by the refractive index change due to the applied forces.

1.4 Conclusions

In this work, a mechanical sensor consisting of 1-D photonic crystals was designed and fabricated using radio frequency sputtering. In this respect, a wet fabrication protocol was developed and PDMS-based on an elastic microcavity layer was sandwiched between two equivalent Bragg reflectors. The Transfer Matrix Method simulations were performed for both the single Bragg and the sandwich sample by taking into account the wavelength-dependent refractive indices of the materials. The Transfer Matrix Method simulations and transmission measurements showed good agreement. In order to observe the system response under increasing loading, the sandwich sample was then subjected to forces with different magnitudes.

As a result, the optical response of the system was studied as a function of the applied forces. The transmittance response of the sandwich structure showed that cavity peaks shift to higher wavelengths and increase their intensity due to an increase of applied force. This effect took place due to both changes in elastic microcavity thickness and change of PDMS refractive index. Finally, the viscoelastic material properties of the PDMS influenced the system response due to loading removal.

References

[1] R. Datar, S. Kim, S. Jeon, P. Hesketh, S. Manalis, A. Boisen, T. Thundat, Cantilever sensors: Nanomechanical tools for diagnostics, MRS Bull. 34 (2009) 449–454. doi:10.1557/mrs2009.121.

[2] H.E. Joe, H. Yun, S.H. Jo, M.B.G. Jun, B.K. Min, A review on optical fiber sensors for environmental monitoring, Int. J. Precis. Eng. Manuf. - Green Technol. 5 (2018) 173–191. doi:10.1007/s40684-018-0017-6.

[3] M. Bellingeri, A. Chiasera, I. Kriegel, F. Scotognella, Optical properties of periodic , quasi-periodic , and disordered one- dimensional photonic structures, Opt. Mater. (Amst). 72 (2017) 403–421. doi:10.1016/j.optmat.2017.06.033.

[4] H. Rigneault, C. Amra, S. Robert, C. Begon, F. Lamarque, B. Jacquier, P. Moretti, A.M. Jurdyc, A. Belarouci, Spontaneous emission into planar multi-dielectric microcavities: theoretical and experimental analysis of rare earth ion radiations,, Opt. Mater. 11 (2-3) (1999) 167–180.

[5] Y. Li, L.M. Fortes, A. Chiappini, M. Ferrari, R.M. Almeida, High quality factor Er-doped Fabry–Perot microcavities by sol-gel processing, J. Phys. D Appl. Phys. 42 (20) (2009) 205104.

[6] G. Ma, J. Shen, Z. Zhang, Z. Hua, S.H. Tang, Ultrafast all-optical switching in one-dimensional photonic crystal with two defects,, Opt. Express 14 (2) (2006) 858–865.

[7] S. Valligatla, A. Chiasera, S. Varas, N. Bazzanella, D.N. Rao dielectric microcavity fabricated by RF-sputtering, Opt. Express 20 G.C. Righini, M. Ferrari, High quality factor 1-D Er3þ-activated (2012) 21214–21222.

[8] A. Chiasera, R. Belli, S.N.B. Bhaktha, A. Chiappini, M. Ferrari, Y. Jestin, E. Moser, G.C. Righini, C. Tosello, Appl. Phys. Lett. 89 (17) (2006) 171910–171913.

[9] A. Chiasera, J. Jasieniak, S. Normani, S. Valligatla, A. Lukowiak, S. Taccheo, D.N. Rao, G.C. Righini, M. Marciniak, A. Martucci, M. Ferrari, Hybrid 1-D dielectric microcavity: Fabrication and spectroscopic assessment of glass-based sub-wavelength structures, Ceram. Int. 41 (2015) 7429–7433. doi:10.1016/j.ceramint.2015.02.059.

[10] T.P. Burg, M. Godin, S.M. Knudsen, W. Shen, G. Carlson, J.S. Foster, K. Babcock, S.R. Manalis, Weighing of biomolecules, single cells and single nanoparticles in fluid, Nature. 446 (2007) 1066–1069. doi:10.1038/nature05741.

[11] R. Raiteri, H.J. Butt, Measuring electrochemically induced surface stress with an atomic force microscope, J. Phys. Chem. 99 (1995) 15728–15732. doi:10.1021/j100043a008.

[12] P.I. Oden, G.Y. Chen, R.A. Steele, R.J. Warmack, T. Thundat, Viscous drag measurements utilizing microfabricated cantilevers, Appl. Phys. Lett. 68 (1996) 3814–3816. doi:10.1063/1.116626.

[13] D.M. Topasna, G.A. Topasna, Numerical modeling of thin film optical filters, Educ. Train. Opt. Photonics. (2009) EP5. doi:10.1364/ETOP.2009.EP5.

[14] T. Siefke, S. Kroker, K. Pfeiffer, O. Puffky, K. Dietrich, D. Franta, I. Ohlídal, A. Szeghalmi, E.-B. Kley, A. Tünnermann. Materials pushing the application limits of wire grid polarizers further into the deep ultraviolet spectral range, Adv. Opt. Mater. 4, 1780–1786 (2016)

[15] I. H. Malitson. Interspecimen comparison of the refractive index of fused silica, J. Opt. Soc. Am. 55, 1205-1208 (1965)

[16] N. Tarjányi, I. Turek, I. Martinček, Effect of mechanical stress on optical properties of polydimethylsiloxane II - Birefringence, Opt. Mater. (Amst). 37 (2014) 798–803. doi:10.1016/j.optmat.2014.09.010.

[17]. R.P. Feynman, R.B. Leighton, M. Sands, PHYSICS, (n.d.).

Chapter 2

2 Design, Fabrication and Evaluation of an Optomechanical Sensor for Pressure and Vibration Detection using Flexible Multilayers

Abstract

We introduce an easily implementable optomechanical device for pressure and vibration sensing using a multilayer structure on a flexible substrate. We present the design, fabrication, and evaluation steps for a proof-of-concept sensor as well as optical glass components. The design steps include optical, mechanical, and optomechanical correlation simulations using the transfer matrix method, finite element analysis, geometric optics, and analytical calculations. The fabrication part focuses on the deposition of multilayers on polymeric flexible substrates using the radio frequency sputtering technique. To investigate the quality of the glass coatings on polymeric substrates, atomic force microscopy and optical microscopy are also performed. Optical measurements reveal that, even after bending, there are no differences between multilayer samples deposited on the polymeric and SiO_2 substrates. The performance assessment of the proof-of-concept device shows that the sensor resonance frequency is around 515 Hz and the sensor static response is capable of sensing from 50 Pa to 235 Pa.

2.1 Introduction

Optics driven sensing technologies bring several advantages over traditional pressure and vibration sensing approaches, which mostly rely on piezoelectricity, capacity and resistivity [1]. The nature of optical sensing systems offers some additional capabilities over current sensing technologies, such as immunity to electromagnetic interference, high signal-to-noise ratio per unit area and wide detection bandwidths [2,3]. For this reason, the development of optical sensing systems for pressure and vibration detection can extend the sensing limits in structural health monitoring, optoacoustic medical imaging and non-contact measurements [3]. Optical sensing modalities, using refraction, interference, and polarization can be employed for the determination of mechanical deformation in a medium. The refraction approach relies on the change in optical response due to change in local density of material while the interference approach relies on the change in spectral behavior of light due to optical interference [3]. In addition, both material property and spectral interference can also contribute to optical response [4]. The development of sensing systems based on the abovementioned sensing modalities shows some implementation challenges due to the material-nature of current optical components. More precisely, the fragility of glass-ceramic based optical components brings some difficulties for the implementation of optical components on thin and deformable structures such as membranes, beams, and cantilevers. Thus, the development of new fabrication protocols for optical materials, in particular flexible optical components, offers new device developments for mechanical sensing applications [5]. For instance: gratings, channel waveguides, also solar cells, and protective coatings can offer unique performance characteristics as compared to their rigid classical structures [6].

As a consequence of an increasing trend in flexible electronics, adding mechanical flexibility to the optical components became a popular subject in the field of optics and photonics. Moreover, integration of optical structures on deformable polymer substrates has given birth to flexible photonics, a field that has rapidly emerged in recent years to the forefront of photonics. Owing to the addition of mechanical flexibility to planar photonic structures, the wide range of application has acquired increasing popularity. To date, flexible planar photonic devices were almost exclusively fabricated using polymeric substrates, which do not offer high refractive indices that are necessary for strong optical confinement. It is also worthy to note that Corning [7] and Schott [8] have recently presented ultra-thin flexible glasses; therefore, there is a chance of a future development for an all-glass flexible photonics component that should operate in several stress conditions i.e. bending, folding, rolling, twisting, stretching and compression [9].

To date, there are several fabrication techniques that are used for fabrication of glass-based photonic devices such as ion implantation [10], sol-gel deposition [11,12], radio frequency (RF) sputtering [11] and electron-beam evaporation [13]. Among the numerous deposition techniques, the RF-magnetron sputtering technique is demonstrated to be a suitable method for glass deposition on a large area for optoelectronic devices [14,15] as well as on polymeric substrates [16,17].

Along this main vein, in this research work, we propose a force and vibration sensing approach based on tunable spectral filters based on flexible optical components. Both demonstration and characterization of a proof-of-concept optomechanical sensor (OMS) are presented. Thus, this paper is conceived with three main sections: i) modeling & design; ii) fabrication; iii) and results, respectively. In the first section, we present the working principle of a sensing system that uses flexible multilayer components in interaction with mechanical parts. Demonstration of the simulation methodologies for both optical and mechanical components using the transfer matrix method (TMM) and the finite element method (FEM) are shown. In addition, to estimate the interaction between optical and mechanical parts of the device, an optomechanical calculation scheme is proposed. In the following section, detailed information regarding the fabrication protocol SiO_2/TiO_2 multilayers on various flexible substrates is provided. Finally, in the third section, we present the characterization results of multilayer samples. Experimental and simulation work regarding the OMS is presented. More precisely, the transmittance and reflectance spectrum of the optical samples are shown. Quality of the flexible samples is examined using optical microscopy and atomic force microscopy (AFM). Finally, OMS is tested under static and dynamic loadings and its optomechanical behavior is estimated via an optomechanical simulation framework.

2.2 Modelling and Design

2.2.1 Working principle and design of a test device

The sensing methodology relies on the optical interaction between two multilayer components; where one of the components is called reflector, while the other one filter. The reflector is a flexible multilayer that is attached to a single-degree-of-freedom (SDoF) contact-layer for the purpose of one-directional reflection and mechanical tunability of the contact-layer without making a compromise on reflection spectrum. A full-spectral-width light source in the visible range illuminates the reflector. The reflected spectrum is, then, filtered by a filter and the final transmitted light is detected by a photodiode. In other words, the overlapping area of the reflectance and transmittance spectrum defines the area that will be detected by a photodiode. Working principle of the sensing system is illustrated in Fig. 2.1.

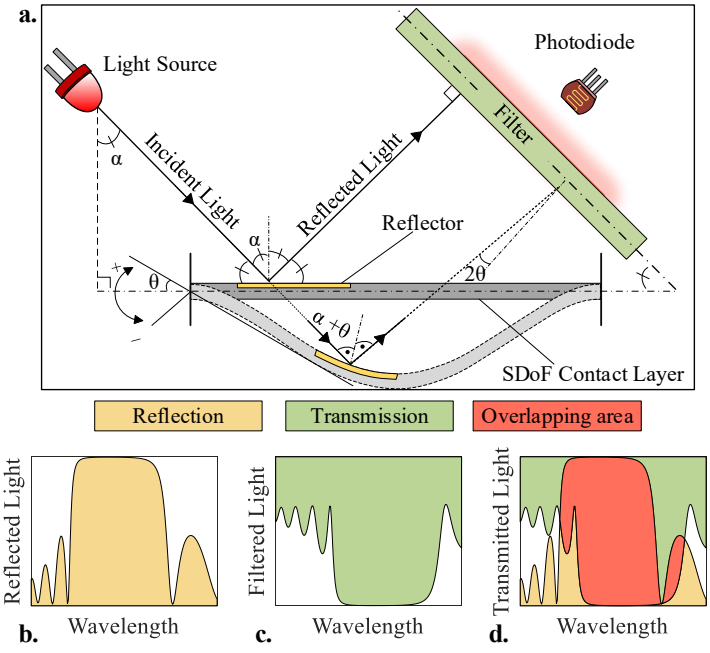

Figure 2.1 (a.) Illustration of the working principle of the sensing system. (b.) An example reflectance spectrum response of the reflector (c.) an example transmittance spectrum response of the filter. (d.) The overlapping area of two spectral features defines the spectrum of light that is finally detected by a photodiode.

Based on this idea, we have implemented a test device that is given in Fig. 2.2 more in detail. The test device is composed of a white LED light source, photodiode, reflector, a contact-layer, and housing components. The light source and the photodiode are both placed with the angle of α=45° to the reflector surface. Housing components were fabricated using 3D printing by ABS material. The bottom side of the housing is made of steel to provide better rigidity. A circular membrane was used as a contact layer made by an opaque-Mylar polyester film. The contact-layer is tightened through the housing components via four screws. A membrane sensing zone is drilled on the metal housing with a hole size of 20 mm in diameter. The reflector is attached on the half side of the membrane as 2 mm×10 mm a rectangular shape. Independent of the optical properties, the sensor response can be tuned easily by changing the membrane geometry and the material for future applications.

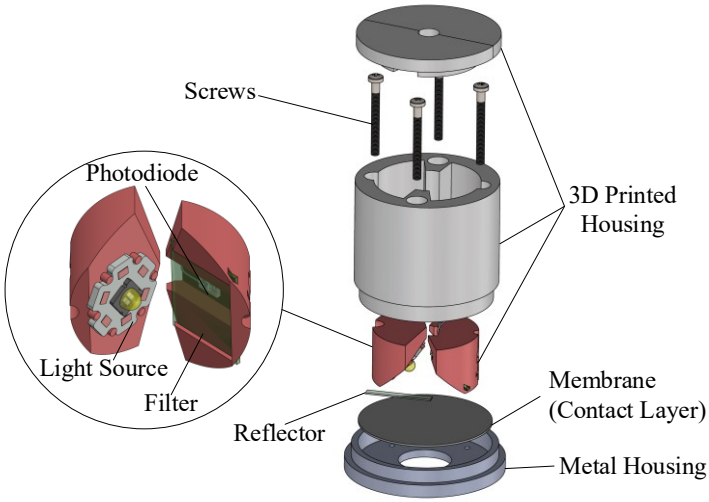

Figure 2.2 Schematic of the test device.

2.2.2 Optical modeling and multilayer design

In order to design the spectral behavior of multilayer components, we have performed a set of TMM [18,19] calculations. Taking into account the i subscript indicates the number of a layer in a multilayer structure, n refractive index, and α is the incident angle on the layer, then, the change in the incident angle for each layer change can be expressed using Snell's law given in (2.1).

$$n_{i-1} \sin \alpha_{i-1} = n_i \sin \alpha_i \tag{2.1}$$

Assuming that the reflector bending is similar to the rotation of a mirror, then, the effect of optical interactions, mainly the incident angle of each component, can be calculated using geometric optics (Fig. 2.1). Moreover, using this information, we can calculate the spectral response of an optical component through TMM.

In TMM calculations, each material segment of the multilayer can be expressed as one characteristics matrix by means of refractive index, thickness, and incident angle values. Characteristic matrix for a single layer can be formulated as in (2.2) where $\gamma_i = n_i \cos\theta_i \sqrt{\varepsilon_0 \mu}_0$, δ : phase difference and defined as in (2.3), t : layer thickness, λ : wavelength, $\varepsilon_0 = 8.85 \times 10^{-12}$: the permittivity of free space and $\mu_0 = 4\pi \times 10^{-12}$: the permeability of free space.

$$M^{(i)} = \begin{bmatrix} \cos\delta_i & \dfrac{j\sin\delta_i}{\gamma_i} \\ j\gamma_i \sin\delta_i & \cos\delta_i \end{bmatrix} \tag{2.2}$$

$$\delta_i(\lambda) = \frac{2\pi n_i t_i \cos\alpha_i}{\lambda} \tag{2.3}$$

Thus, for a multilayer with N total number of layers, the overall characteristic matrix, by representing all layers in one, can be written as in (2.4). Moreover, reflectance (R) and transmittance (T) for reflector and filter can be calculated as in (2.5) and (2.6), respectively.

$$\mathrm{M} = \prod_{i=1}^{N} \mathrm{M}^{(i)} \tag{2.4}$$

$$T(\lambda) = 100\left(\left| \frac{2 \cdot \gamma_1}{\gamma_1 \cdot (\mathrm{M})_{1,1} + \gamma_1 \cdot \gamma_N \cdot (\mathrm{M})_{1,2} + (\mathrm{M})_{2,1} + \gamma_N \cdot (\mathrm{M})_{2,2}} \right| \right)^2 \tag{2.5}$$

$$R(\lambda) = 100\left(\left| \frac{\gamma_1 \cdot (\mathrm{M})_{1,1} + \gamma_1 \cdot \gamma_N \cdot (\mathrm{M})_{1,2} - (\mathrm{M})_{2,1} - \gamma_N \cdot (\mathrm{M})_{2,2}}{\gamma_1 \cdot (\mathrm{M})_{1,1} + \gamma_1 \cdot \gamma_N \cdot (\mathrm{M})_{1,2} + (\mathrm{M})_{2,1} + \gamma_N \cdot (\mathrm{M})_{2,2}} \right| \right)^2 \tag{2.6}$$

In the current design configuration, considering the θ is the bending of the membrane, thus, the reflection angle of the reflector will be $(\alpha + \theta)$ and similarly, the incident angle of the filter will be 2θ. In other words, a bending of the reflector does

not only change the reflection angle of the reflector but also changes the incident angle on the filter. Regarding this information, spectral interaction between the reflector and filter can be estimated via TMM which will be further discussed in the optomechanical calculation section.

Multilayer structures are designed using SiO_2 and TiO_2 alternating material layers deposited on a silica substrate. Design spectrum is considered in the visible range where wavelengths vary from 400 nm to 800 nm. In total, 7 couples of SiO_2 and TiO_2 layers were chosen. Each SiO_2 and TiO_2 layer thickness is about 105 nm and 65 nm, respectively. Throughout the calculations, we have used the wavelength-dependent refractive index values from [20,21]. The multilayer design is shown in Fig. 2.3.

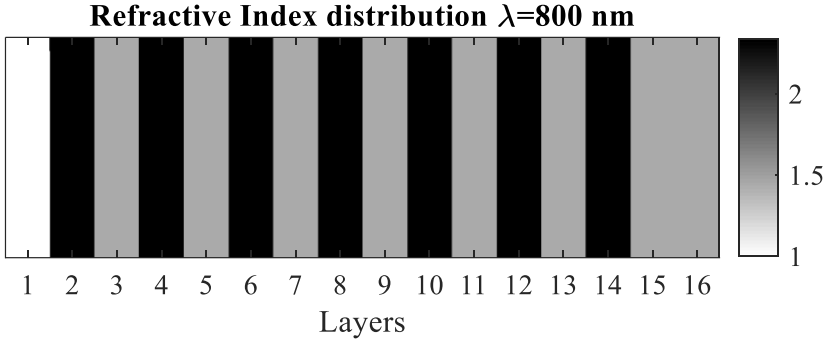

Figure 2.3 Refractive index distribution of the multilayer design at 800 nm. Here the 1st and 16th layers correspond to air and substrate, respectively. Black layers correspond to TiO_2 while gray layers show SiO_2 layers.

2.2.3 Membrane deflection and bending angle

The contact-layer is a key component that defines the mechanical detection capabilities of the sensor. Deflection of the contact-layer defines detection sensitivity of the sensor for static loading as well as dynamic response of the sensor for vibration detection. In this study, we have considered a circular contact layer in particular it is called a membrane. The deflection of a fixed-end circular membrane is illustrated in Fig. 2.4.

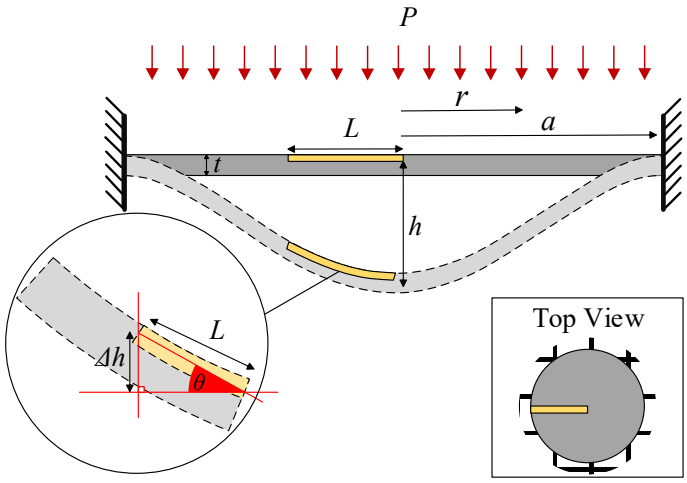

Figure 2.4 OMS membrane deflection. The reflector (shown in yellow) is attached to half part of the circular membrane.

Membrane deflection can be calculated using the analytical formula given in (2.7)

$$h(r) = \frac{Pa^2}{4T_0}\left(1 - \frac{r^2}{a^2}\right) \tag{2.7}$$

where P : uniform pressure acting on the membrane, a is membrane radius, r is radial position through the radius, and T_0 is pretension force acting on membrane. Thus, considering a rectangular reflector that is attached to the membrane with the length of L, then bending angle θ can be derived as in (2.8).

$$\theta = \tan^{-1}\left(\frac{\Delta h}{\sqrt{L^2 - \Delta h^2}}\right) \tag{2.8}$$

where the Δh corresponds to the change in the deflection that is obtained from (2.7).

It is worthy to note that, depending on flexural rigidity and pretension of structures, concerning: thickness, radius, and elastic modulus, different boundary conditions apply. Therefore, a structure can be modelled either by a plate or by a membrane (also called the diaphragm). More details can be found in [22,23].

Moreover, the frequency response is also important to define the membrane response under dynamic loadings. Thus, the natural frequency (f_N) of a circular membrane can be analytically calculated [42] as given in (2.9)

$$f_N = \frac{k_N}{2\pi a}\sqrt{\frac{T_0}{t\rho}} \tag{2.9}$$

where ρ is the density of the membrane and k_N is the mode factor which comes from the roots of the Bessel functions, thus, for the first mode of the membrane (also known as 1,0 mode), the mode factor is 2.4048.

In this work, we have used Mylar polyester film with material properties given in Table 2.1.

Table 2.1 Material Properties for Mylar polyester film

Material Property	**Value**
Thickness	0.07 mm
Young's Modulus	98 MPa
Poisson's Ratio	0.38
Density	1390 kg/m^3

In addition to the analytical calculations, we have computed FEM simulations using COMSOL Multiphysics. More in detail, a modal analysis (also known as eigenfrequency analysis in COMSOL Multiphysics) is performed for both membrane and OMS housing to determine the resonance frequency of the structures. The membrane deflection under different static loadings is calculated.

1.4 Optomechanical simulation framework

In order to calculate the change in the optical response due to the mechanical deflections, we developed an optomechanical calculation scheme. Thus, in this calculation scheme, firstly the deflection and the bending angle of the membrane are calculated. Then, this mechanical information is inserted into the TMM computations to calculate the wavelength shifts in the optical spectrum for both the filter and the reflector. Then, the transmittance and the reflectance measurements were shifted in lower and higher wavelengths respectively, by taking into account the wavelength shift values that are obtained through the calculations. Finally, the overlapping area of two spectrums is calculated using the Trapezoidal numerical integration that is expected to define the overall sensor response as intensity change on the photodiode. The optomechanical calculation scheme is summarized in Fig. 2.5.

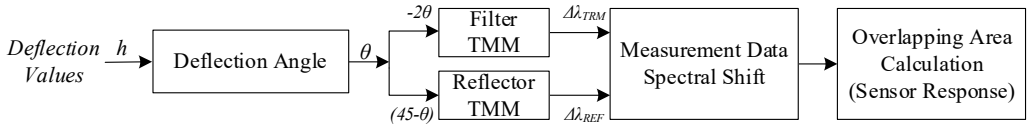

Figure 2.5 Summary of the optomechanical calculation framework.

2.3 Fabrication of optical components

The multilayer structures were fabricated using an RF-sputtering deposition system. In total, 7 couples (14 single layers) of SiO_2 and TiO_2 films were deposited on polyester (3M PP2500), poly-methyl methacrylate (PMMA), and conventional silicon (Si) and silica (SiO_2) substrates. No difference is evidenced in the optical properties of the films deposited on the different substrates [25]. For deposition, alternatively changing a 15×5 cm^2 titania and a 15×5 cm^2 silica targets were used. The residual pressure before the deposition was 4.5×10^{-7} mbar. During the deposition procedure, the substrates were not heated and the temperature of the sample holder during the deposition was kept at 30 °C. More in detail, the conventional cleaning protocols for the SiO_2 and Si substrates require a thermal cleaning procedure before the deposition, that is involving heating of the substrates up to 120 °C for 10 minutes under vacuum at 10^{-6} mbar. However, the polymeric substrates cannot bear the high temperatures. For this reason, thermal cleaning was not performed. The cleaning process was performed using ethanol and distilled water only. The chamber environment was Ar gas with a pressure of 5.4×10^{-3} mbar, and an RF power of 110 W was applied for both silica and titania targets. In order to monitor the thickness of the layers during the deposition, two quartz microbalances from Inficon instruments (model number: SQM-160) were placed for each sample separately. The thickness monitoring system was calibrated beforehand, for both targets with a long deposition process (24 hrs. of deposition) and thicknesses were measured independently through an m-line apparatus [15,26]. The final resolution of the effective thickness for this quartz microbalance is about 1 Å. More details are available in reference [27].

In addition, various characterization techniques were performed to investigate the multilayer properties. The absorption spectrum of the samples in the VIS-NIR region was obtained by using a double beam Varian-Cary spectrophotometer with a resolution of 2 nm [27].

Atomic force microscopy (AFM) was performed with a Solver Px Scanning Probe Microscope from NT-MDT. AFM topographies were acquired in semi-contact mode with a silicon tip ~219.8 kHz, Q338 with a nominal radius of less than 10 nm. AFM analyses were performed starting from the center of each sample. Wide areas, 20×20 μm^2, were also scanned with lower resolution (256×256 pixels) to avoid particles and

determine the best area to characterize. Analyses were repeated on different scanning areas, 10×10 μm^2, 5×5 μm^2, and 2×2 μm^2 with a resolution of 512×512 pixels. An additional area, 100×100 μm^2, was also scanned for further investigation if any scratch or creep occurring on the surface layer due to the bending of the substrates. There was no significant surface defect observed.

2.3.1 Experiment setup for sensor testing

A custom-made controller was developed and connected to OMS. The light source brightness is tuned using a variable resistor through the controller. In order to reduce ambient noise, light source and photodiode signal were modulated through a chopper and a lock-in amplifier. Finally, the OMS signal was monitored using an oscilloscope. The experiment setup and detailed illustration of the instrumentation are shown in Fig. 2.6.

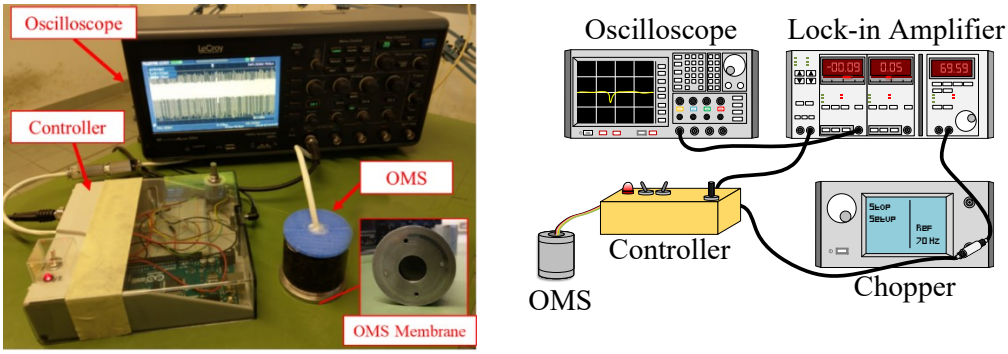

Figure 2.6. OMS Experiment setup (left). Detailed instrument setup (right).

2.4 Results

2.4.1 Optical components

Transmittance and reflectance measurements were performed for the samples. Figure 2.7 shows the transmittance spectra of the multilayer structure deposited on a silica substrate and its comparison to the TMM calculation Moreover, the reflectance spectra of the multilayer structure deposited on silica and the flexible substrates are shown in Fig. 2.8. Fabricated samples are also shown in Fig 2.9.

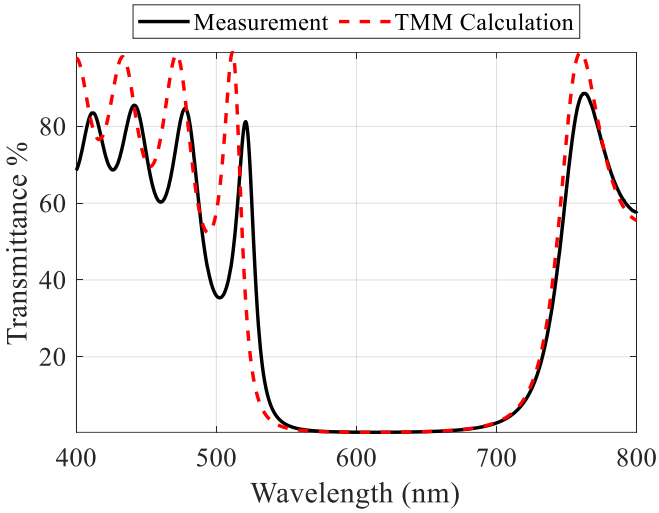

Figure 2.7. Transmittance measurement of the multilayer structure deposited on a silica substrate and its comparison to the TMM calculation.

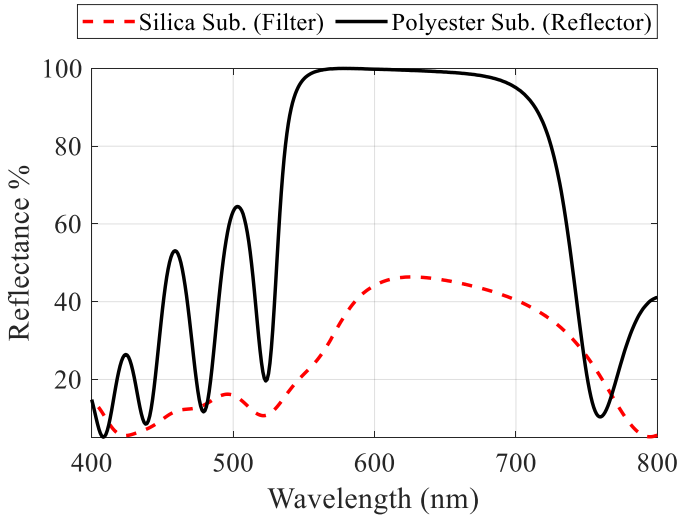

Figure 2.8. Reflectance measurement of the multilayer structure deposited on silica and flexible substrate.

Figure 2.9. Fabricated samples. The multilayer films sdeposited on a silica substrate (left); the multilayer films deposited on a flexible polyester substrate under bending (right).

In order to investigate the coating quality of the flexible samples, before and after the bending conditions, optical microscopy and AFM were used. The optical microscope images of the multilayer structure deposited on a PMMA substrate are shown in Fig. 2.10.

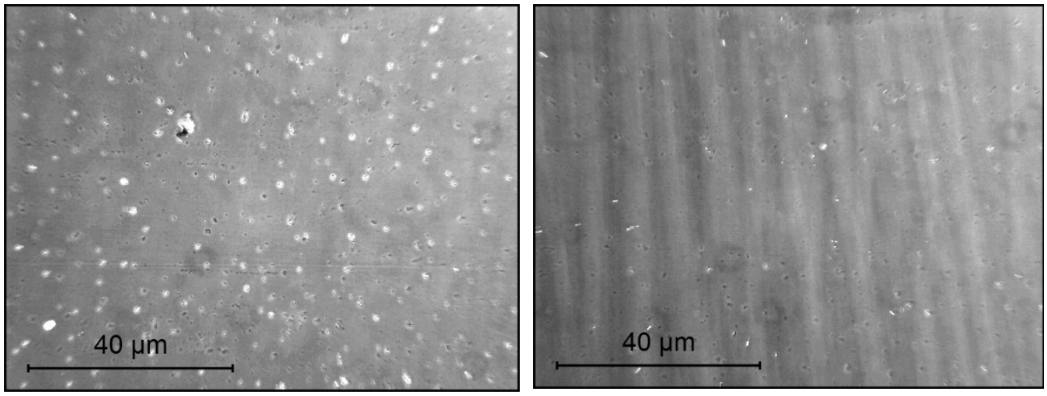

Figure 2.10. Optical microscope image of the multilayer structure on a PMMA before and after bending (left and right respectively.)

There were some local defects observed due to the lack of a significant cleaning process before the deposition. It is also expected that the contamination on the substrate surface can cause that kind of imperfections. Optical microscopy images do not show any significant damage to the coatings after bending. Moreover, the films did not show any delamination neither cracks. However, some ripple-like patterns are observed, probably due to the surface stress of the PMMA substrate under mechanical deformation.

Three uncoated substrates and three multilayer-coated substrates of silica, silicon, and PMMA were investigated by AFM. The average roughness (R_a) and root mean square roughness (R_q) values on different scanning area for the three substrates and coatings were calculated (Fig. 2.11).

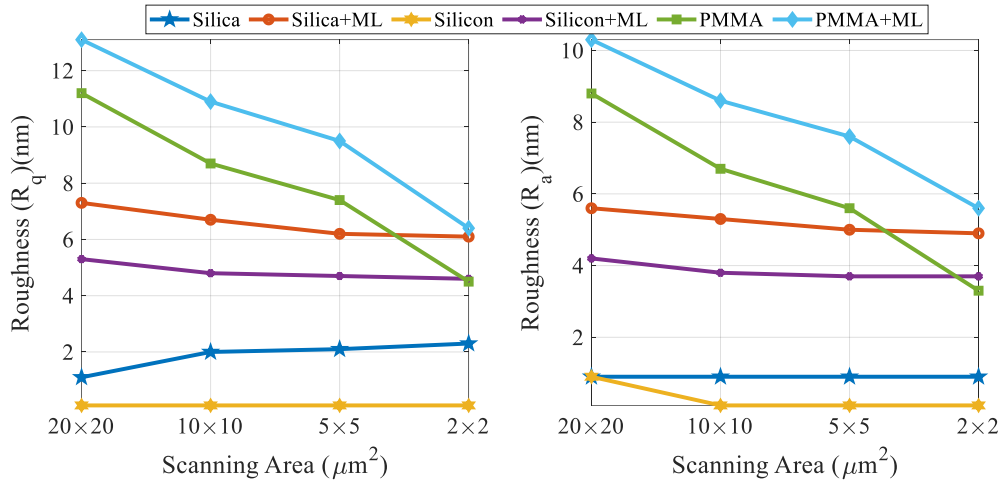

Figure 2.11. Root mean square roughness (R_q) (left) and average roughness (R_a) (right) on different scan areas for the three substrates silica, silicon, and PMMA and relative multilayer (ML) deposited system.

Figure 2.11 shows that the multilayer coatings exhibit higher surface roughness with respect to the substrates. The roughness rises from about 4 to 5 nm for silicon and silica and 2 nm for PMMA. Moreover, it is not reported here, but a further inspection on a wider area (100x100 μm^2) of a multilayer sample was also performed, and still, no significant defects were observed.

2.4.2 Modal analysis

In order to understand the modal response of the OMS device, an impact test analysis was performed [43]. Therefore, the OMS is fixed into an optical table with an apparatus which is a plate with a hole that enables it to interact with the membrane. After that, the membrane is excited by a 3 hex size key like mimicking a hummer impact. Three different impact tests were carried out. OMS response under different impacts and their comparison to three ambient noise measurements is shown in Fig. 2.12.

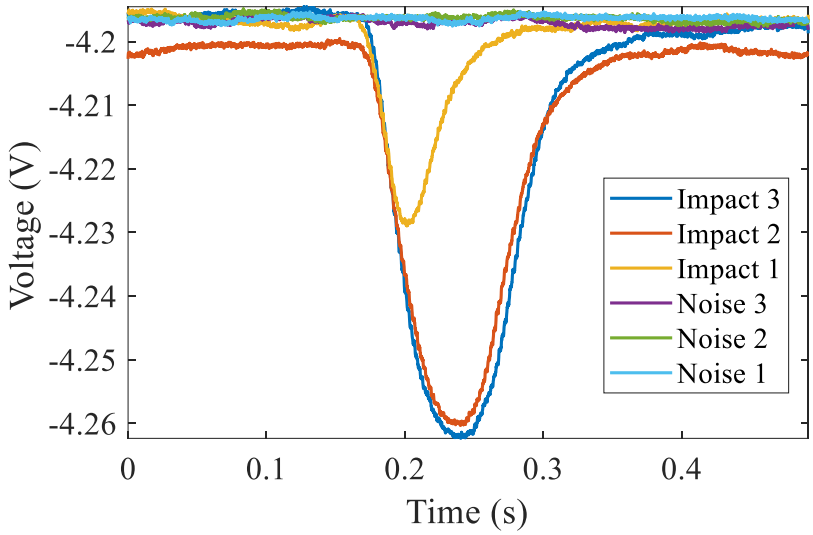

Figure 2.12. The OMS response under impacts. The signals that are labeled as Noise 1,2, and 3 are measured without any excitation on the membrane, while impact 1,2, and 3 corresponds to excitations with varying amplitudes.

Impact signals are converted into the frequency domain by using the Fourier Transform (FFT). We have observed a resonance peak of about 515 Hz. However, there is also another resonance at 1 kHz due to the ambient noise. The frequency-domain response of the OMS is given in Fig. 2.13. According to equation (2.9), the resonance frequency is calculated considering 250 kPa membrane pretension. Moreover, FEM modal analysis was performed for both membrane and the housing. In Figs. 2.14 (a) and (b) membrane first mode shape at 515 Hz, and the model response of the housing are presented, respectively.

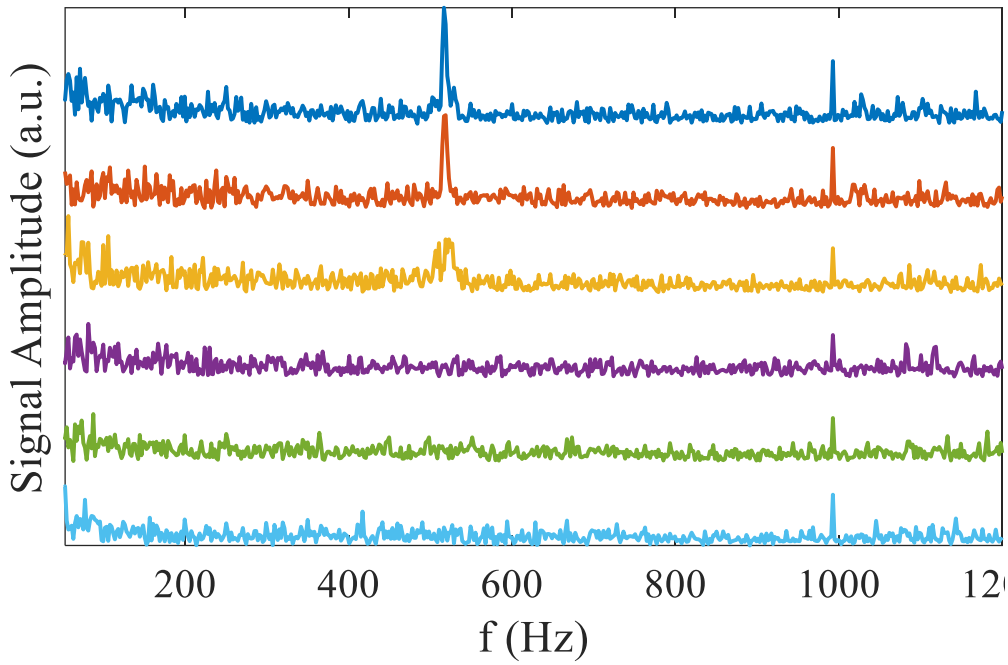

Figure 2.13. FFT analysis of the impact test signals. The first three signals from bottom to top are showing background noise (Noise 1, 2, and 3 respectively). The first three signals from top to bottom are showing signals result from different impact forces (Impact 3,2 and 1 respectively).

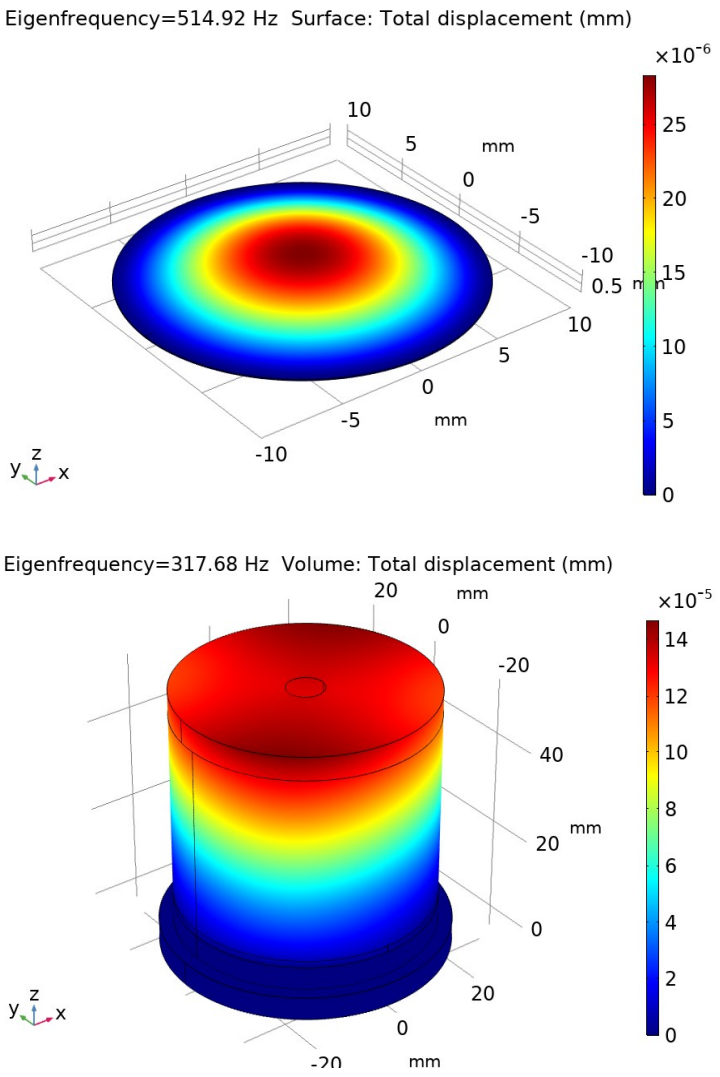

Figure 2.14. First mode shape of the OMS about 515 Hz (top). The first mode shape of the Housing and resonance frequency is about 317 Hz (bottom). (Numbers and colors represent the level of the displacement. Do not reflect real displacement values.)

2.4.3 Static response analysis

OMS response is investigated under static loading conditions. Thus, varying weight forces corresponding from 50 Pa to 235 P were placed on the membrane, and the OMS response was recorded. The voltage change in the OMS response loading is given in Fig 2.15. Moreover, the membrane deflection is simulated via both FEM and analytically. The membrane deflection under 200 Pa loading is shown in Fig. 2.16.

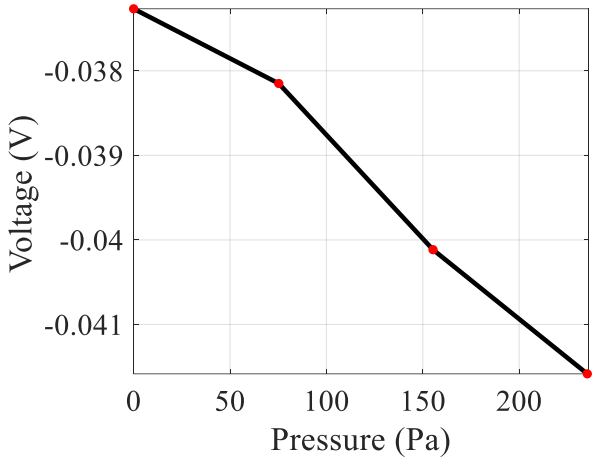

Figure 2.15. OMS response under loading.

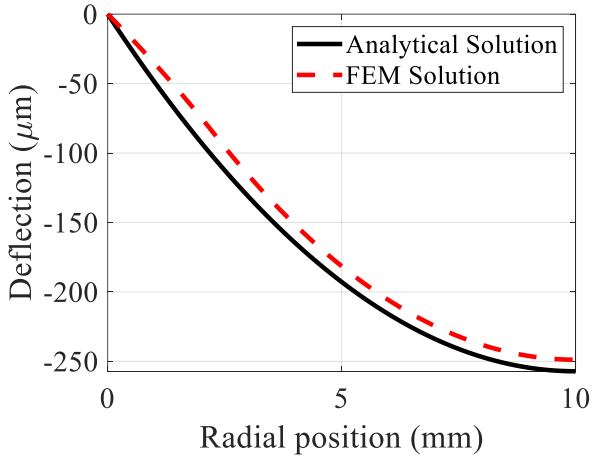

Figure 2.16. Membrane Deflection under 200 Pa loading. The simulated curve is also shown (dashed-red).

2.4.4 Optomechanical simulations

The static response of the OMS is calculated via the optomechanical analysis. In this context, the membrane deflection values are calculated under varying loadings up to 235 Pa and bending angles were derived. By using these bending angle values, spectral changes are calculated through several TMM calculations. The change in the wavelength of the reflector and the filter is shown in Fig. 2.17.

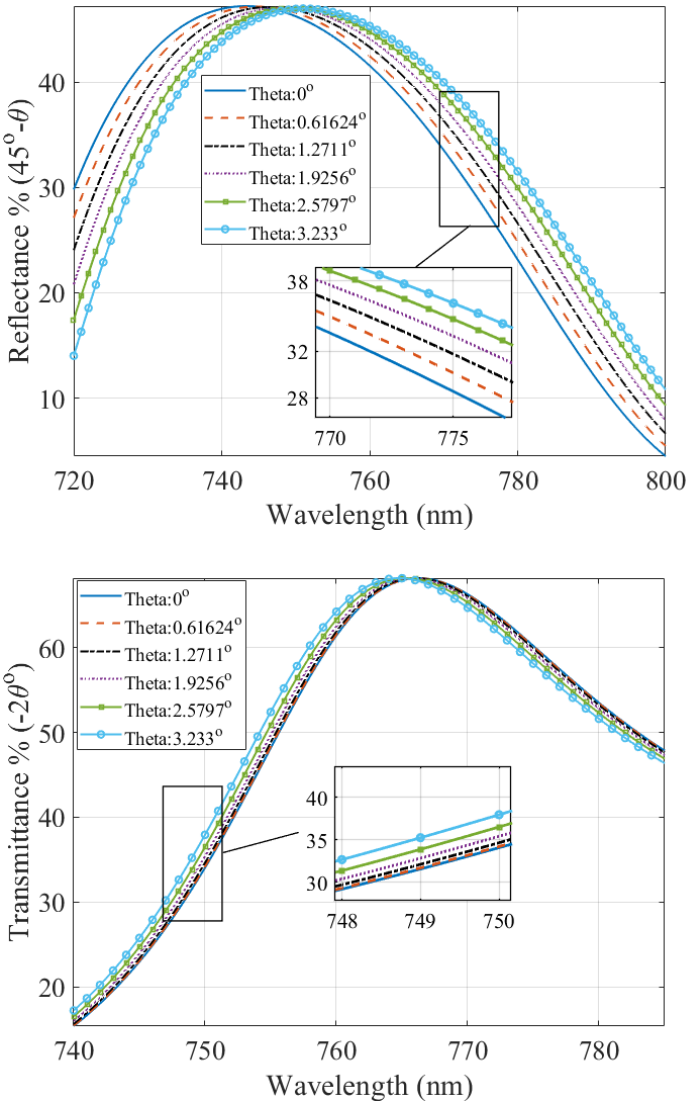

Figure 2.17. Simulated spectral shift at the stopband of the reflector (top) and the filter (bottom).

TMM results show that the reflectance spectrum shifts to higher wavelengths while the transmittance spectrum shifts to the lower wavelengths. The dynamic range of the wavelength changes is shown in Fig. 2.18.

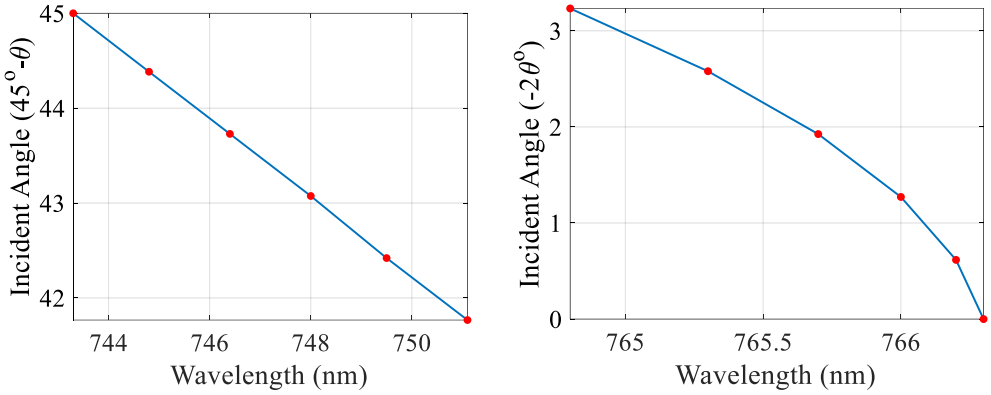

Figure 2.18. Simulated change in the wavelength values for the reflector (left) and the filter (right).

Finally, the static response of the OMS is calculated as shown in Fig. 2.19. Moreover, the spectral configuration of the reflector and the filter at $\theta = 3.233°$ is given in Fig 2.20.

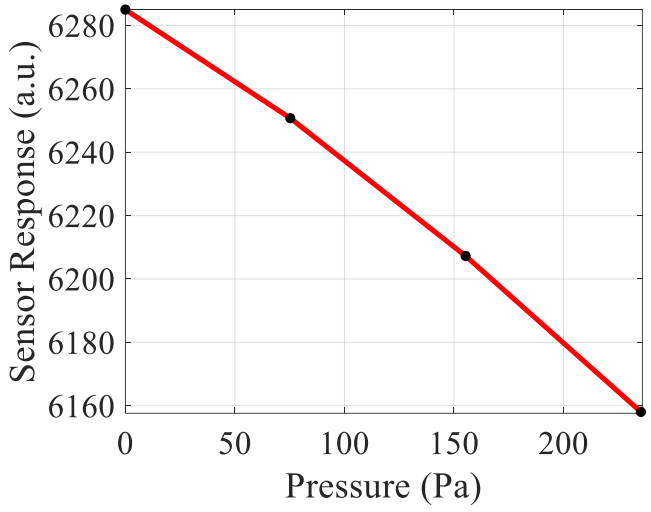

Figure 2.19. Simulated sensor response under loading.

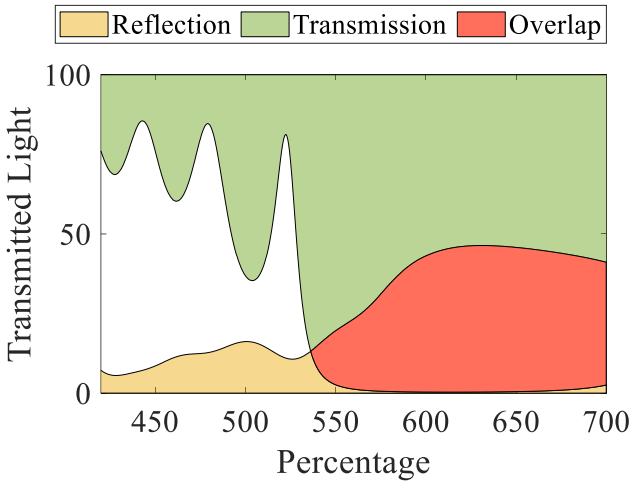

Figure 2.20. The spectral configuration of the OMS at $\theta = 3.233°$

Similarly, we have also simulated the dynamic response of the OMS through optomechanical calculations. In order to define the deflection values, we have performed frequency domain analysis for the OMS. More in detail, the OMS membrane is excited with a 100 Pa periodic input force using COMSOL Multiphysics and its response through the spectrum is calculated. The membrane deflection values at each frequency value are extracted and then plugged into the optomechanical; calculations. Therefore, the spectral change of the deflection angle, as well as the sensor response, are calculated. The calculation results are given in Fig. 2.21.

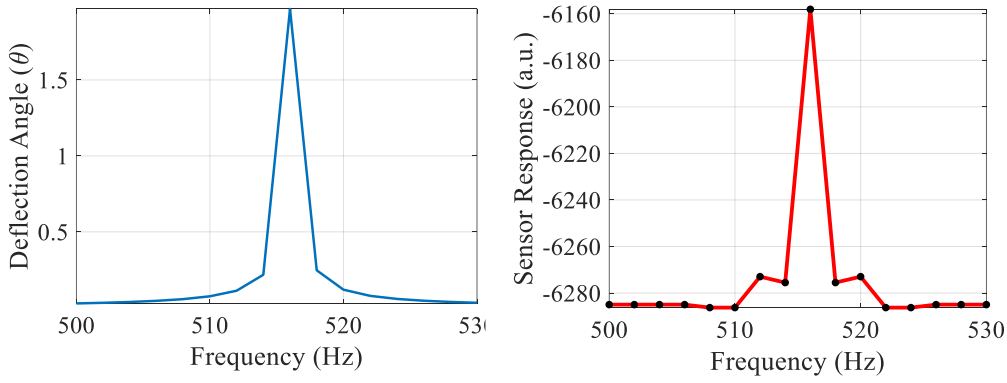

Figure 2.21. The deflection angle change under dynamic loading (left). The frequency response of the OMS is calculated through the optomechanical simulation framework (right).

2.5 Conclusions

In this paper, an innovative sensing approach has been introduced for force and vibration detection based on flexible photonic components. In order to fabricate the optical components, a protocol has been developed through SiO_2/TiO_2 multilayers on a rigid, as well as a flexible substrate, using the RF-sputtering technique. The optical response of multilayers was evaluated using both the transfer matrix method simulations and spectrophotometer measurements. Optical microscopy and AFM measurements confirmed the good quality of the glass on the flexible substrates. No cracks were observed on the multilayer structure. A proof-of-concept optomechanical sensor has been demonstrated using a flexible multilayer. A thin mechanical contact layer was attached to the flexible reflector and mechanical deformations were measured. The sensor performance was characterized by both static and dynamic conditions. It was found that the device is capable of detecting static loadings from 50 Pa to 235 Pa values. Moreover, the dynamic response of the sensor was detected at about 515 Hz by means of an impact test. Additional analysis regarding the dynamic response of the sensor was also carried out through both analytical and finite element calculations. In order to couple mechanical deformations through the optical response, an optomechanical simulation framework has been developed. The interaction between the optical and the mechanical components was correlated by means of measurement data, geometric optics, transfer matrix simulations, and finite element analysis. Thus, the framework showed that the optomechanical response of the sensor device can be estimated through reliable simulations.

Acknowledgements

This research is performed in the framework of the projects CNR-PAS “Flexible Photonics” (2020-2021); the Polish National Agency for Academic Exchange (NAWA) grant no. PPN/IWA/2018/1/00104 and Italian Ministry of Education, University and Research (MIUR) in the frame of the ‘Departments of Excellence’ (grant L 232/2016).

References

[1] C. U. Grosse and M. Ohtsu, *Acoustic emission testing*. Springer Science \& Business Media, 2008.

[2] A. Nair and C. S. Cai, “Acoustic emission monitoring of bridges: Review and case studies,” *Eng. Struct.*, vol. 32, no. 6, pp. 1704–1714, 2010.

[3] K. Ohno and M. Ohtsu, “Crack classification in concrete based on acoustic emission,” *Constr. Build. Mater.*, vol. 24, no. 12, pp. 2339–2346, 2010.

[4] R. Di Filippo, G. Abbiati, O. Sayginer, P. Covi, O. S. Bursi, and F. Paolacci, “Numerical surrogate model of a coupled tank-piping system for seismic fragility analysis with synthetic ground motions,” in *American Society of Mechanical Engineers, Pressure Vessels and Piping Division (Publication) PVP*, 2019, vol. 8.

[5] O. Sayginer, R. di Filippo, A. Lecoq, A. Marino, and O. S. Bursi, “Seismic Vulnerability Analysis of a Coupled Tank-Piping System by Means of Hybrid Simulation and Acoustic Emission,” *Exp. Tech.*, 2020.

[6] G. Manthei and K. Plenkers, “Review on in situ acoustic emission monitoring in the context of structural health monitoring in mines,” *Appl. Sci.*, vol. 8, no. 9, 2018.

[7] C. Barile, C. Casavola, G. Pappalettera, and V. P. Kannan, “Application of different acoustic emission descriptors in damage assessment of fiber reinforced plastics: A comprehensive review,” *Eng. Fract. Mech.*, p. 107083, 2020.

[8] L. Zhang, H. Yalcinkaya, and D. Ozevin, “Sensors and Actuators A : Physical Numerical approach to absolute calibration of piezoelectric acoustic emission sensors using multiphysics simulations,” vol. 256, pp. 12–23, 2017.

[9] K. Marschall, “Processing Technology In-Process Monitoring with Piezoelectric Sensors,” vol. 44, pp. 345–352, 1994.

[10] W. P. Mason, H. J. Mcskimin, and W. Shockley, “Ultrasonic Observation of Twinning in Tin,” *Phys. Rev.*, vol. 73, no. 10, pp. 1213–1214, May 1948.

[11] N. Thompson and D. J. Millard, “XXXVIII. Twin formation, in cadmium,” *London, Edinburgh, Dublin Philos. Mag. J. Sci.*, vol. 43, no. 339, pp. 422–440, 1952.

[12] N. Sabri, S. A. Aljunid, M. S. Salim, R. B. Ahmad, and R. Kamaruddin, “Toward Optical Sensors: Review and Applications,” *J. Phys. Conf. Ser.*, vol. 423, p. 12064, Apr. 2013.

[13] A. Theodosiou and K. Kalli, “Recent trends and advances of fibre Bragg grating sensors in CYTOP polymer optical fibres,” *Opt. Fiber Technol.*, vol. 54, p. 102079, 2020.

[14] G. Wissmeyer, M. A. Pleitez, A. Rosenthal, and V. Ntziachristos, “Looking at sound: optoacoustics with all-optical ultrasound detection,” *Light Sci. Appl.*, vol. 7, no. 1, p. 53, 2018.

[15] A. Macleod, *Thin-Film Optical Filters*, vol. 53, no. 4. 2012.

[16] J. H. Z. Christi K. Madsen, *Optical Filter Design and Analysis*. .

[17] J. K. Thomson, H. K. Wickramasinghe, and E. A. Ash, “A Fabry-Perot acoustic surface vibration detector - Application to acoustic holography,” *J. Phys. D. Appl. Phys.*, vol. 6, no. 6, pp. 677–687, 1973.

[18] P. C. Beard, “Transduction mechanisms of the Fabry-Perot polymer film sensing concept for wideband ultrasound detection,” *IEEE Trans. Ultrason. Ferroelectr. Freq. Control*, vol. 46, no. 6, pp. 1575–1582, 1999.

[19] E. Zhang, J. Laufer, and P. Beard, “Backward-mode multiwavelength photoacoustic scanner using a planar Fabry-Perot polymer film ultrasound sensor,” *Appl. Opt.*, vol. 47, no. 4, pp. 561–577, 2008.

[20] P. Morris, A. Hurrell, A. Shaw, E. Zhang, and P. Beard, “A Fabry–Pérot fiber-optic ultrasonic hydrophone for the simultaneous measurement of temperature and acoustic pressure,” *J. Acoust. Soc. Am.*, vol. 125, no. 6, pp. 3611–3622, 2009.

[21] M. Bellingeri, A. Chiasera, I. Kriegel, and F. Scotognella, “Optical properties of periodic, quasi-periodic, and disordered one-dimensional photonic structures,” *Opt. Mater. (Amst).*, vol. 72, pp. 403–421, 2017.

[22] K. O. Hill and G. Meltz, “Fiber Bragg grating technology fundamentals and overview,” *J. Light. Technol.*, vol. 15, no. 8, pp. 1263–1276, Aug. 1997.

[23] S. Larouche and L. Martinu, “OpenFilters: open-source software for the design, optimization, and synthesis of optical filters,” *Appl. Opt.*, vol. 47, no. 13, p. C219, 2008.

[24] D. M. Topasna and G. A. Topasna, “Numerical modeling of thin film optical filters,” *Educ. Train. Opt. Photonics*, no. October, p. EP5, 2009.

[25] G. F. Burkhard, E. T. Hoke, and M. D. McGehee, “Accounting for Interference, Scattering, and Electrode Absorption to Make Accurate Internal Quantum Efficiency Measurements in Organic and Other Thin Solar Cells,” *Adv. Mater.*, vol. 22, no. 30, pp. 3293–3297, Aug. 2010.

[26] Y. G. Boucher, J. Le Rouzo, I. Ribet-Mohamed, and R. Haïdar, “Modified form birefringence in periodic multilayer structures including uniaxial anisotropic materials,” *J. Opt. Soc. Am. B*, vol. 25, no. 5, pp. 777–784, May 2008.

[27] Y. Li, L. M. Fortes, A. Chiappini, M. Ferrari, and R. M. Almeida, “High quality factor Er-doped Fabry-perot microcavities by sol-gel processing,” *J. Phys. D. Appl. Phys.*, vol. 42, no. 20, 2009.

[28] G. Ma, J. Shen, Z. Zhang, Z. Hua, and S. H. Tang, “Ultrafast all-optical switching in one-dimensional photonic crystal with two defects,” *Opt. Express*, vol. 14, no. 2, pp. 858–865, Jan. 2006.

[29] H. Rigneault *et al.*, “Spontaneous emission into planar multi-dielectric microcavities: Theoretical and experimental analysis of rare earth ion radiations,” *Opt. Mater. (Amst).*, vol. 11, no. 2–3, pp. 167–180, Jan. 1999.

[30] S. Valligatla *et al.*, “High quality factor 1-D Er^3+-activated dielectric microcavity fabricated by RF-sputtering,” *Opt. Express*, vol. 20, no. 19, p. 21214, Sep. 2012.

[31] A. Chiasera *et al.*, “Hybrid 1-D dielectric microcavity: Fabrication and spectroscopic assessment of glass-based sub-wavelength structures,” *Ceram. Int.*, vol. 41, no. 6, pp. 7429–7433, 2015.

[32] T. P. Burg *et al.*, “Weighing of biomolecules, single cells and single nanoparticles in fluid,” *Nature*, vol. 446, no. 7139, pp. 1066–1069, 2007.

[33] R. Raiteri and H. J. Butt, “Measuring electrochemically induced surface stress with an atomic force microscope,” *J. Phys. Chem.*, vol. 99, no. 43, pp. 15728–15732, 1995.

[34] “COMSOL Multiphysics® v. 5.4. www.comsol.com. COMSOL AB, Stockholm, Sweden.” Stockholm, Sweden.

[35] O. Sayginer, A. Chiasera, S. Varas, A. Lukowiak, M. Ferrari, and O. S. Bursi, “Design and fabrication of multilayer-driven optomechanical device for force and vibration sensing,” in *Fiber Lasers and Glass Photonics: Materials through Applications II*, 2020, vol. 11357, pp. 328–337.

[36] H. Sun and X. Li, “Recent Advances on III-Nitride Nanowire Light Emitters on Foreign Substrates – Toward Flexible Photonics,” *Phys. status solidi*, vol. 216, no. 2, p. 1800420, Oct. 2018.

[37] “Corning Willow Glass Laminates | Ultra-thin, Bendable, Flexible Glass |

Corning." [Online]. Available: https://www.corning.com/worldwide/en/innovation/corning-emerging-innovations/corning-willow-glass.html. [Accessed: 09-Jan-2021].

[38] "Let the future evolve in your hands - Schott Innovation." [Online]. Available: https://www.us.schott.com/innovation/ultrathinglass/. [Accessed: 09-Jan-2021].

[39] D. W. Mohammed, R. Waddingham, A. J. Flewitt, K. A. Sierros, J. Bowen, and S. N. Kukureka, "Mechanical properties of amorphous indium--gallium--zinc oxide thin films on compliant substrates for flexible optoelectronic devices," *Thin Solid Films*, vol. 594, pp. 197–204, 2015.

[40] M. Kadic, G. W. Milton, M. van Hecke, and M. Wegener, "3D metamaterials," *Nat. Rev. Phys.*, vol. 1, no. 3, pp. 198–210, 2019.

[41] S. Molesky, Z. Lin, A. Y. Piggott, W. Jin, J. Vucković, and A. W. Rodriguez, "Inverse design in nanophotonics," *Nat. Photonics*, vol. 12, no. 11, pp. 659–670, 2018.

[42] A. F. Bower, *Applied Mechanics of Solids*. CRC press, 2010.

[43] B. J. Schwarz and M. H. Richardson, "Experimental modal analysis," *CSI Reliab. week*, vol. 35, no. 1, pp. 1–12, 1999.

[44] N. Mostaghel, "Analytical description of pinching, degrading hysteretic systems," *J. Eng. Mech.*, vol. 125, no. 2, pp. 216–224, 1999.

[45] J. Yu, P. Ziehl, F. Matta, and A. Pollock, "Acoustic emission detection of fatigue damage in cruciform welded joints," *J. Constr. Steel Res.*, vol. 86, pp. 85–91, 2013.

[46] J. W. Fisher, *Fatigue and fracture in steel bridges. Case studies*. 1984.

[47] J. W. Fisher, "Fatigue strength of welded steel beam details and design considerations," 1972.

[48] J. Yu, P. Ziehl, B. Zrate, and J. Caicedo, "Prediction of fatigue crack growth in steel bridge components using acoustic emission," *J. Constr. Steel Res.*, vol. 67, no. 8, pp. 1254–1260, 2011.

[49] C. Ennaceur, A. Laksimi, C. Hervé, and M. Cherfaoui, "Monitoring crack growth in pressure vessel steels by the acoustic emission technique and the method of potential difference," *Int. J. Press. Vessel. Pip.*, vol. 83, no. 3, pp. 197–204, 2006.

[50] C. P. Okeke, A. N. Thite, J. F. Durodola, N. A. Fellows, and M. T. Greenrod, "Modelling of hyperelastic polymers for automotive lamps under random vibration loading with proportional damping for robust fatigue analysis," in *Procedia Structural Integrity*, 2018, vol. 13, pp. 1460–1469.

[51] "Fatigue life prediction of Polymethyl methacrylate (PMMA) polymer under

random vibration loading - ScienceDirect.” [Online]. Available: https://www.sciencedirect.com/science/article/pii/S2452321619302847. [Accessed: 29-Jan-2021].

Chapter 3

3 Seismic Vulnerability Analysis of a Coupled Tank-Piping System by Means of Hybrid Simulation and Acoustic Emission

Abstract

In order to shed light on the seismic response of complex industrial plants, advanced finite element models should take into account both multicomponents and relevant coupling effects. These models are usually computationally expensive and rely on significant computational resources. Moreover, the relationships between seismic action, system response and relevant damage levels are often characterized by a high level of nonlinearity, which requires a solid background of experimental data. Vulnerability and reliability analyses both depend on the adoption of a significant number of seismic waveforms that are generally not available when seismic risk evaluation is strictly site-specific. In addition, detection of most vulnerable components, i.e., pipe bends and welding points, is an important step to prevent leakage events. In order to handle these issues, a methodology based on a stochastic seismic ground motion model, hybrid simulation and acoustic emission is presented in this paper. The seismic model is able to generate synthetic ground motions coherent with site-specific analysis. In greater detail, the system is composed of a steel slender tank, i.e., the numerical substructure, and a piping network connected through a bolted flange joint, i.e., the physical substructure. Moreover, to monitor the seismic performance of the pipeline and harness the use of sensor technology, acoustic emission sensors are placed through the pipeline. Thus, real-time acoustic emission signals of the system under study are acquired using acoustic emission sensors. Moreover, in addition to seismic events, also a severe monotonic loading is exerted on the physical substructure. As a result, deformation levels of each critical component were investigated; and the processing of acoustic emission signals provided a more in-depth view of the damage of the analysed components.

3.1 Introduction

Natural catastrophe can trigger serious consequences in industrial plants, with reference to both structural and non-structural failures resulting in the so-called Natech events [1]. Among other natural catastrophes, seismic events represent a significant share of possible causes.

However, industrial plants are made of an high number of different components with dissimilar characteristics, overall resistances and associated hazards. A very common component of these facilities are pipelines, whose vulnerability becomes an important matter especially when filled with hazardous material, like in petrochemical plants. As a matter of fact, in these circumstances, the failure scenario of a loss of containment (LoC) can result in significant adverse effects on nearby communities and the environment. With reference to LoC prevention, this paper presents an experimental investigation of a realistic tank-piping system in order to assess its seismic performances with a special focus on vulnerable components, like bolted flange joints (BFJs), Tee joints and pipe bends; see [2, 3].

A very useful tool for seismic risk assessment is the performance-based earthquake engineering (PBEE) methodology [4]. According to [5], the PBEE approach is affected by two main sources of uncertainty, i.e., ergodic and non-ergodic uncertainties. More precisely, ergodic variables like seismic intensity measures (IMs) are statistically independent in time domain and, their accuracy, increases with the number of samples. Conversely, structural uncertainties like soil-structure interaction, material characteristics, finite element (FE) models, etc. are not statistically independent or even completely invariant in time; therefore, the averaging of results of the highest possible number of different analyses does not reduce uncertainties propagation. Thus, uncertainties in IMs can be reduced with the adoption of a sufficiently high number of seismic action samples, i.e., ground motion signals. However, the number of natural seismic records is quite limited and, procedures like intensity scaling, can lead to additional errors [6].

Along these lines, in this paper, we present a procedure to reduce both ergodic and nonergodic uncertainties. In particular, ergodic uncertainties are limited with the adoption of synthetic ground motions generated on the underpinning site-specific probabilistic seismic hazard analysis (PSHA) [7]. In order to achieve that, we calibrated the stochastic ground motion model, as formulated by [8], against a set of natural accelerograms compatible with the results of the aforementioned PSHA. On the other hand, non-ergodic uncertainties are reduced by means of experimental data provided by component cyclic testing [9] and hybrid simulation (HS) on a coupled tank-piping

system. Specifically, the hybrid model of the system under study combines numerical (NSs) and physical substructures (PSs). More precisely, following the approach of [10, 11], the steel tank represents the NS and the piping network the PS. Furthermore, in order to both evaluate inelastic phenomena of the piping system and to detect and localize crack events, we employ a set of acoustic emission sensors. This type of sensors is widely used in industrial applications to monitoring pipelines and other types of vessels [12]. As a result, damage levels can also clearly correlate to external loading.

The remainder of the paper is arranged into five main sections. the first one contains a description of the coupled tank-piping system under study while the second one presents the ground motion model of the seismic input. The third section covers in depth the experimental approach used for HS. The fourth section provides information about sensor installation and the use of acoustic emission. Relevant results of the experimental work are provided in the fifth section. Finally, in the last section, main conclusions are drawn and possible future developments are mentioned.

3.2 Case Study

The selected case study is composed of a coupled tank-piping system. In detail, the tank is made by steel and placed unanchored on a concrete foundation, with a height of 14 meters and an 8 meters diameter. The tank is assumed to be filled with oil. Moreover, the tank is connected to the piping network via a bolted flange joint. On the other hand, the piping network is made by API 5L X52 steel, equivalent to the European P355 steel. Besides, it encompasses 8” (outer diameter: 219.08mm; thickness: 8.18mm) and 6” (outer diameter: 168.28 mm; thickness: 7.11mm) schedule 40 pipes. Furthermore, the piping network encompasses several critical components, mainly two elbows, a bolted flange joint, and a Tee joint. The design of the tank-piping system is given in Fig. 3.1.

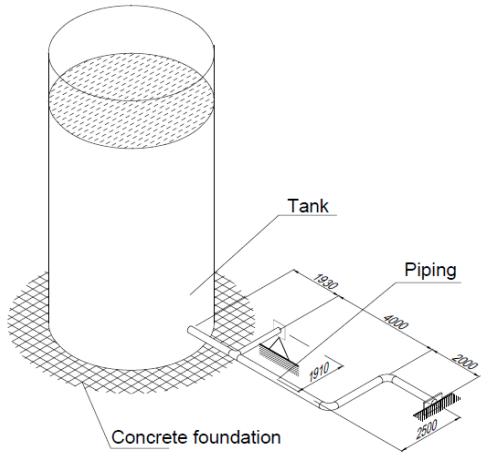

Figure 3.1 Realistic drawing of the tank-piping system and components, measures in mm.

The piping material is P355 steel (Grade X52) with yielding stress of 380 MPa while the fitting steel has a nominal yield stress of 355 MPa. More in detail, the relevant geometric and mechanical characteristics of the Tee joint are given in Table 3.1. Moreover, the internal pressure of the pipeline is kept at 3.2 MPa in order to investigate the pressure effect on the mechanical properties of the joints.

Table 3.1 Mechanical properties and the geometry of the Tee joint

Design	Diameter (mm)	Thickness (mm)	Length (mm)	Material
Main pipe	219.1 (8'')	8.2 (0.32'')	1568 (61.7'')	P355N steel fy = 380 MPa
Branch pipe	168.3 (6'')	7.1 (0.28'')	678 (26.7'')	P355N steel fy = 380 MPa

3.2.1 Seismic Input

Intrinsically, a seismic signal can vary in a several different characteristics scales. For this reason, it is quite difficult to generate a realistic seismic signal. Thus, the characterization of a seismic action requires taking into account an high level of uncertainty. Even though lowering the uncertainty of the seismic input by considering a high number of seismic signals is an option, natural records are limited. For this reason, in order to use a number of seismic signals that are higher than the available set of coherent natural accelerograms, we decided to use synthetic ones. Thus, in this study, we implemented a multi-step procedure to calibrate a stochastic ground motion model in order to generate coherent synthetic ground motions.

As the first step of this procedure, our case study is supposed to be located in Hanford, California (US), and a probabilistic seismic hazard (PSHA) analysis [7] is carried out. The analysis is based on the United States Geological Survey (USGS) database, and the relevant PSHA results are depicted in Fig. 3.2.

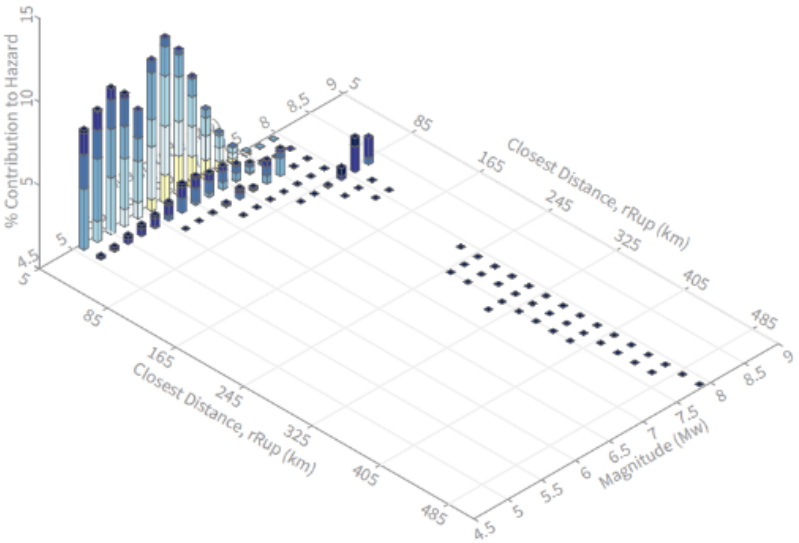

Figure 3.2 Probabilistic seismic hazard deaggregation analysis for Hanford, California (US).

As a result of the deaggregation analysis given in Fig. 3.2, mode values for magnitude (M) and distance from the fault (R) read 6.3 and 10.75 km, respectively. Based on these two values, a set of seven compatible accelerograms is chosen and their relevant R and M values are given in given in Table 3.2.

Table 3.2 Set of compatible accelerograms.

Earthquake Name	Station Name	Magnitude (M)	Distance (R) (km)
Northridge-01	Canoga Park - Topanga Can	6.69	14.7
Northridge-01	Canyon Country - W Lost Cany	6.69	12.44
Northridge-01	N Hollywood - Coldwater Can	6.69	12.51
Northridge-01	Northridge - 17645 Saticoy	6.69	12.09
Northridge-01	Simi Valley - Katherine Rd	6.69	13.42
Northridge-01"	Sun Valley - Roscoe Blvd	6.69	10.05
Northridge01	Sunland - Mt Gleason Ave	6.69	13.35
Northridge02	Pacoima Kagel Canyon	6.05	11.34

As can be seen from Table 2, all the different signals refer to the same event, that is the Northridge earthquake since we prefer to consider a single event in order to limit the variability of the seismic input. In fact, the stochastic ground motion model that we adopt in this work is already capable of generating a sufficient level of variability. More in detail, the model was developed by [8] and generates synthetic ground motions processing 6 different parameters, listed in Table 3.3, by means of the following main expression:

$$a_g(t) = q(t, \boldsymbol{\alpha}) \left[\frac{1}{\sigma_f(t)} \int_{-\infty}^{t} h\big(t - \tau, \boldsymbol{\lambda}(\tau)\big) \omega(\tau) d\tau \right] \tag{3.1}$$

Where $\omega(\tau)$is the baseline white noise while $\hat{\boldsymbol{\alpha}}$ is defined by means of:

$$\hat{\boldsymbol{\alpha}} = arg \min_{\boldsymbol{\alpha}} \left(\left| I_a(t_{45}) - \hat{I}_a(t_{45}) \right| + \left| I_a(t_{95}) - \hat{I}_a(t_{95}) \right| \right) \tag{3.2}$$

Furthermore, $h\big(t - \tau, \boldsymbol{\lambda}(\tau)\big)$, i.e., the Impulse Response Function (IRF) of a linear time-varying filter, can be expressed as follows:

$$h\big(t-\tau,\boldsymbol{\lambda}(\tau)\big)=f(\omega_f,\zeta_f) \tag{3.3}$$

where:

$$\omega_f=\omega_{mid}+\omega'(t-t_{mid}) \tag{3.4}$$

Table 3.3 Model parameters for stochastic ground motion.

I_a	Arias intensity
$D_{5\text{-}95}$	Time interval of 95% of the I_a
t_{mid}	Time at which 45% of the I_a is reached
ω_{mid}	Filter frequency at t_{mid}
ζ_f,	Filter damping ratio (constant)
ω'	Rate of change of the filter frequency with time

Following the calibration process described in [8], we evaluate the model parameters able to generate a set of accelerograms coherent to those listed in Table 3.2. Once these values are calculated, we make two hypotheses in order to define a statistical distribution for each one of the model parameters. The first hypothesis is to consider the parameters statistically uncorrelated. With reference to this, the actual linear correlation coefficients between the different parameters are shown in Fig. 3.3. The second hypothesis is the choice of uniform distributions to describe the probability distribution of all the parameters, with the only exception of ω' that we consider equal to a specific constant value of -0.568 rad/s^2. With regard to the uniformly distributed parameters, their lowest and highest boundaries (LB and UB), set to encompasses all the values retrieved from the aforementioned calibration process, are listed in Table 3.4.

Table 3.4 Distributions of model parameters

Name	Distribution	LB	UB	Units
I_a	Uniform	0.019	3.992	m^2/s^3
D_{5-95}	Uniform	5.083	16.810	s
T_{45}	Uniform	1.596	5.664	s
ω_{mid}	Uniform	14.620	31.000	rad/s
ζ	Uniform	0.074	0.557	-

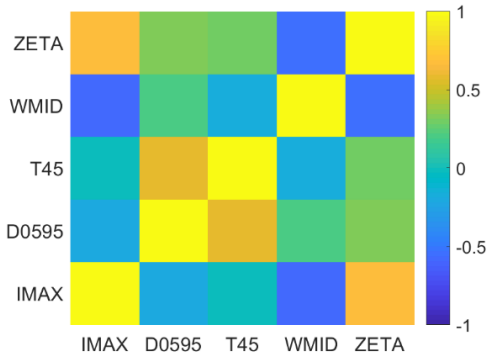

Figure 3.3 Linear correlation of stochastic parameters.

From Fig. 3.3, it can be seen that the hypothesis of uncorrelated parameters is not so dissimilar from reality. Nevertheless, to prepare the experimental campaign, we have to select the proper seismic input taking into account the limited number of tests practically manageable. For this reason, a preliminary step is to reduce the space of these parameters selecting those with the highest influence on the system seismic response. In order to select a simple parameter to identify the seismic response with the maximum sliding displacement of the steel tank, is chosen, see Fig. 3.4 for reference. As a matter of fact, it is straightforward that the sliding displacement a reliable benchmark of the external load on the piping system.

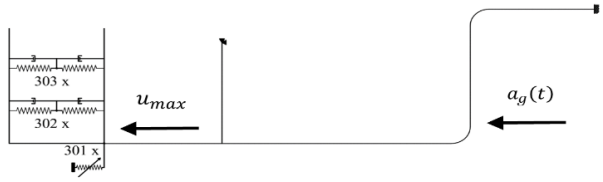

Figure 3.4 Simplified MATLAB FE model, scheme of input/output.

Thus, we present the procedure to perform a global sensitivity analysis (GSA) and select the seismic input for experimental tests as described in [4].

As the first step, once the choice of inputs and outputs, respectively x and y, is done, it is possible to formalize them by means of:

$$x \in X_{ED} = \{I_a, D_{5-95}, T_{45}, \omega_{mid}, \zeta\} \tag{3.5}$$

$$y \in Y_{ED} = u_{max}^{80\%} \tag{3.6}$$

Thus, a set of 2e2 stochastic ground motion model parameters is generated, according to the distributions defined in Table 4, in order to perform a Monte Carlo (MC) analysis with a simplified MATLAB model. However, this set is expanded to a total of 4e4 artificial accelerograms combining each of the 2e2 parameter realizations with 2e2 different baseline noises, ω(τ). A preliminary analysis on a smaller set is realized with a convergence check upon the 80% percentile of the maximum displacements, as depicted in Fig. 3.5. Therefore, a GSA is performed to assess the individual contributions of each input variable to the total variance of the model response. A GSA can be performed with Sobol's decomposition (also called general ANOVA decomposition) of the computational model, which allows one to decompose a full model response in submodels, according to [14].

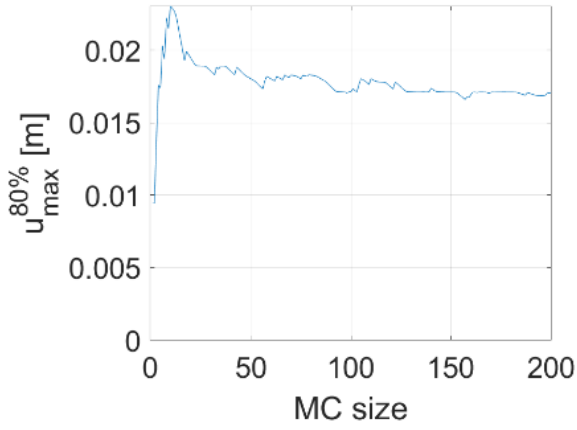

Figure 3.5 Convergence of the 80th percentile of maximum sliding displacement.

The Sobol' index for each subset of input variables $\boldsymbol{u}$ can be written as follows:

$$S_{\boldsymbol{u}} = \frac{D_{\boldsymbol{u}}}{D} \tag{3.7}$$

As stated in [15] polynomial chaos expansion (PCE) methodology provides an effective way to estimate the Sobol' indices by post-processing the polynomial coefficients. The analytical formulation of PCE method can be written as follows:

$$\hat{y}(\boldsymbol{x}) = \mathcal{M}^{PC}(\boldsymbol{x}) = \sum_{\boldsymbol{\alpha} \in \mathcal{A}^{M,p}} y_{\boldsymbol{\alpha}} \Psi_{\boldsymbol{\alpha}}(\boldsymbol{x}) \tag{3.8}$$

Where $\Psi_{\boldsymbol{\alpha}}$ is a multivariate polynomial with multi-index vector $\boldsymbol{\alpha}$, $y_{\boldsymbol{\alpha}}$ is the coefficient of a single multivariate polynomial and $\mathcal{A}^{M,p} = \{\boldsymbol{\alpha} \in \mathbb{N}^M : |\boldsymbol{\alpha}| \leq p\}$ is the truncated set of multi-indices. In particular, the relevant variance can be expressed as:

$$Var[\mathcal{M}^{PC}(\boldsymbol{x})] = \sum_{\substack{\boldsymbol{\alpha} \in \mathcal{A}^{M,p} \\ \alpha \neq 0}} y_{\boldsymbol{\alpha}}^2 \tag{3.9}$$

By means of Eq. (7) and (9) we can write Total Sobol' indices as:

$$\hat{S}_i^{T,PC} = \frac{\sum_{\boldsymbol{\alpha}\in\mathcal{A}_i^T} \hat{y}_{\boldsymbol{\alpha}}^2}{\sum_{\substack{\boldsymbol{\alpha}\in\mathcal{A} \\ \boldsymbol{\alpha}\neq\mathbf{0}}} \hat{y}_{\boldsymbol{\alpha}}^2}, \quad \mathcal{A}_i^T = \{\alpha \in \mathcal{A} : \alpha_i > 0\} \tag{3.10}$$

Finally, the relevant values of Sobol' indices evaluated by Eq. (3.10) are shown in Fig. 3.6:

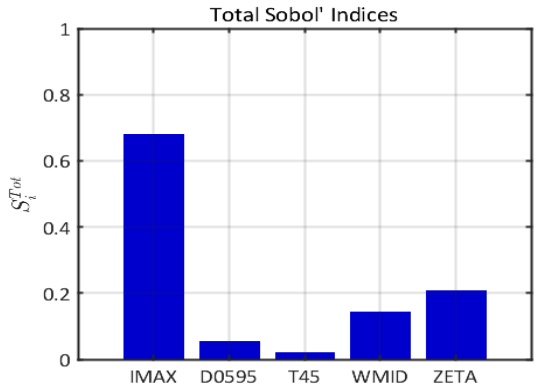

Figure 3.6 Total Sobol' indices.

From Fig. 3.6 it is possible to notice that three parameters generate most part of the output variance, i.e. I_a, ω_{mid} and ζ. This is somehow expected since they represent the most significant part of the intensity of accelerograms physical effects. Besides, based on GSA results, these three parameters are chosen to vary according to the statistical distributions defined in Table 4, while the remaining three are fixed at their average value, as reported in Table 3.5.

Table 3.5 Constant parameters.

Name	Value	Units
D_{5-95}	10.441	s
T_{45}	3.700	s
$\dot{\omega}$	-0.568	rad/s^2

According to these modified distributions, a new set of 4e4 artificial accelerograms is therefore generated combining 2e2 parameter realizations with 2e2 different baseline noises. Thus, from this set of artificial accelerograms, seven signals are selected to be tested with hybrid simulation. Among them, 4 are chosen to keep the system in the linear

regime, equivalent to service limit state (SLS), and 3 to go slightly in non-linear regime to investigate ultimate limit state (ULS). This categorization is made upon u_{max}, by setting $u_{max} < 0.04\ m$ for SLS signals and $u_{max} > 0.06\ m$ for ULS ones. The relevant spectral accelerations of these 7 accelerograms are depicted in Fig. 3.7 with SLS signals in blue and ULS in red.

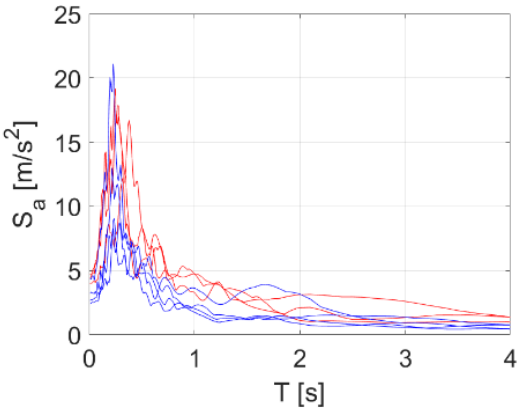

Figure 3.7 Spectral accelerations of ULS (red) and SLS (blue) synthetic ground motions

More precisely, we selected an SLS signal, depicted in Fig. 3.8, with a PGA of 3.14 m/s^2 to be tested with hybrid simulation. We decided to adopt a low intensity signal in order to not induce any yielding into our system. As a matter of fact, we relied on the monotonic test to study the plastic behavior of the PS.

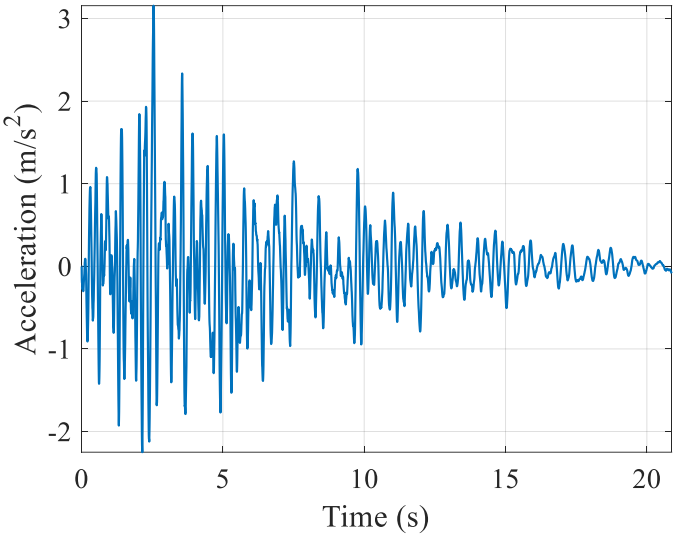

Figure 3.8 Seismic Input Signal used for Hybrid Simulation

3.2.2 Experimental Setup and Hybrid Simulations

The experimental approach relies on the hybrid simulation technique [10]. More precisely, the unanchored tank is simulated via a numerical substructure (NS). Thus, the transfer system, i.e. a 250 kN MTS actuator, enforces the compatibility between the NS and the physical substructure (PS) represented by the piping system. The PS is shown in Figs. 3.9-3.11.

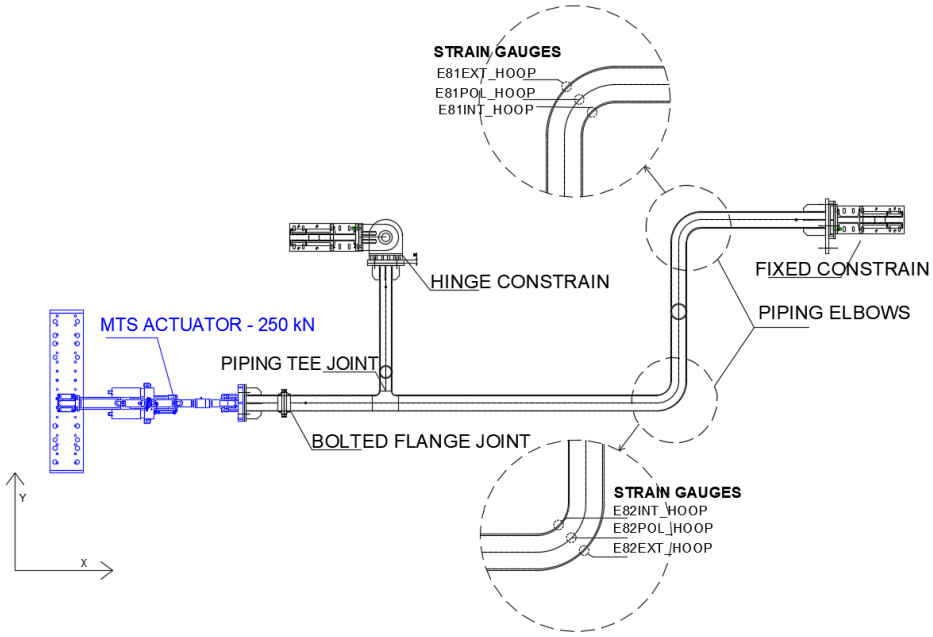

Figure 3.9 Experimental setup configuration consisting of the physical substructure and the transfer system

Figure 3.10 Experimental setup consisting of the physical substructure and the transfer system.

a) b) (c)

Figure 3.11 Close up view of the experimental components. a) bolted flange joint, b) piping elbow and (c) Tee joint

Furthermore, the NS model is built with a simplified approach based on [16]. Along this line, the simplified tank model is given in Fig. 3.12 and the relevant parameters are reported in Table 3.6.

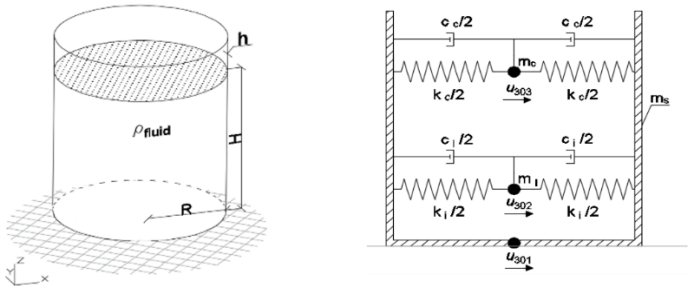

Figure 3.12 Simplified tank model after [16].

Table 3.6 Simplified tank model parameters.

Parameter	Value	Unit
E	210	GPa
ρ_{fluid}	900	kg/m^3
ρ_{tank}	7850	kg/m^3
c_c	1690	Ns/m
c_i	1930×10^3	Ns/m

H	14	m
R	4	m
m_t – steel tank mass	1.65×10^4	kg
m_l – liquid mass	6.33×10^5	kg
m_c – convective mass	7.98×10^4	kg
m_i – impulsive mass	5.47×10^5	kg

For clarity, the main scheme of hybrid simulation is shown in Fig. 3.13.

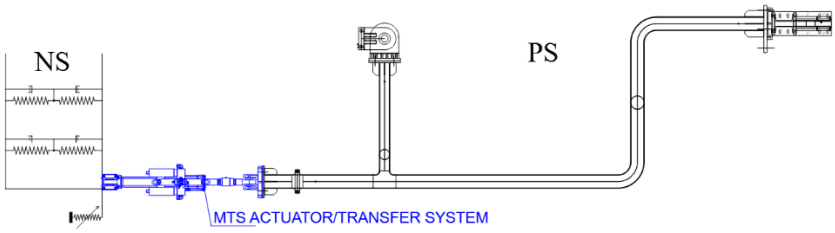

Figure 3.13 Scheme of the hybrid simulation.

The sliding effect at the base of the tank is modelled by a friction contact model between the tank bottom and the concrete foundation. More precisely, the friction effect is implemented into the NS through the bilinear Mostaghel model [17]. In this respect, the main equations of the Mostaghel's model read,

$$\begin{cases} \dot{r} = \left(\alpha_{MST}k_{MST} + (1-\alpha_{MST})k_{MST}\left(\bar{N}(v)\bar{M}(s-\delta_{MST}) + M(v)N(s+\delta_{MST})\right)\right)v, \\ \dot{u} = v \end{cases} \tag{3.11}$$

where the parameter s and the remaining functions $N, M, \bar{N}$ and $\bar{M}$ are defined as follows:

$$s = \frac{r - \alpha_{MST}k_{MST}u}{(1-\alpha_{MST})k_{MST}} \tag{3.12}$$

$$
\begin{aligned}
N(v) &= 0.5\big(1 + sgn(v)\big)\Big(1 + \big(1 - sgn(v)\big)\Big) \\
M(v) &= 1 - N(v) \\
\bar{N}(v) &= M(-v) \\
\bar{M}(v) &+ N(-v)
\end{aligned}
\tag{3.13}
$$

Furthermore, parameters k_{MST}, α_{MST} and δ_{MST} represent initial stiffness, post-yielding stiffness reduction factor, and yielding displacement of the idealized mechanical model, respectively. In order to replicate the friction phenomenon, these parameters are set as,

$$
\begin{aligned}
\delta_{MST} &= \Delta = 1e-3\ m \\
\alpha_{MST} &= 1e-3 \\
k_{MST} &= \frac{\mu(m_l + m_t)g}{\Delta} = 2.18e+8\frac{N}{m}.
\end{aligned}
\tag{3.14}
$$

For the sake of clarity, both a mechanical model and the entailing hysteretic behavior of the degrading system formalized by [17][44], is shown in the following figure.

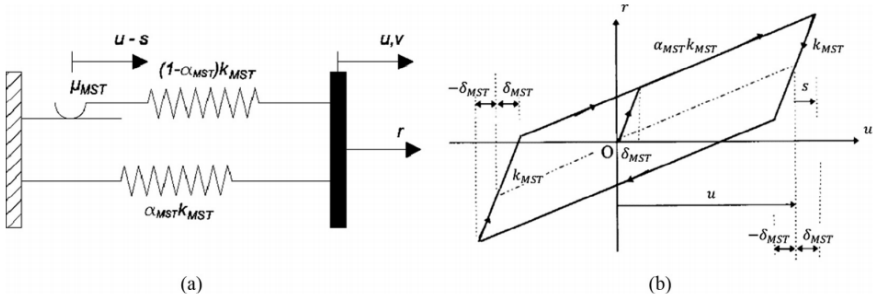

Figure 3.14 Bilinear Mostaghel's model [17]: (a) SDoF idealization; (b) Hysteretic loop.

More specifically, we assumed a friction coefficient for the interaction between steel and concrete equal to $\mu=0.1$, according to [18].

With regard to time integration adopted in HS, we relied on the Partitioned Generalized (PG-α) algorithm [11]. It allows to decouple the computation time between NS and PS and assures the compatibility of velocities between the two domains by means of Localized Lagrange Multipliers. Moreover, the solution of the NS is evaluated through a linearly implicit predictor-corrector approach based on the trapezoidal rule with $\gamma=0.5$, $\beta=0.25$ and $\alpha=0$.

In order to carry out HSs, both mass and stiffness matrices were used to model the NS by means of the MATLAB/Simulink code in the Host PC. The Host PC compiles the system of equations discretized in time by the Partitioned PG-α algorithm [11] which are then sent to an xPC target -a real time operating system installed in a target PC- via a LAN connection. During HS, the integration algorithm solves the equations of motion in the xPC target and estimates a displacement command for the PS. It is written in the xPC target, and this signal is instantaneously copied in the MTS controller through SCRAMNET -a reflective memory between the Host PC and the MTS controller-. The controller then commands the actuator to move the coupling DoF to the desired position. Again, the SCRAMNET memory instantaneously supplies the corresponding restoring force measured by a load cell to the xPC target, as depicted in Fig. 3.15.

A comparison between the target displacement computed and the measured one is used to assess the performance of the HS. In particular, the absolute ratio between the residual measured distance to the target displacement and the starting displacement position is calculated at each step. Thus, in order to guarantee an accurate solution within the actuator electronics limitations, a maximum value of 10-4 is imposed for this ratio. Finally, a partitioned integration based on Localized Lagrange Multipliers (LLM) is used to enforce kinematic compatibility between velocities, at the interface between PS and NS [11].

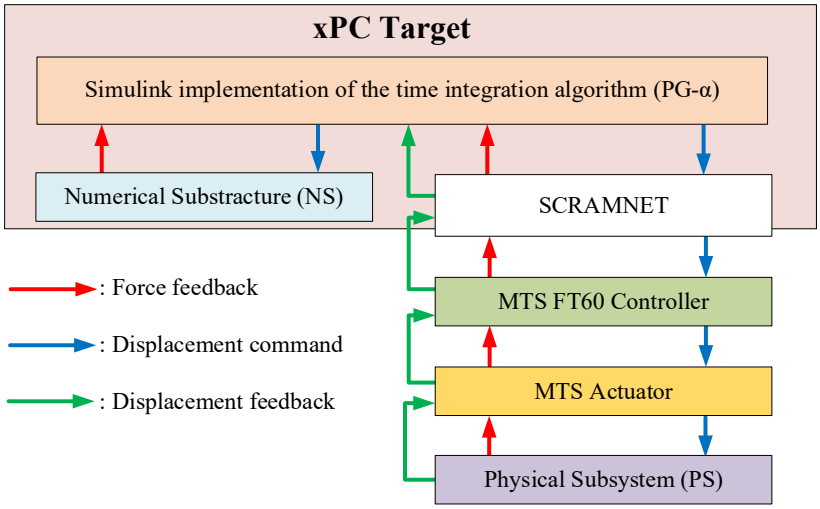

Figure 3.15 Transfer system and signals in the hybrid simulation.

3.2.3 Acoustic Sensor Installation

The piping system consists of three main critical components: i) a Tee joint; ii) Elbow #1; iii) Elbow #2. These components can experience stress concentrations during earthquake events due to both their geometry and their welding connections to the main pipeline. As a matter of fact, this study focuses on low-cycle fatigue of Tee joints and piping elbows while other components, like bolted flange joints, are found to be less vulnerable to this limit state [2]. Clearly, the LoC limit state is very important for a piping performance, but it is out of the scope of this paper.

Acoustic emission tests are carried out using an AMSY6 acoustic emission system, including 12 VS150 sensors with 150 kHz resonant frequency, provided from Vallen Systeme GmbH. The sensors are attached to the pipeline components using a couplant liquid alongside with magnetic spring clips or adhesive tape as indicated in Fig. 3.16.

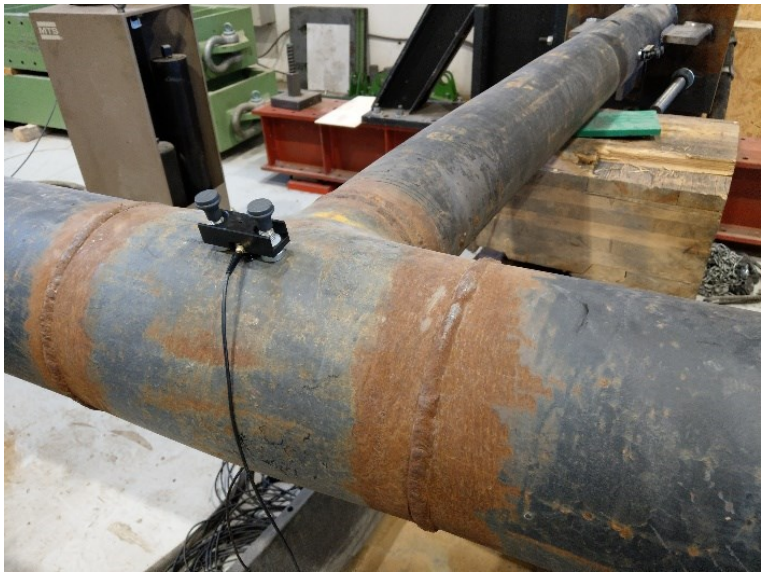

Figure 3.16 Acoustic sensor installation on the Tee joint. Typical MAG4M magnetic spring clips used to attach the VS150 sensor on the pipeline.

The exact placement of the sensors is illustrated in Fig. 3.17. Moreover, the acoustic emission events are measured and recorded in real time, including emission signals (hits), normalized energy, time of the event, rise time, and other relevant measures.

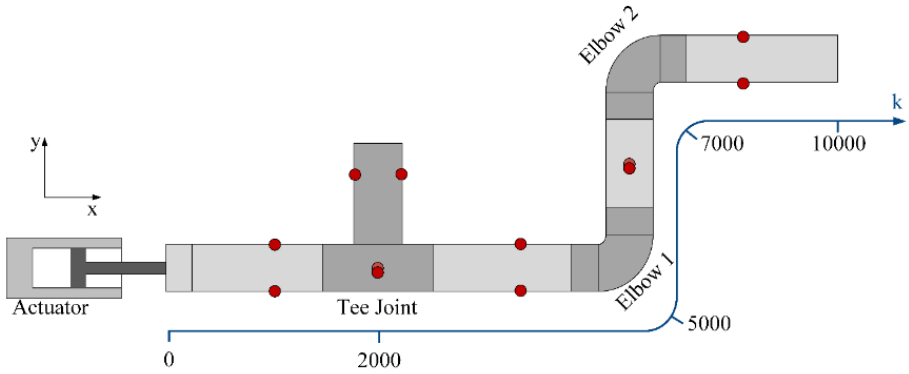

Figure 3.17 Top view illustration of the pipeline. Red points correspond to the acoustic emission sensors. Dimensions in mm.

3.3 Results

3.3.1 Acoustic Emission

The Tee joint, Elbow #1, and Elbow #2 components are linked to the main pipeline by means of welded connections. Naturally, weldments involve high residual stresses and more defects with respect to a monolithic component [45]. Hence, welded connections subjected to cyclic or dynamic loading can exhibit fatigue sensitive characteristics while flaws can trigger crack growth [46], [47]. Moreover, crack formation and its relevant growth mechanism can be detected and evaluated with a proper analysis of acoustic emission signals [48]. More precisely, in this study we measured acoustic emissions of the tank-piping system both during a seismic event and a monotonic loading. As a result, the evaluation of acoustic emission signals provided information about the health status of critical component connections as well as dislocation and deformation mechanisms of the pipe.

3.3.2 Hybrid Simulation

The response of the piping system is firstly examined by means of hybrid simulation using a synthetic ground motion record, i.e. the one depicted in Fig 3.8. Moreover, the total duration of HS took sixteen minutes during which acoustic emissions signals were collected. The relationship between the acoustic emission events and displacements entailed by seismic input is illustrated in Fig. 3.18.

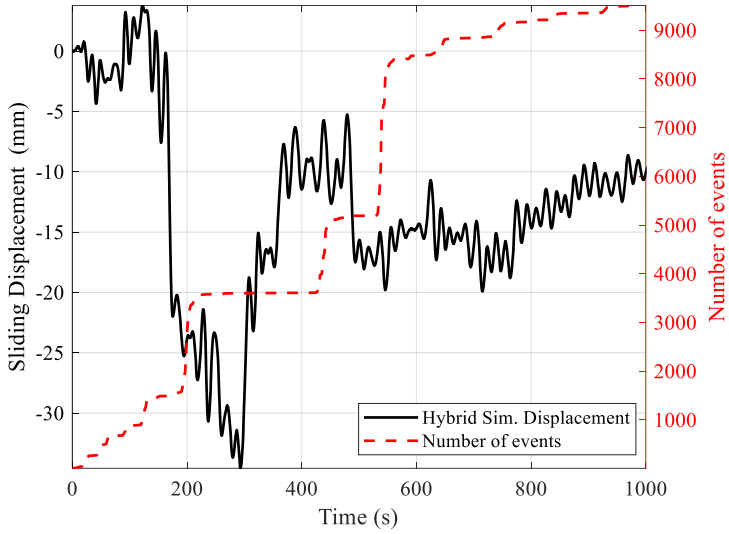

Figure 3.18 Trends of displacements provided by hybrid simulation and acoustic emission events.

One can notice from Fig. 3.18 that the number of acoustic emission signals proportionally increases with the longitudinal displacement of the pipeline system; this is a clear indication that the pipeline displacement triggers the deformation mechanisms through the pipeline material. Thus, in order to better understand the damage status of critical components, a volumetric monitoring approach is adopted with reference to Tee joint and Elbow #1 depicted in Fig. 3.17. This approach is aimed at detecting and localizing cracks with an increased accuracy. As a matter of fact, test results show that most of the acoustic emissions are concentrated in welding connections of the examined components. More precisely, the collected acoustic emission signals and their locations for Tee joint and Elbow #1, are presented in Fig. 3.19 and 3.20, respectively. Hence, relying on the emission signals data, the Tee joint is found to experience a higher level of deformation compared to Elbow #1.

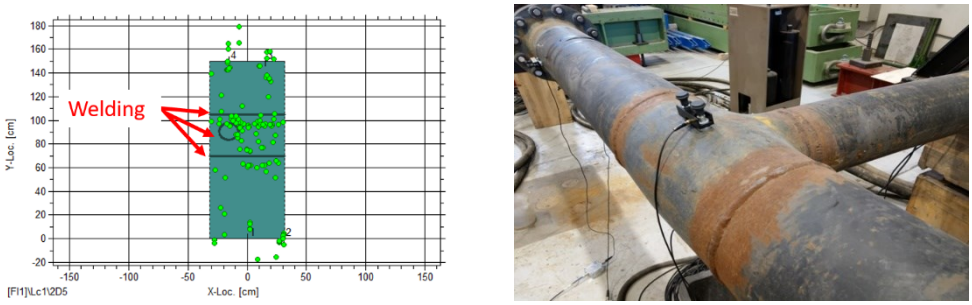

Figure 3.19 Green points show acoustic emission signals detected on the Tee joint during the HS tests (left). Tee joint component (right).

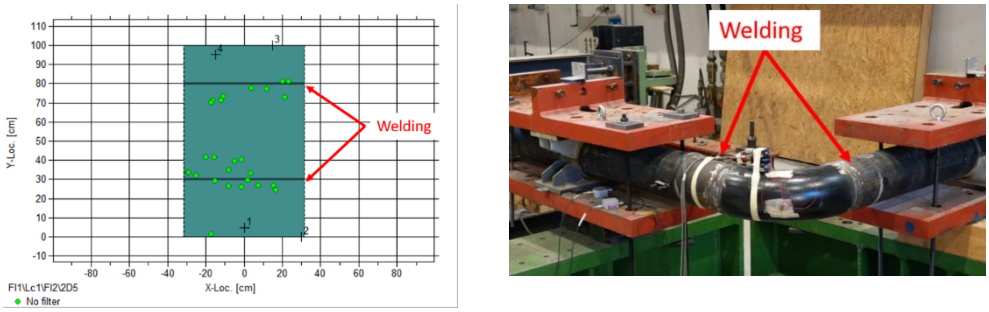

Figure 3.20 Acoustic emission signals detected on Elbow #1 (left). Elbow #1 component (right).

In order to reach a deeper understanding of the performance of both Tee joint and Elbow #1 time-dependent emission signals are represented the frequency domain using the Fast Fourier Transform. The entailing mean frequency versus the total duration of each signal is reported in Fig. 3.21 too.

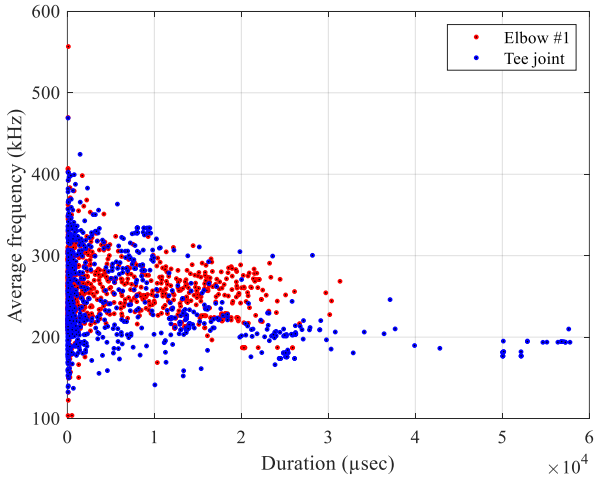

Figure 3.21 Comparison of the events mean frequencies and durations of Tee joint and Elbow #1.

A careful reader can notice that both Tee joint and Elbow #1 generate signals with a wide range of frequency values and different duration times. As a matter of fact, experimental data underline longer event durations for the Tee joint given to a large amount of welded connections subjected to damage.

3.3.3 Monotonic Test

In order to reach the collapse limit state, the piping system was subjected to a monotonic test. More precisely, the system was loaded by means of the transfer system up to 190 kN, corresponding to a maximum total displacement of 470 mm. The relevant loading-displacement relationship including the cumulative number of relevant acoustic events is depicted in Fig. 3.22. A good correlation between the two set of data exist especially when the piping components enter in the plastic regime.

Furthermore, in order to understand the level of critical components damage occurred during the monotonic test, the location of acoustic emission events was investigated. Along this line, we divided the pipeline in 100 mm segments along the k-direction as shown in Fig 3.17. Thus, for each segment, the total number of acoustic emission signals is evaluated and relevant event densities are depicted

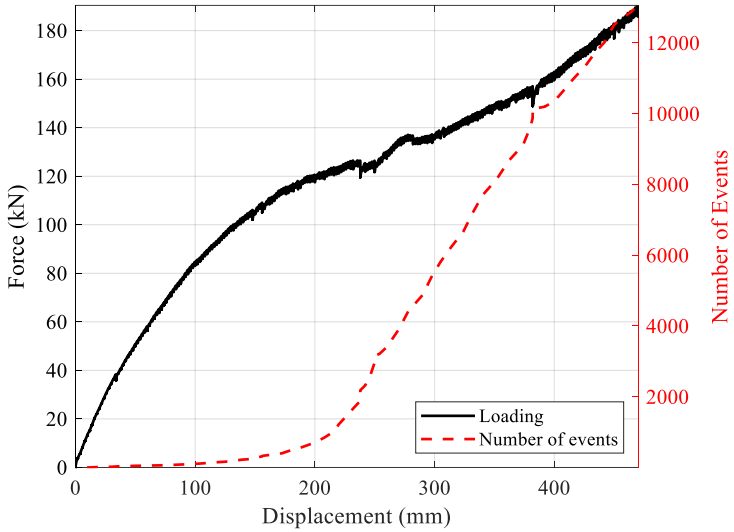

Figure 3.22 Loading-displacement relationship of the piping system including the cumulative number of relevant acoustic events

in Fig. 3.23 Both the Tee joint and Elbow #2 result to be the most damaged components.

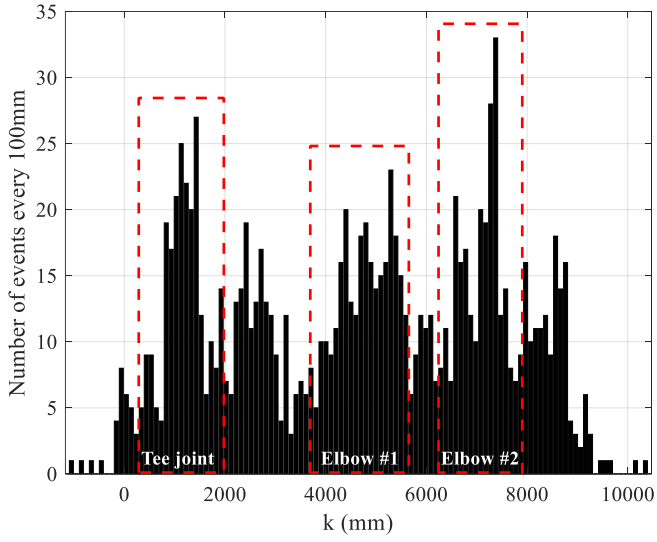

Figure 3.23 Location-dependent number of events.

Moreover following [49], we analyzed in depth plasticity mechanisms in the pipeline. Therefore, the relationship between events amplitude and the total number of crack events, depicted in Fig. 24, was used to define both elastic and plastic regions all the way

through. As a result, one can observe the first motion of dislocations, called Plasticity #1, that exhibit low amplitude emissions of about 78 dB. The following events, grouped as Plasticity #2, were observed after 600 seconds with a maximum peak amplitude of about 100 dB. Differently from the Plasticity #1 phase, dislocation mechanisms of the material lose their importance in the Plasticity #2 phase. Thus, liberation of dislocations, trigger permanent deformations through the piping system and significant deformations start. Furthermore, after the beginning of the Plasticity #2 region, the number of event activities exhibit a rapid increment. This trend can be correlated to the overall pipeline stiffness decrease with respect to the initial stiffness shown in Fig 22.

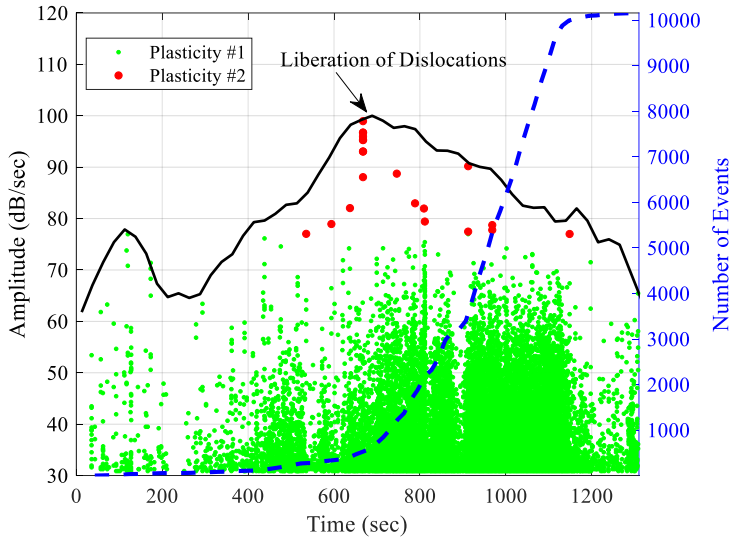

Figure 3.24 Plasticity evaluation of the piping system subjected to monotonic loading.

3.4 Conclusions

In this article, we presented a methodology capable of assessing the vulnerability characteristics of a realistic tank-piping system based on hybrid simulation, synthetic ground motions and acoustic emission analysis. In particular, we focused on the performance of vulnerable components of the piping network. As a first step, we considered a seismic scenario that is associated with a geographical site using a probabilistic seismic hazard analysis. On this basis, we identified a seismic input by means of a stochastic ground motion model. In addition, in order to reach the collapse limit state of the piping system, a monotonic loading case was also considered. During both loading cases, the acoustic emission detection and localization was carried out during the experiments. Based on the performance evaluation of critical components based on acoustic emission events, the Tee joint resulted to be the most damaged component for the hybrid simulation case whilst Elbow #2 was the most damaged component for the monotonic case. Thus, the acoustic emission technique let us to gather more in-depth information about damage level of critical components as well as the plasticity level of the piping system. This opens the way to collect a library of acoustic emission events for the classification of vulnerable component and to refine our finite elements models for future studies.

References

1. Cruz, A.M., Steinberg, L.J., Vetere-Arellano, A.L.: Emerging issues for natech disaster risk management in Europe. J. Risk Res. 9, 483–501 (2006). doi:10.1080/13669870600717657

2. Bursi, O.S., di Filippo, R., La Salandra, V., Pedot, M., Reza, M.S.: Probabilistic seismic analysis of an LNG subplant. J. Loss Prev. Process Ind. 53, 45–60 (2018). doi:10.1016/j.jlp.2017.10.009

3. Caputo, A.C., Paolacci, F., Bursi, O.S., Giannini, R.: Problems and perspectives in seismic Quantitative Risk Analysis of chemical process plants. J. Press. Vessel Technol. 141, (2019)

4. Cornell, C.A. and Krawinkler, H.: Progress and Challenges in Seismic Performance Assessment, (2000)

5. Der Kiureghian, A.: Non-ergodicity and PEER's framework formula. Earthq. Eng. Struct. Dyn. 34, 1643–1652 (2005). doi:10.1002/eqe.504

6. Julian J. Bommer, A.B.A.: The Use Of Real Earthquake Accelerograms As Input To Dynamic Analysis. J. Earthq. Eng. Imp. Coll. Press. 8, 43–91 (2004). doi:10.1080/13632460409350521

7. Baker, J.W.: An Introduction to Probabilistic Seismic Hazard Analysis. (2008)

8. Sanaz Rezaeian, A.D.K.: Simulation of synthetic ground motions for specified earthquake and site characteristics. Earthq. Eng. Struct. Dyn. 39, 1155–1180 (2010). doi:10.1002/eqe

9. Vincenzo La Salandra, Rocco Di Filippo, Oreste S. Bursi, Fabrizio, S.A.P.: Cyclic Response of Enhanced Bolted Flange Joints for Piping Systems. In: ASME 2016 Pressure Vessels & Piping Conference (2016)

10. Abbiati, G., La Salandra, V., Bursi, O.S., Caracoglia, L.: A composite experimental dynamic substructuring method based on partitioned algorithms and localized Lagrange multipliers. Mech. Syst. Signal Process. 100, 85–112 (2018). doi:10.1016/j.ymssp.2017.07.020

11. Abbiati, G., Lanese, I., Cazzador, E., Bursi, O.S., Pavese, A.: A computational framework for fast-time hybrid simulation based on partitioned time integration and state-space modeling. Struct. Control Heal. Monit. 26, e2419 (2019)

12. Brownjohn, J.M.W.: Structural health monitoring of civil infrastructure. Philos. Trans. R. Soc. A Math. Phys. Eng. Sci. 365, 589–622 (2007). doi:10.1098/rsta.2006.1925

13. Di Filippo, R., Abbiati, G., Sayginer, O., Covi, P., Bursi, O.S., Paolacci, F.: Numerical surrogate model of a coupled tank-piping system for seismic fragility analysis with synthetic ground motions. In: American Society of Mechanical Engineers, Pressure Vessels and Piping Division (Publication) PVP. American Society of Mechanical Engineers (ASME) (2019)

14. Sobol' IM. Sensitivity estimates for nonlinear mathematical models. Math Modeling Comput Exp;1:407–14. 1993.

15. Stefano Marelli, B.S.: a Framework for Uncertainty Quantification in MATLAB. Vulnerability, Uncertainty, Risk ©ASCE 2014. 2554–2563 (1996)

16. Malhotra P. K., Wenk. T., Wieland M., 2000. Simple Procedure for Seismic Analysis of Liquid-Storage Tanks. Structural Engineering International, 3/2000, pp. 197-201.

17. Mostaghel, N.: Analytical description of pinching, degrading hysteretic systems. J. Eng. Mech. 125, 216–224 (1999)

18. Gorst, N. J. S., J., W. S., Pallett, P. F. & Clark, L. A. (2003): Friction in temporary works. Research report. Shool of Engineering, The University of Birmingham, Health and Safety Executive, Publication no. 071, Birmingham.

19. Yu, J., Ziehl, P., Matta, F., Pollock, A.: Acoustic emission detection of fatigue damage in cruciform welded joints. J. Constr. Steel Res. 86, 85–91 (2013). doi:10.1016/j.jcsr.2013.03.017

20. Fisher, J.W.: Fatigue and fracture in steel bridges. Case studies. (1984)

21. Fisher, J.W.: Fatigue strength of welded steel beam details and design considerations. (1972)

22. Yu, J., Ziehl, P., Zrate, B., Caicedo, J.: Prediction of fatigue crack growth in steel bridge components using acoustic emission. J. Constr. Steel Res. 67, 1254–1260 (2011). doi:10.1016/j.jcsr.2011.03.005

23. Ennaceur, C., Laksimi, A., Hervé, C., Cherfaoui, M.: Monitoring crack growth in pressure vessel steels by the acoustic emission technique and the method of potential difference. Int. J. Press. Vessel. Pip. 83, 197–204 (2006). doi:10.1016/j.ijpvp.2005.12.004

Chapter 4

4 Supplementary Topics

In this chapter, four supplementary topics are presented to contribute to the previous chapters and also to demonstrate further methodologies regarding sensor design studies. The content of the four topics is summarized as follows:

- The first topic presents the mathematical derivation of the thin film optical filters using the transfer matrix method.
- The second topic introduces a novel design and optimization approach for thin-film optical filters using the Genetic algorithm.
- The third topic presents an additional design and simulation work for the frequency tuning of the sensing approach that was given in Chapter 1.
- The fourth topic presents the geometric improvements for frequency tuning of the sensor design that was given in Chapter 2.

4.1 Modeling of Thin Film Optical Filters using the Transfer Matrix Method

4.1.1 Abstract

Thin-film optical filters are key components in the fields of optics and photonics. Thanks to their simple and reliable properties, these filters are becoming increasingly popular in numerous areas such as monitoring, sensing, communication, etc. For this reason, modelling of the thin film optical filters plays an important role in the development stages of novel devices. The Transfer Matrix Method is a well-known approach to calculate electromagnetic interactions amongst the layers of thin films.

In this topic, the physical background of thin-film optical filters is reviewed and the mathematical derivation of the Transfer Matrix Method is presented. In order to calculate the transmission and the reflection characteristics of a thin film optical filter, a programming scheme is developed. The program supports wavelength-dependent material properties, incident angle modifications, and complex refractive indices. The code structure is constructed to design periodic as well as arbitrarily distributed layers throughout this thesis work.

Background

The Transfer Matrix Method (TMM) is an effective route to calculate the propagation of electromagnetic waves in different dielectric media. The TMM is widely used in the modelling of fiber Bragg gratings, design of thin-film optical filters and it is also used in acoustic and mechanical systems [1], [2]. There are several studies in the literature that explain the theory and the mathematical background of the TMM [3]–[9]. On the other hand, coding and implementation of the TMM have been provided in several studies using various programming tools including MATLAB [5]. Thus, in this topic, the physical meaning and the mathematical derivation of TMM are presented. Based on these derivations, a custom code script was developed and used through the thesis which supports the calculation of transmittance and reflectance, including arbitrarily distributed layers, wavelength-dependent complex refractive indices, and modifications in the incident angle.

4.1.2 The Transfer Matrix Method Formulation

An electromagnetic wave propagating from air to the multiple thin-film layers is illustrated in Figure 1. The incident wave is split into two different components which are reflected and transmitted waves (medium absorptions are neglected.). Through each layer, internal reflections reveal at both boundaries of each layer except the last layer where the light leaves the system. The last layer of the system shows reflection in the exit direction only.

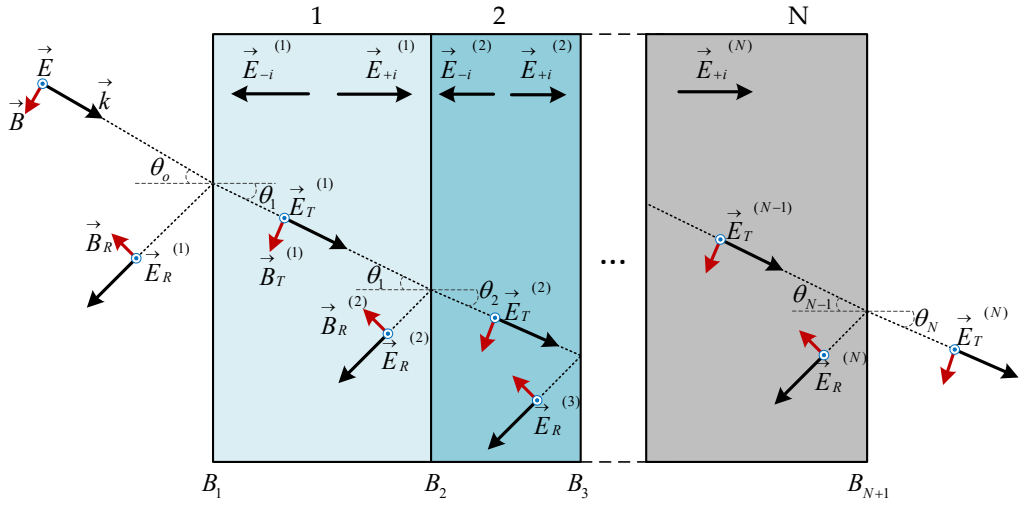

Figure 4.1 Propagation of the light through different material mediums is illustrated. The black-colored arrows represent wave vectors, red arrows show magnetic fields and blue components are electric fields. Incoming wave splits into two main components which are reflected (R subscripted terms) and transmitted fields (T subscripted terms). Furthermore, at each layer, internal reflections occur in the same and opposite direction of the light (-i and +i subscripted terms).

The electric field equilibrium at each medium boundary can be written as in (4.1).

$$
\begin{aligned}
&\vec{E}_{B_1} : \vec{E} + \vec{E}_R^{(1)} = \vec{E}_T^{(1)} + \vec{E}_{-i}^{(1)} \\
&\vec{E}_{B_2} : \vec{E}_{+i}^{(1)} + \vec{E}_R^{(2)} = \vec{E}_T^{(2)} + \vec{E}_{-i}^{(2)} \\
&\vec{E}_{B_3} : \vec{E}_{+i}^{(2)} + \vec{E}_R^{(3)} = \vec{E}_T^{(3)} + \vec{E}_{-i}^{(3)} \\
&\vdots \\
&\vec{E}_{B_{N+1}} : \vec{E}_{+i}^{(N-1)} + \vec{E}_R^{(N)} = \vec{E}_T^{(N)}
\end{aligned}
\tag{4.1}
$$

where $\vec{k}$ is wave vector, $\vec{E}$ is the incoming electric field, B subscripts represent the boundaries between two adjacent media, R subscript represents the reflected components, T subscript represents the transmitted component, $+i$ subscripts indicate the internal electric field in the direction of incoming electric field and $-i$ subscripts indicate the internal electric field in opposite direction to the incoming electric field, the superscript of each component represents the layer encompassing the electromagnetic wave with N being the total number of the layers.

Similar to (1), the corresponding magnetic field equilibrium can be written as shown in (4.2).

$$
\begin{aligned}
&\vec{B}_{B_1} : \vec{B}\cos\theta_0 - \vec{B}_R^{(1)}\cos\theta_0 = \vec{B}_T^{(1)}\cos\theta_1 - \vec{B}_{-i}^{(1)}\cos\theta_0 \\
&\vec{B}_{B_2} : \vec{B}_{+i}^{(1)}\cos\theta_1 - \vec{B}_R^{(2)}\cos\theta_1 = \vec{B}_T^{(2)}\cos\theta_2 - \vec{B}_{-i}^{(2)}\cos\theta_1 \\
&\vec{B}_{B_3} : \vec{B}_{+i}^{(2)}\cos\theta_2 - \vec{B}_R^{(3)}\cos\theta_2 = \vec{B}_T^{(3)}\cos\theta_3 - \vec{B}_{-i}^{(3)}\cos\theta_2 \\
&\vdots \\
&\vec{B}_{B_{N+1}} : \vec{B}_{+i}^{(N-1)}\cos\theta_{N-1} - \vec{B}_R^{(N)}\cos\theta_{N-1} = \vec{B}_T^{(N)}\cos\theta_N
\end{aligned}
\tag{4.2}
$$

where $\vec{B}$ variable represents the magnetic field components, θ corresponds to the incident angle of each field component and its subscript corresponds to the layer number. The incident angle at the boundary of each medium can be calculated using Snell's law given in (4.3).

$$n_{N-1}\sin\theta_{N-1} = n_N \sin\theta_N \tag{4.3}$$

where, n is the refractive index of each material layer.

$$B^{(N)} = n_N E^{(N)}\sqrt{\varepsilon_0\mu_0} \tag{4.4}$$

where $\varepsilon_0 = 8.85\times10^{-12}$ is the permittivity of free space and $\mu_0 = 4\pi\times10^{-12}$ is the permeability of free space.

$$\gamma_N = n_N \cos\theta_N \sqrt{\varepsilon_0\mu}_0 \tag{4.5}$$

When the relationship between the electric field and the magnetic is considered as given in (4.4) and then imposing a variable γ_L (4.5) in order to simplify the calculations, the set of equations introduced in (4.2) can be rewritten as in (4.6).

$$\begin{aligned}
&\vec{B}_{B_1} : \gamma_0(\vec{E} - \vec{E}_R^{(1)}) = \gamma_1(\vec{E}_T^{(1)} - \vec{E}_{+i}^{(1)}) \\
&\vec{B}_{B_2} : \gamma_1(\vec{E}_T^{(1)} - \vec{E}_R^{(2)}) = \gamma_2(\vec{E}_T^{(2)} - \vec{E}_{+i}^{(2)}) \\
&\vec{B}_{B_3} : \gamma_2(\vec{E}_T^{(2)} - \vec{E}_R^{(3)}) = \gamma_3(\vec{E}_T^{(3)} - \vec{E}_{+i}^{(3)}) \\
&\vdots \\
&\vec{B}_{B_{N+1}} : \gamma_{(N-1)}(\vec{E}_T^{(N-1)} - \vec{E}_R^{(N)}) = \gamma_N(\vec{E}_T^{(N)} - \vec{E}_{+i}^{(N)})
\end{aligned} \tag{4.6}$$

The phase difference (4.7) between the internal reflections and transmitted electric fields can be expressed as in (4.8).

$$\delta_N(\lambda) = \frac{2\pi n_N t_N \cos\theta_N}{\lambda} \tag{4.7}$$

$$\vec{E}_{+i}^{(N)} = \vec{E}_T^{(N)} e^{-i\delta_N} \tag{4.8}$$

where t is the thickness of corresponding layers and δ is the phase difference. Thus, by changing the variables and applying further simplifications (4.9), the electric field and the magnetic field equilibriums can be simplified as a set of equations in (4.10).

$$\begin{aligned} \vec{E}_T^{\,(N)} &= \vec{E}_T^{\,(N-1)} e^{-i\delta_N} + \vec{E}_{+i}^{\,(N-1)} e^{i\delta_N} \\ \vec{E}_T^{\,(N)} &= \vec{E}_T^{\,(N-1)} e^{-i\delta_N} + \vec{E}_T^{\,(N-1)} e^{-i\delta_N} e^{i\delta_N} = \vec{E}_T^{\,(N-1)} (1 + e^{-i\delta_N}) \end{aligned} \tag{4.9}$$

$$\begin{aligned} &\vec{E}_{B_1} : \vec{E} + \vec{E}_R^{\,(1)} = \vec{E}_T^{\,(1)} + \vec{E}_{-i}^{\,(1)} \\ &\vec{E}_{B_2} : \vec{E}_{+i}^{\,(1)} + \vec{E}_R^{\,(2)} = \vec{E}_T^{\,(2)} + \vec{E}_{-i}^{\,(2)} \\ &\vec{E}_{B_3} : \vec{E}_{+i}^{\,(2)} + \vec{E}_R^{\,(3)} = \vec{E}_T^{\,(3)} + \vec{E}_{-i}^{\,(3)} \\ &\vdots \\ &\vec{E}_{B_{N+1}} : \vec{E}_{+i}^{\,(N-1)} + \vec{E}_R^{\,(N)} = \vec{E}_T^{\,(N)} \end{aligned} \tag{4.10}$$

$$\begin{aligned} &\vec{B}_{B_1} : \gamma_0 (\vec{E} - \vec{E}_R^{\,(1)}) = \gamma_1 (\vec{E}_T^{\,(1)} - \vec{E}_{+i}^{\,(1)}) \\ &\vec{B}_{B_2} : \gamma_1 (\vec{E}_T^{\,(1)} - \vec{E}_R^{\,(2)}) = \gamma_2 (\vec{E}_T^{\,(2)} - \vec{E}_{+i}^{\,(2)}) \\ &\vec{B}_{B_3} : \gamma_2 (\vec{E}_T^{\,(2)} - \vec{E}_R^{\,(3)}) = \gamma_3 (\vec{E}_T^{\,(3)} - \vec{E}_{+i}^{\,(3)}) \\ &\vdots \\ &\vec{B}_{B_{N+1}} : \gamma_N (\vec{E}_T^{\,(N-1)} - \vec{E}_R^{\,(N)}) = \gamma_N (\vec{E}_T^{\,(N)} - \vec{E}_{+i}^{\,(N)}) \end{aligned}$$

Finally, the equations set in (4.10), can be simplified in the matrix form (4.11) which is showing the electric and magnetic fields at any boundary (subscript of B_x indicates the boundary layer) of the layers.

$$\begin{pmatrix} \mathrm{E}_{B_x} \\ \mathrm{B}_{B_x} \end{pmatrix} = \begin{pmatrix} \cos\delta_N & \dfrac{i\sin\delta_N}{\gamma_N} \\ i\gamma_N \sin\delta_N & \cos\delta_N \end{pmatrix} \begin{pmatrix} \mathrm{E}_{B_x}^{\,(N)} \\ \mathrm{B}_{B_x}^{\,(N)} \end{pmatrix} = \mathrm{M} \begin{pmatrix} \mathrm{E}_{B_x}^{\,(N)} \\ \mathrm{B}_{B_x}^{\,(N)} \end{pmatrix} \tag{4.11}$$

where the matrix M can be calculated for multiple layers as given in (4.12).

$$\mathrm{M} = \prod_{b=1}^{N} \mathrm{M}^{(b)} \tag{4.12}$$

Transmittance and reflectance can be defined as in (13) and (14), respectively.

$$t \equiv \frac{\vec{E}_T^{\,(N)}}{\mathrm{E}} \tag{4.13}$$

$$r \equiv \frac{\vec{E}_R^{\,(N)}}{\mathrm{E}} \tag{4.14}$$

Moreover, the transmission and the reflection can be calculated in percentage as shown through (4.15) and (4.16), respectively.

$$T(\lambda) = 100|t|^2 = 100\left(\left|\frac{2\cdot\gamma_1}{\gamma_1\cdot(\mathrm{M})_{1,1} + \gamma_1\cdot\gamma_N\cdot(\mathrm{M})_{1,2} + (\mathrm{M})_{2,1} + \gamma_N\cdot(\mathrm{M})_{2,2}}\right|\right)^2 \tag{4.15}$$

$$R(\lambda) = 100|r|^2 = 100\left(\left|\frac{\gamma_1\cdot(\mathrm{M})_{1,1} + \gamma_1\cdot\gamma_N\cdot(\mathrm{M})_{1,2} - (\mathrm{M})_{2,1} - \gamma_N\cdot(\mathrm{M})_{2,2}}{\gamma_1\cdot(\mathrm{M})_{1,1} + \gamma_1\cdot\gamma_N\cdot(\mathrm{M})_{1,2} + (\mathrm{M})_{2,1} + \gamma_N\cdot(\mathrm{M})_{2,2}}\right|\right)^2 \tag{4.16}$$

4.2 Design and Optimization of Thin Film Optical Filters

4.2.1 Abstract

In this topic, an automated design and optimization framework for thin-film optical filters is presented. A genetic algorithm (GA) was used together with a transfer matrix model to determine the best combination of the design parameters such as layer thicknesses, material selection, number of layers, layer distributions, etc. to find a structure that satisfies pre-defined design objectives.

The GA is a stochastic search algorithm that mimics the nature of biological evolution. Similar to nature, GA relies on chromosome exchange between each individual and the survival of a stronger chromosome. Similar to the chromosome of an organism, also each design structure owns a variable vector that consists of design parameters. Thus, the selection of the best combination among the design variables is managed by GA. The operation flowchart of the GA framework is shown in Fig. 4.2.

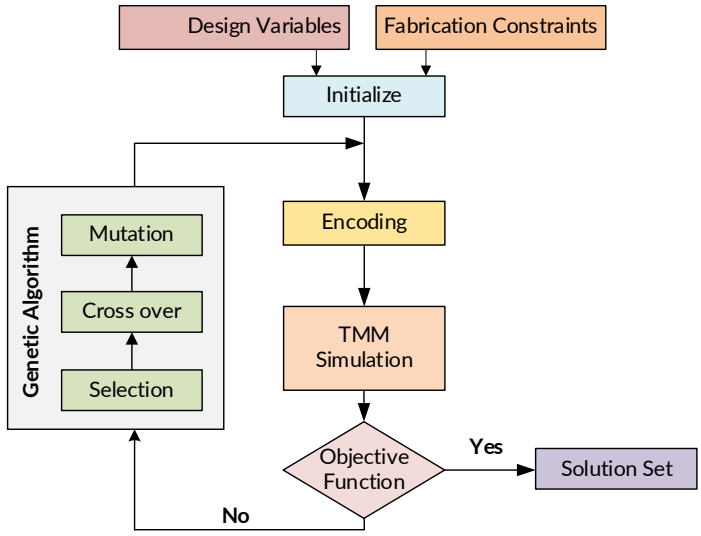

Figure 4.2 Operation flowchart of the GA optimization framework.

Some of the important operation steps of the GA optimization framework can be summarized as follows:

Initialization:

- Design parameters are embedded into a vector format which is called a chromosome.
- If there is an initial solution parameter, it can be defined at this stage. Depending on the initial parameters, GA performance and convergence can be improved.

Encoding:

- The variable vector is mapped to the simulation model (TMM).
- This operation provides a coupling between the GA and a simulation model.

Simulation:

- A variable vector embedded simulation is calculated via TMM.
- Simulation results are converted to a solution vector which will be plugged into the GA.
- The simulation is an important process that defines the overall system performance and accuracy.

Objective Function:

- An objective function is a mathematical function that defines the design objectives of a design problem.
- It is also called cost function, merit function, or fitness function
- The mathematical expression of the objective function plays a crucial role in the convergence and accuracy of the optimization framework.

4.2.2 Studies and Results

4.2.2.1 Hybrid Cavity at 1.55 um

In this part, the design of a hybrid Bragg filter with a cavity peak at 1.55 um is presented. The initial design configuration was defined as 5 different sets of Bragg filters where each Bragg contains four couples of SiO_2 and TiO_2. Thus, in total 10 number of design variables are defined. The search space was defined considering the fabrication limitations. Therefore the thickness value of each design variable is limited from a minimum thickness of 10 nm to a maximum of 300 nm. The objective function was defined to obtain a resonance peak at 1.5 um with the highest possible transmittance value. Moreover, the neighborhood of the cavity peak is defined to have as small as possible transmittance values. In other words, the optimizer was forced to obtain a high-quality factor peak at a flat bandgap. The details of the objective function are given in Fig. 4.3. In addition to that, Fig. 4.4 shows the design configuration and the thickness values that were found through the optimization work.

$$\textbf{given} \quad t = \langle t_1, t_2 \ldots t_{10} \rangle \quad , \quad \{ t \mid t \in \mathbb{Z} \}$$
$$\textbf{minimize} \quad f(t,\lambda) = \max \left[size(T(\lambda_{Zero}) > 0.3) \quad \left| (10 - T(\lambda_{Peak}) \right| \right]$$
$$\textbf{subject to} \quad 10 \le t \le 300$$

Figure 4.3 Objective function for the design of a hybrid Cavity structure at 1.55 um

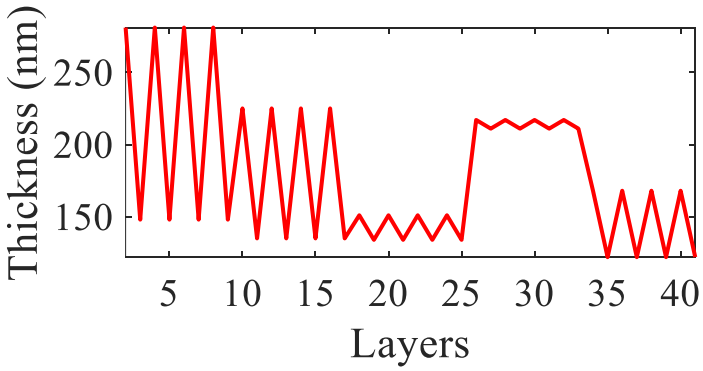

Figure 4.4 Thickness distribution of the material layers. (The odd-numbered layers correspond to TiO_2 while the even-numbered layers are SiO_2 except the first and the last layers which are air and a substrate respectively.)

The corresponding transmittance response of this system is shown in Fig. 4.4.

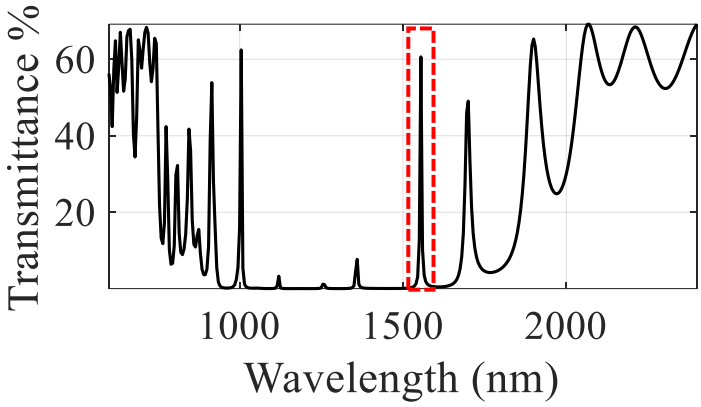

Figure 4.5 Transmittance of the given design spectrum.

The transmittance graph shows a resonance peak at 1.55 um and relatively flat bandgap properties. However, this result can be improved by extending the design degrees of freedom of the system. For instance, the use of different material layers, extending the number of layers, or changing the thickness limit of each layer can possibly result in a better set of solutions.

4.2.2.2 Notch Filter Design for 780 nm

In this optimization framework, a notch filter at 780 nm is studied. The initial structure design was considered with an alternating SiO_2 and TiO_2 layers. The number of coupled layers and the thickness of each layer at a couple was chosen as a design variable. Similar to the previous study, the thickness value of each design variable is limited from a minimum thickness of 10 nm to a maximum of 300 nm. In addition, the number of couples is limited from 1 to 15. In other words, the system is limited by the maximum total number of 30 layers. It is also worth noting that, all design parameters were constrained to take an integer value since the number of layers cannot be decimal nor to fabricate a layer with a decimal thickness is not feasible.

In order to obtain low transmittance values with a narrow bandgap around 780 nm, the objective function was defined as in Fig. 4.6. More in detail, the objective function was defined to perform the following operations:

i. Calculate transmittance values in the range from 775 nm to 785 nm with a step size of 2 nm.
ii. Find the number of elements that are less than 5%.
iii. Minimize the total number of elements. (Try to lower all transmittance values below 5%)

$$
\begin{aligned}
&\textbf{\textit{given}} \begin{cases} t=\langle t_1, t_2, N\rangle \quad , \quad \{t \mid t \in \mathbb{Z}\} \\ N \quad , \quad \{N \mid N \in \mathbb{Z}\} \\ \lambda_{Notch} = [775{:}785] \end{cases} \\
&\textbf{\textit{minimize}} \quad f(t, N, \lambda) = size(T(\lambda_{Notch}) \leq 5) \\
&\textbf{\textit{subject to}} \quad 10 \leq t \leq 300 \quad , \quad 1 \leq N \leq 15
\end{aligned}
$$

Figure 4.6 Objective function to design a notch filter at 780 nm

The layer configuration of a final notch filter is given in Fig 4.7. The refractive index distribution of the layers is shown in Fig. 4.9.

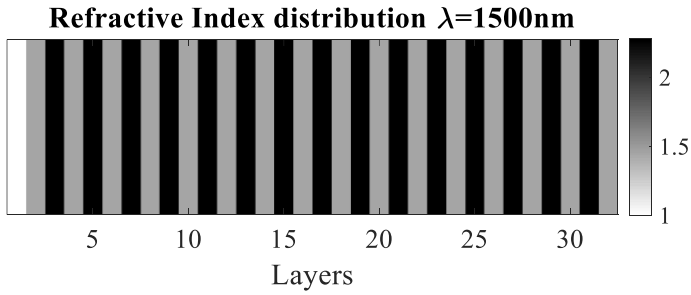

Figure 4.7 Layer configuration of the notch filter design. Dark-colored layers represent TiO_2 while the gray-colored layers are SiO_2. The first and the last layers correspond to air and a silica substrate respectively.

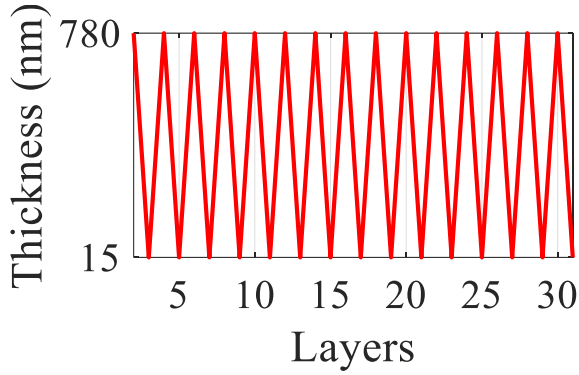

Figure 4.8 Thickness distribution of the material layers. (The odd-numbered layers correspond to TiO_2 while the even-numbered layers are SiO_2 except the first layer which is the substrate.)

The notch filter sample was fabricated using RF sputtering and characterized through similar fabrication and spectrum measurement protocols that were mentioned in Chapter 1 and Chapter 2. The simulation and measurement results are compared in Fig. 4.9.

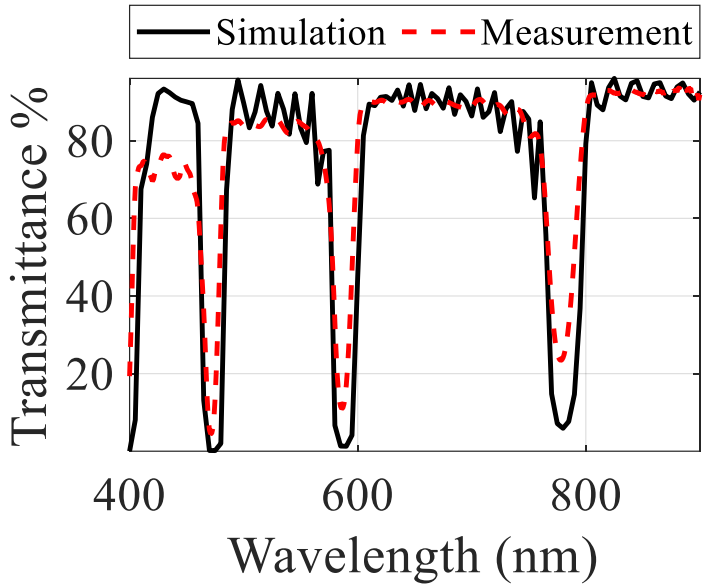

Figure 4.9 Comparison of the design results to a fabricated sample

4.2.2.3 Sensitivity improvement of tunable spectral filter-based sensors

An optimization framework is performed for the sensitivity improvement of a tunable spectral filter system that was introduced in Chapter 2. In this context, three different design studies are presented. The highlights of this study can be listed as follows:

- A reflector and a filter were configured as given in Chapter 2.
- Sensor response is derived through the overlapping optical response of the filter and the reflector using the Trapezoidal rule.
- The reflection angle of the reflector was swept from 0° to 5°.
- Change in the overlapping area over the angle sweep was defined as the sensor response.
- The sensor sensitivity (m) was defined as the slope of the sensor response curve.
- Throughout the optimization work, the value of sensor sensitivity (m) was aimed to be maximized.
- Both optical components were assumed as identical.

1st Design Study

In the first design approach, the thickness of each SiO_2 and TiO_2 layer and the total number of couple layers are considered as design variables. The thickness range of the TiO_2 and SiO_2 was limited from 5 nm to 100 nm and from 5 nm to 600 nm respectively. The total number of layers is a limited maximum of up to 10 couples. The difference between the overlapping area at 0° and 5° is aimed at to be maximized. The objective function is given in Fig. 4.10.

$$\textbf{\textit{given}} \quad t = \left\langle t_{SiO_2}, t_{TiO_2}, N \right\rangle \quad , \quad \left\{ t \middle| t \in \mathbb{Z} \right\}$$

$$\textbf{\textit{minimize}} \quad f(t, N, \lambda) = -\left| A_{0^\circ} - A_{5^\circ} \right|$$

$$\textbf{\textit{subject to}} \quad 5 \le t_{SiO_2} \le 600 \quad , \quad 5 \le t_{TiO_2} \le 100 \quad , \quad 1 \le N \le 10$$

Figure 4.10 Objective function

The optimization framework was computed with a population size of 30 individuals. The calculations were stopped since the maximum convergence tolerance was reached at MATLAB defaults. The convergence graph of this first design study is given in Fig. 4.11.

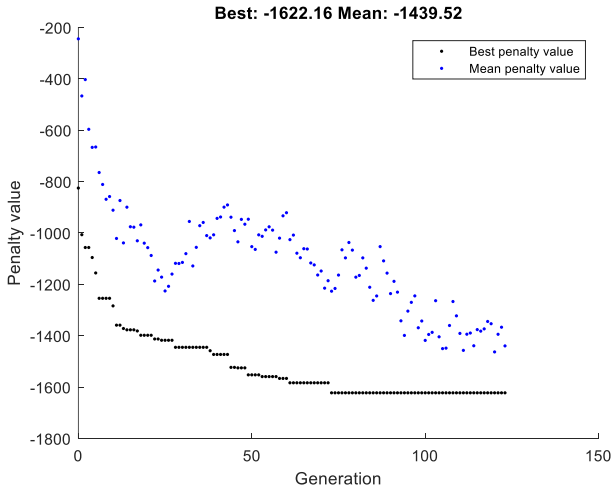

Figure 4.11 Convergence plot of 1st design study

The optimization process resulted in the total number of 9 couples varying thicknesses from 37 nm to 405 nm for TiO_2 and SiO_2 respectively. Details of the layer configuration are given in Fig. 4. 12.

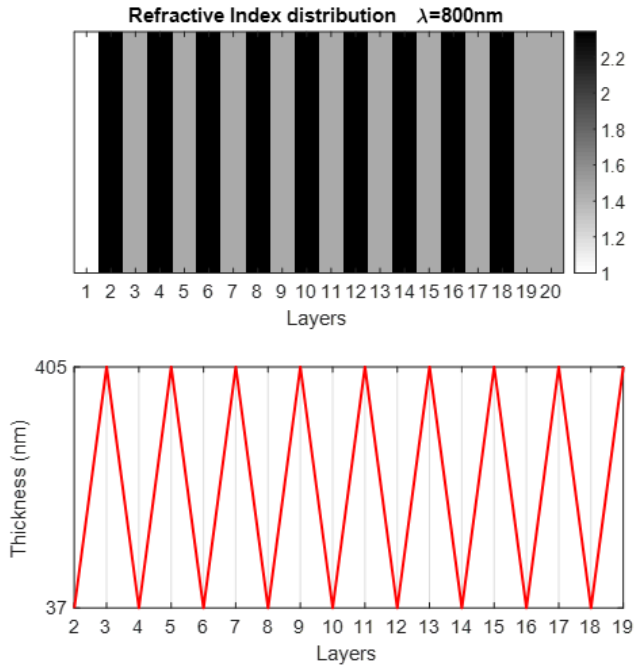

Figure 4.12 Layer configuration of the first optimization study. Top: Dark-colored layers represent TiO_2 while the gray-colored layers are SiO_2. The first and the last layers correspond to air and a silica substrate respectively. Bottom: Thickness distribution of the material layers. (The odd-numbered layers correspond to TiO_2 while the even-numbered layers are SiO_2 except the first layer which is the substrate.).

The optical orientation of the reflector and filter is given in Fig. 4.13. The intersecting area in between the transmission and the reflection is calculated via the Trapezoidal rule. The reflection angle of the reflector was swept from 0° to 5° with an increment size of 0.5°and all area calculations were repeated. The change in the area with respect to the angle sweep is plotted in Fig. 4.13. The sensor sensitivity was found about m=325.

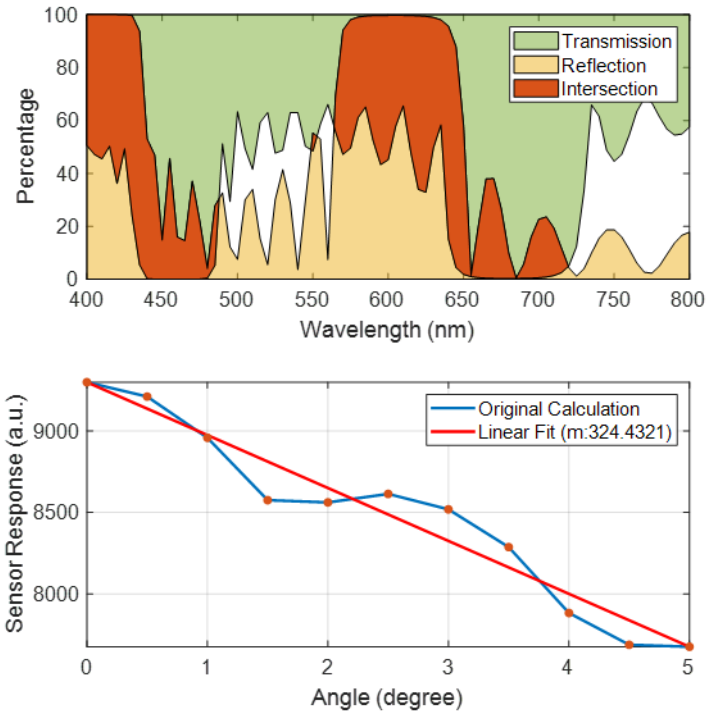

Figure 4.13 Top: The optical configuration at an incident angle at 0°. Bottom: Change in the intersection area of the optical spectrum from 0° to 5°with the increment size of 0.5°.

2nd Design Study

In the second design study, a different objective function was developed. The design degree of freedom of the optical structure was increased by introducing material layers with independently distributed thickness values. More precisely, the total number of 10 material layers were distributed in the initial design, starting from the substrate site with an alternating order of SiO_2 and TiO_2 layers respectively. The thickness range of the TiO_2 and SiO_2 was limited from 5 nm to 100 nm and from 5 nm to 600 nm respectively.

Using an intuition from the 1st study, the increment in the number of bandgaps can increase the overlapping area between the filter and reflector. In other words, a sawtooth-like structure is the best candidate for maximization of the overlapping area for per unit angle change between two optical components. For this reason, the objective function is defined, considering the sensor sensitivity, number of bandgaps (k), and bandgap amplitudes (P). More in detail, the objective function is given in Fig. 4.15.

$$
\begin{aligned}
&\textbf{\textit{given}}\begin{cases} t = \left\langle t_{SiO_2(1)}, t_{TiO_2(2)} \ldots, t_{TiO_2(10)} \right\rangle \quad , \quad \left\{ t \middle| t \in \mathbb{Z} \right\} \\ P = [P_1 \quad P_2 \quad \ldots \quad P_k] \quad , \quad P_m = \dfrac{1}{k}\sum_{i=1}^{k} P_i \end{cases} \\
&\textbf{\textit{minimize}} \quad f(t, N, \lambda) = \max\left(\left\lceil \left| 150 - m \right| \quad \left| 60 - P \right| \quad P_m \times \left| k - 2 \right| \right\rceil \right) \\
&\textbf{\textit{subject to}} \quad 5 \le t_{SiO_2} \le 600 \quad , \quad 5 \le t_{TiO_2} \le 100 \quad , \quad k = 10
\end{aligned}
$$

Figure 4.14 Objective function for the second design study

The optimization framework was computed with a population size of 30 individuals. The calculations were stopped since the user-defined maximum generation number was reached. The convergence graph of this first design study is given in Fig. 4.15.

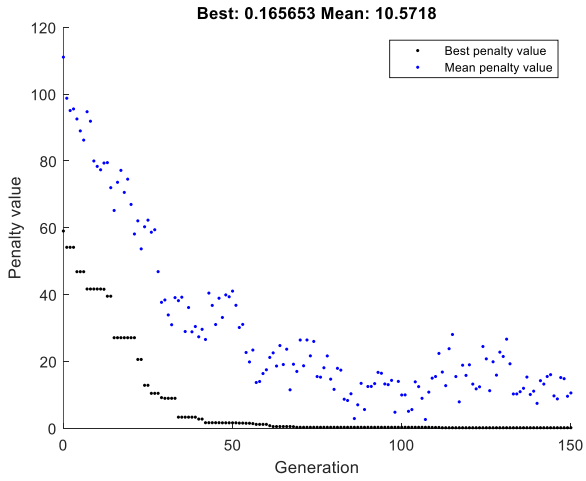

Figure 4.15 Convergence plot of 2nd design study.

The optimization process resulted in a total number of 10 layers with thickness distribution of each layer independently. Details of the layer configuration are given in Fig. 4. 16.

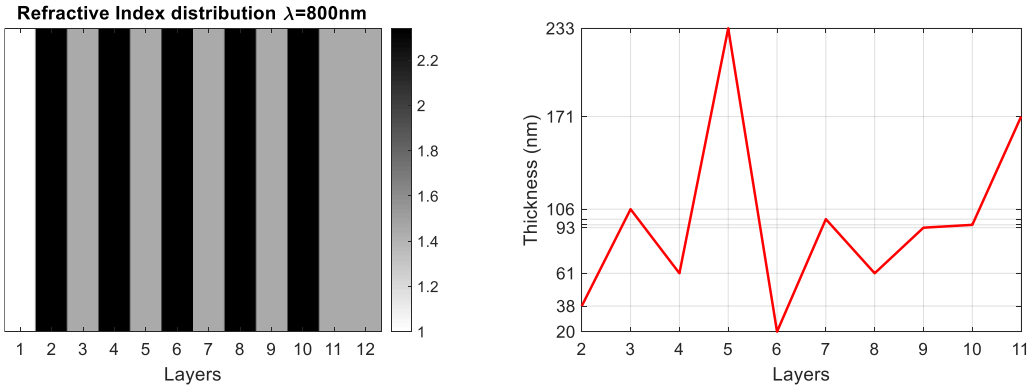

Figure 4.16 Layer configuration of the second design study. Left: Dark-colored layers represent TiO_2 while the gray-colored layers are SiO_2. The first and the last layers correspond to air and a silica substrate respectively. Right: Thickness distribution of the material layers. (The odd-numbered layers correspond to TiO_2 while the even-numbered layers are SiO_2 except the first layer which is the substrate.).

The sensor response was determined using the same approach that was performed also in the first study. The spectral configuration of two optical components shows two

bandgap peaks as it was defined in the objective function. Moreover, the sensor response shows m=150 which is lower with respect to the first study. However, sensor transfer function shows a linear trend and also the number of layers is lower than the first study that brings an advantage of easier fabrication. Results are shown in Fig. 4.17.

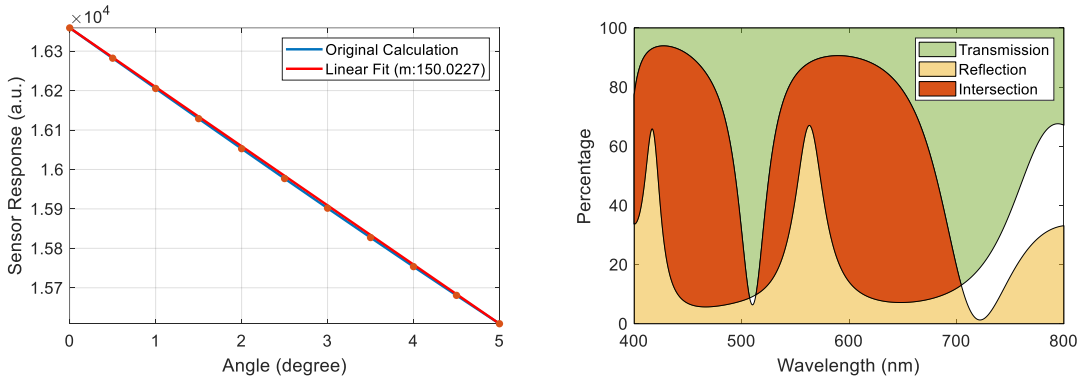

Figure 4.17 Left: The optical configuration at the incident angle of 0°. Right: Change in the intersection area of the optical spectrum from 0° to 5°with the increment size of 0.5°.

3rd Design

In the third design study, the initial design was kept as similar to the second study but the optimization parameters were slightly changed. The objective function was tuned by changing the weights to achieve higher sensitivity by forcing the optimizer to create four bandgaps with lower bandwidths. The updated objective function is given in Fig. 4.18.

$$
\begin{aligned}
&\textbf{\textit{given}}\begin{cases} t = \left\langle t_{SiO_2(1)}, t_{TiO_2(2)} \ldots, t_{TiO_2(10)} \right\rangle \quad , \quad \left\{ t \middle| t \in \mathbb{Z} \right\} \\ P = [P_1 \quad P_2 \quad \ldots \quad P_k] \quad , \quad P_m = \dfrac{1}{k}\sum_{i=1}^{k} P_i \end{cases} \\
&\textbf{\textit{minimize}} \quad f(t, N, \lambda) = \max\left(\left[\left| 900 - m \right| \quad \left| 50 - P \right| \quad P_m \times \left| k - 4 \right| \right] \right) \\
&\textbf{\textit{subject to}} \quad 5 \le t_{SiO_2} \le 600 \quad , \quad 5 \le t_{TiO_2} \le 100 \quad , \quad k = 10
\end{aligned}
$$

Figure 4.18 Objective function for the third study

The optimization framework was computed with the population size of 30 individuals. The calculations were stopped since the user-defined maximum generation number was reached. The convergence graph of this first design study is given in Fig. 4.15.

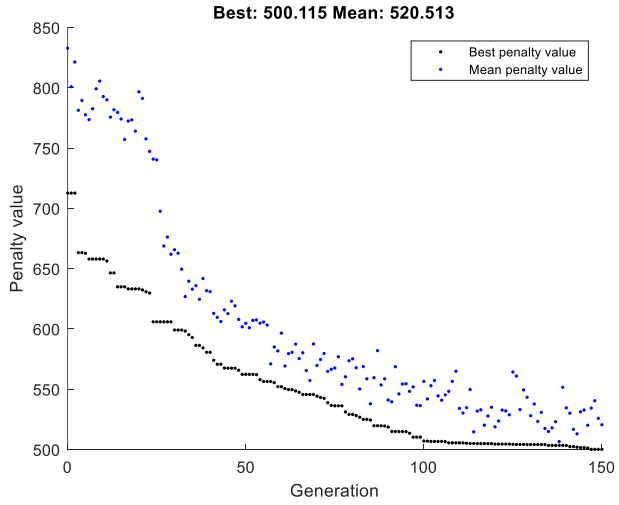

Figure 4.19 Convergence plot of 3rd design study.

The optimization process resulted in a total number of 10 layers with thickness distribution of each layer independently. Details of the layer configuration are given in Fig. 4. 16.

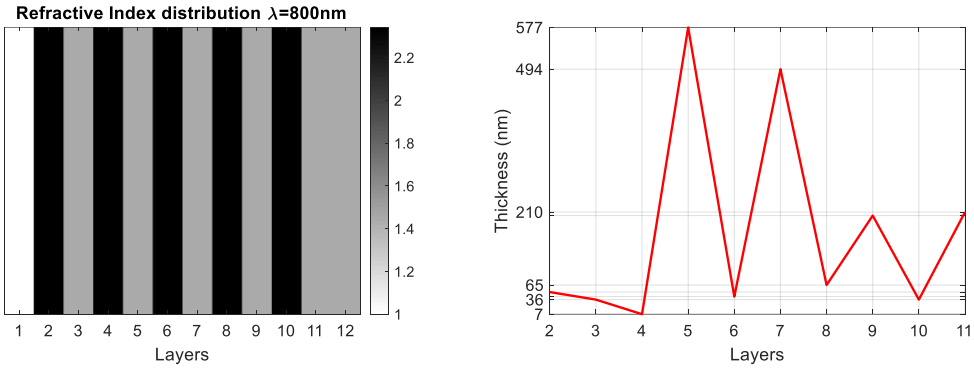

Figure 4.20 Layer configuration of the third design study. Left: Dark-colored layers represent TiO_2 while the gray-colored layers are SiO_2. The first and the last layers correspond to air and a silica substrate respectively. Right: Thickness distribution of the material layers. (The odd-numbered layers correspond to TiO_2 while the even-numbered layers are SiO_2 except the first layer which is the substrate.).

The sensor response was determined using the same approach that was performed also in the previous studies. The spectral configuration of two optical components shows four bandgap peaks as it was defined in the objective function. The sensor response shows about m=400 which is the highest value overall in the three design studies. Results are shown in Fig. 4.21.

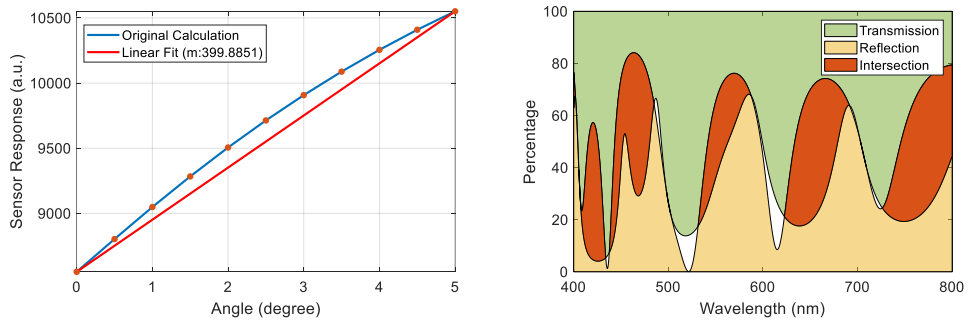

Figure 4.21 The optical configuration at the incident angle of 0°. Right: Change in the intersection area of the optical spectrum from 0° to 5°with the increment size of 0.5°.

4.3 Design of a Resonant Fabry Perot Structure

4.3.1 Abstract

This topic deals with the structural dynamic simulations of a both-end-fixed beam design which aims to detect high-frequency vibrations in an environment using the sensing approach that was introduced in Chapter 1. In this design, the cavity layer was designed as void while two-cavity supports were employed to contribute single-degree-of-freedom behavior of the structure. Similar to the sensing idea that was introduced in Chapter 1, a Fabry Perot cavity was designed using two Bragg layers where one of which is aimed to have a relatively thinner substrate to show resonant behavior. A more detailed concept design is illustrated in Fig. 4.22.

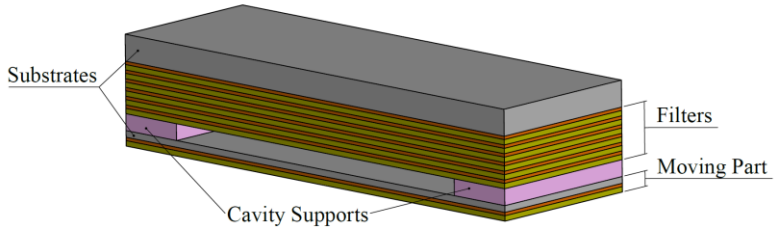

Figure 4.22 Concept design of a Resonant Fabry Perot Structure

In this context, the details of the design objectives are summarized as follows:

- The design intends to obtain both ends fixed, single-degree-of-freedom structures where the resonance frequency can be tuned via designing the geometry of the moving part such as; width, length, thickness, and substrate material.
- The moving part is connected to the second Bragg filter through two fixed cavity supports. These supports can be fabricated through a straightforward micromachining process using PMMA material.
- In this sensing approach, the moving part is expected to have a thinner total thickness thus also the rigidity, with respect to the rest of the structure.
- Apart from the moving part, the rest of the structure has a very wide range of design degrees of freedom in order to design the structure optically.

4.3.2 Concept Design & Results

By taking into account these design considerations mentioned above, structural dynamic analysis of a concept design was conducted using the finite element method (FEM) via COMSOL Multiphysics. The cavity supports were chosen PMMA while the substrate and thin-film stack are both chosen SiO_2. The geometry of the simulation model and dimension parameters are given in Fig. 4.23 and Table 4.1, respectively.

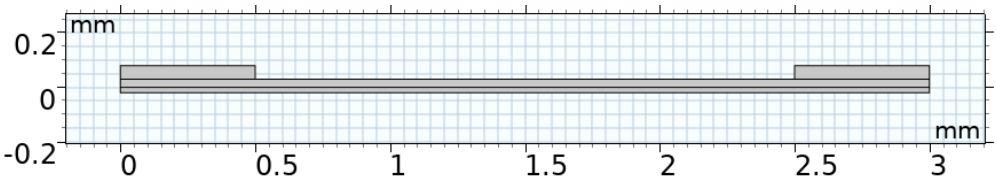

Figure 4.23 Sideview of a resonant Fabry Perot structure

Table 4.1 Dimensions of a concept designed of a resonant Fabry Perot structure

Moving Part Thickness	Cavity Thickness	Cavity Length	Cavity Depth
180 um	50 um	2 mm	3 mm

In order to understand the structural dynamics of the concept design, two simulation studies were performed: eigenfrequency analysis and frequency domain analysis.

Firstly, the eigenfrequency analysis was performed to investigate the model behavior of the structure. The first three modes and mode shapes of the structure were calculated. Results of the mode shapes and mode frequencies are given in Fig. 4.24, Fig. 4.25, and Fig. 4.26.

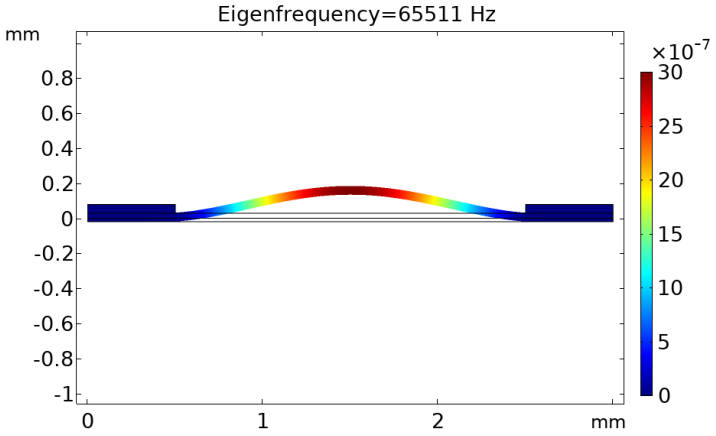

Figure 4.24 First mode shape about 65 kHz

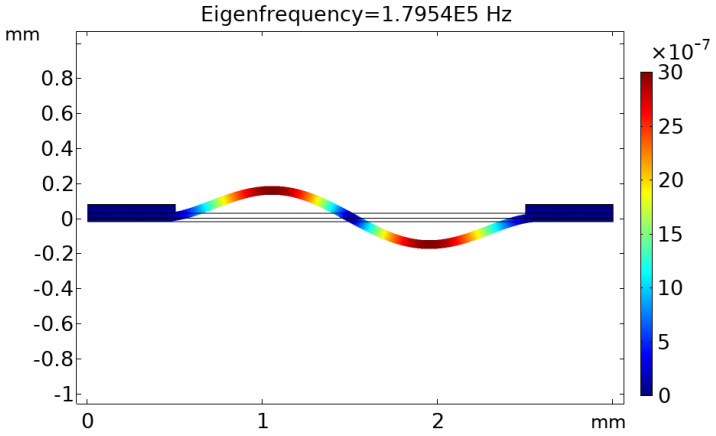

Figure 4.25 First mode shape about180 kHz

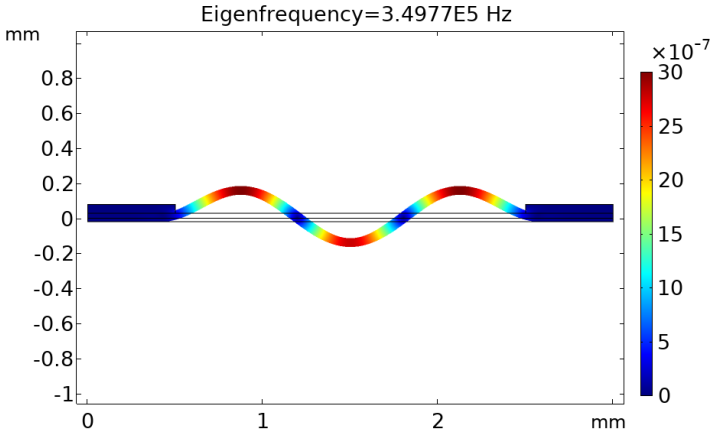

Figure 4.26 First mode shape about 350 kHz

Moreover, in order to see the frequency response of the structure and to calculate the displacement amplitude under periodic excitation, frequency response analysis was performed. More in detail, 1 N sinusoidal force was applied to the structure and the steady-state response of the structure was calculated by performing a homogenous solution for a second-order linear nonhomogeneous differential equations. A consistent Rayleigh damping value was used which was taken from the literature [10],[11]. Frequency response is shown in Fig. 4.27.

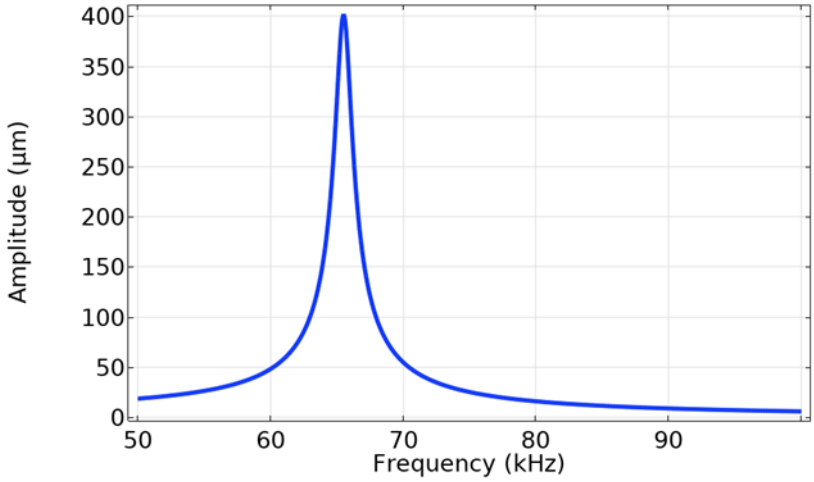

Figure 4.27 Frequency response of a resonant Fabry Perot structure

4.4 Frequency Tuning of the Sensor Analyzed in Chapter 2

4.4.1 Abstract

This part presents additional work for the sensor structure that was introduced in Chapter 2. In this work, frequency tuning of the sensor structure was investigated by changing the membrane geometry and the membrane material. The change in the sensor response was investigated through simulation work using COMSOL Multiphysics. Outlines of this study can be listed as follows:

- A new contact layer was designed that can work at 50kHz and above.
- The contact layer material was designed as 10 mm of diameter and 1.5 mm thickness made by a PMMA material.
- The new contact layer shows plate characteristics instead of a membrane that was given in Chapter 2.
- Eigenfrequency analysis and frequency response analysis were performed.

4.4.2 Contact Layer Design & Results

The new contact layer was designed to achieve above-50 kHz working frequencies. For this purpose, the contact layer dimensions and the material were redesigned. Thus, a PMMA contact layer with 5 mm of radius and 1.5 mm of thickness was employed in the new design (Fig. 4.28).

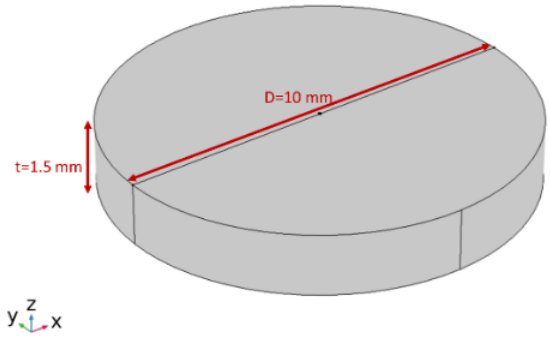

Figure 4.28 Dimensions of a new contact layer made by PMMA

Firstly, an eigenfrequency analysis was performed to determine the resonance frequency of the contact layer. The first three mode shapes and the frequency values are given in Fig. 4.29. Fig. 4.30 and Fig. 4.31 respectively.

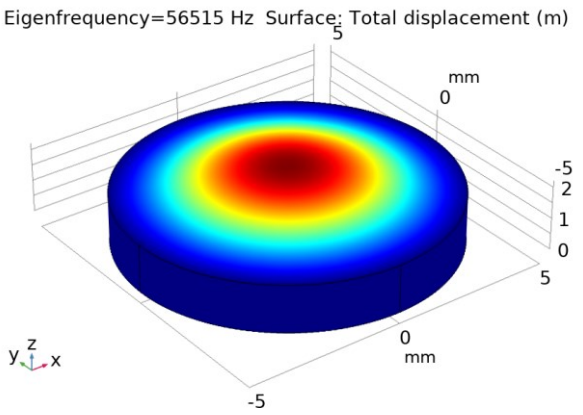

Figure 4.29 First mode shape about 56 kHz. (Also known as 0.1 mode).

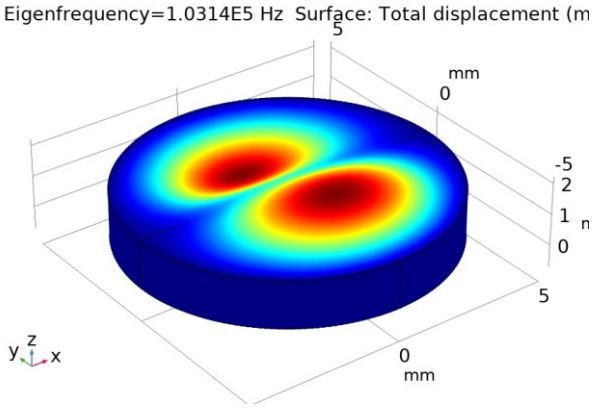

Figure 4.30 Second mode shape about 103 kHz. (Also known as 1.1 mode).

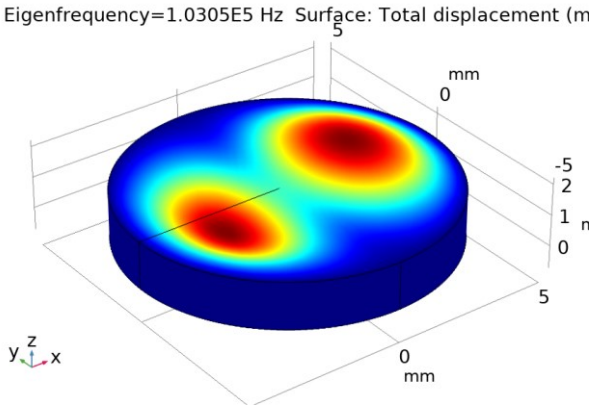

Figure 4.31 Third mode shape about 103 kHz (symmetric of the second mode) (Also known as 1.1 mode).

Moreover, to determine the frequency response of the structure and to calculate the displacement amplitude under harmonic excitation, frequency response analysis and also time response analysis were performed. A consistent Rayleigh damping value was used which was taken from the literature [10],[11]. The frequency response curve of the contact layer is shown in Fig. 4.32.

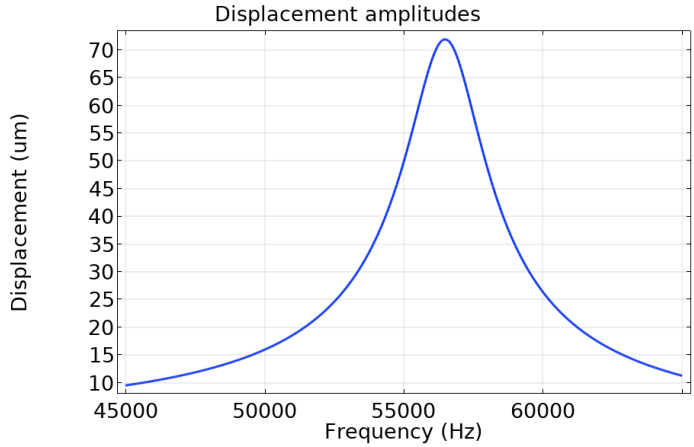

Figure 4.32 Frequency response curve of the PMMA contact layer.

In addition to that, a time-domain analysis was performed to investigate the transient response behavior of the contact layer. In this respect, a sinusoidal input force was applied to the contact layer through 8.8 µs. The input force is given in Fig. 4. 33.

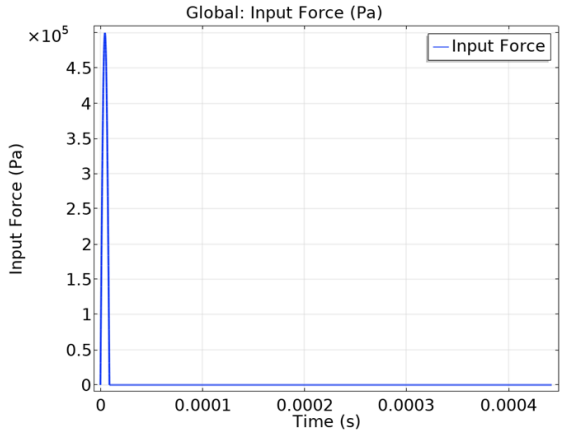

Figure 4.33 Input force profile

The transient response of the contact layer was simulated for 50 ms and the displacement curve is given in Fig. 4.34.

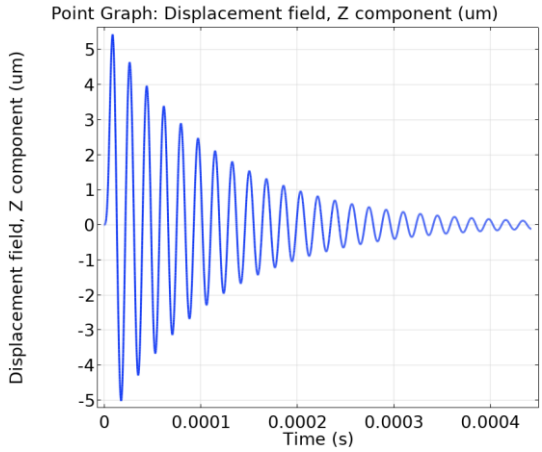

Figure 4.34 Transient response of the contact layer.

Fast Fourier Transform (FFT) analysis of the transient response of the contact layer is shown in Fig. 4.35. A resonance peak around 56 kHz is observed. It is worth noting that the displacement values are extracted from the geometric center of the contact layer only. Therefore, the FFT results represent the first mode response only.

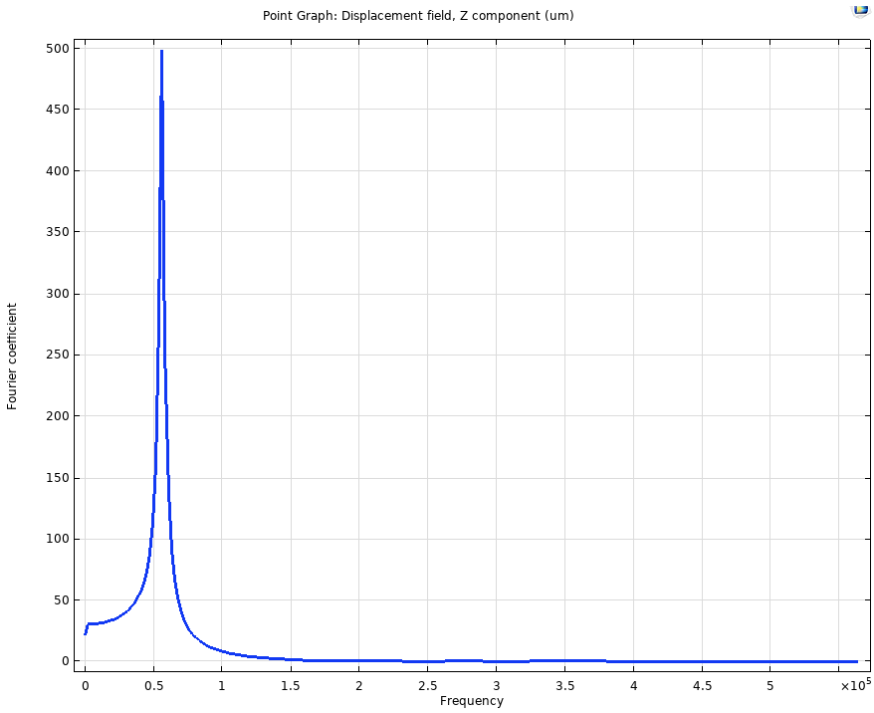

Figure 4.35 FFT of the transient response of the contact layer.

In addition to that, a further analysis was performed to see the sensor performance while it is mounted on a structure. Therefore, a full sensor including all components was installed on a steel beam and the contact layer response of the sensor was investigated. The sensor installation on a steel beam is shown in Fig. 4.36. The steel plate was modeled with a periodic boundary condition at the edge of a finite material domain, to avoid elastic wave reflection back due to the excitation.

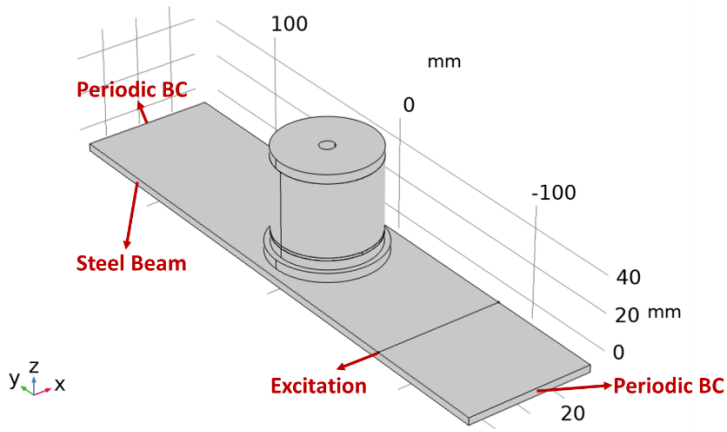

Figure 4.36 Sensor installation on a steel beam.

The time-domain response of the structure was simulated through 50 µs simulation time. The time-domain response of the structure is shown in Fig. 4.37.

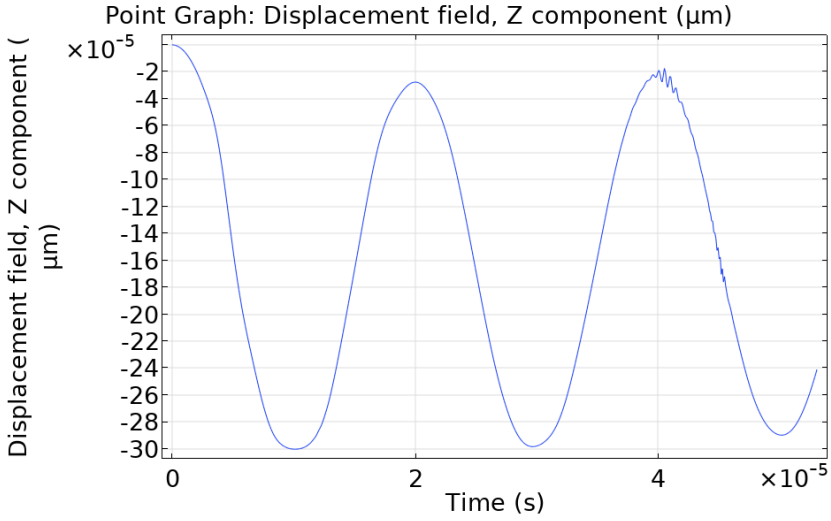

Figure 4.37 Time-dependent response of the contact layer.

Moreover, FFT analysis of the time domain response shows the frequency response of the contact layer. FFT analysis of the time domain response is shown ins Fig. 4.38.

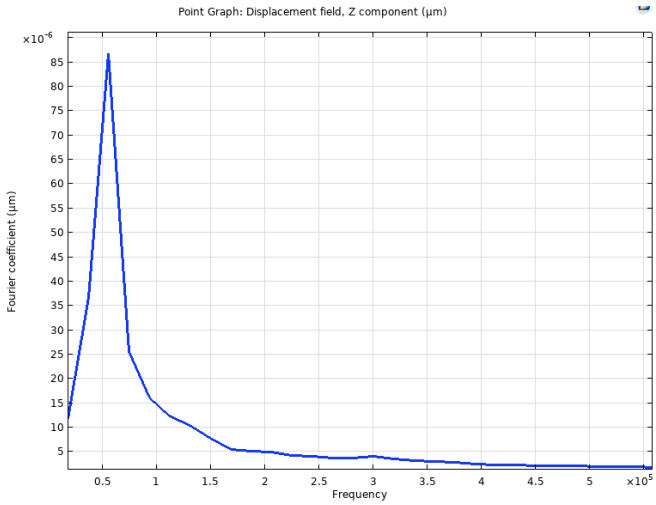

Figure 4.38 FFT analysis of the time domain response in Fig. 4. 37

To conclude up, the frequency response of the sensor can be designed by changing the contact layer. Different dimensions and materials can enable to calibrate of the sensor frequency for different applications. However, it should be also noted that the sensitivity of the structure mostly relies on the optical components. Therefore, the design of the optical components also plays a crucial role for different frequency applications. In particular, high frequency (ultrasound) elastic waves experience a high amount of attenuation. Therefore, the amplitude of these signals may not show a significant displacement through the contact layer. But a well-tuned optical component can overcome this issue. In order to design the optical components properly for a specific application, the design and optimization framework would be beneficial which was introduced in Chapter 4.2.

References

[1] G. Carta and M. Brun, “Bloch-Floquet waves in flexural systems with continuous and discrete elements,” Mech. Mater., vol. 87, pp. 11–26, 2015.

[2] G. Carta, M. Brun, A. B. Movchan, and T. Boiko, “Transmission and localisation in ordered and randomly-perturbed structured flexural systems,” Int. J. Eng. Sci., vol. 98, pp. 126–152, 2016.

[3] S. Larouche and L. Martinu, “OpenFilters: open-source software for the design, optimization, and synthesis of optical filters,” Appl. Opt., vol. 47, no. 13, p. C219, 2008.

[4] D. M. Topasna and G. A. Topasna, “Numerical modeling of thin film optical filters,” Educ. Train. Opt. Photonics, no. October, p. EP5, 2009.

[5] G. F. Burkhard, E. T. Hoke, and M. D. McGehee, “Accounting for Interference, Scattering, and Electrode Absorption to Make Accurate Internal Quantum Efficiency Measurements in Organic and Other Thin Solar Cells,” Adv. Mater., vol. 22, no. 30, pp. 3293–3297, Aug. 2010.

[6] F. D. Ismail, M. S. Aziz, C. Teeka, J. Ali, and P. P. Yupapin, “Filter design using multi-bragg reflectors,” World J. Model. Simul., vol. 8, no. 3, pp. 205–210, 2012.

[7] S. Guldin, “Inorganic Nanoarchitectures by Organic Self-Assembly,” vol. 19, pp. 19–33, 2013.

[8] Y. G. Boucher, J. Le Rouzo, I. Ribet-Mohamed, and R. Haïdar, “Modified form birefringence in periodic multilayer structures including uniaxial anisotropic materials,” J. Opt. Soc. Am. B, vol. 25, no. 5, pp. 777–784, May 2008.

[9] M. Bellingeri, A. Chiasera, I. Kriegel, and F. Scotognella, “Optical properties of periodic, quasi-periodic, and disordered one-dimensional photonic structures,” Opt. Mater. (Amst)., vol. 72, pp. 403–421, 2017.

[10] C. P. Okeke, A. N. Thite, J. F. Durodola, N. A. Fellows, and M. T. Greenrod, “Modelling of hyperelastic polymers for automotive lamps under random vibration loading with proportional damping for robust fatigue analysis,” in Procedia Structural Integrity, 2018, vol. 13, pp. 1460–1469.

[11] Okeke, C. P., Thite, A. N., Durodola, J. F., & Greenrod, M. T. (2019). Fatigue life prediction of Polymethyl methacrylate (PMMA) polymer under random vibration loading. Procedia Structural Integrity, 17, 589–595. https://doi.org/10.1016/j.prostr.2019.08.079

Summary, conclusions and future perspectives

Summary

This thesis presents the outcomes of an interdisciplinary research work focusing on the development of optomechanical sensors for vibration detection and in future acoustic emission applications. In this context, the thesis content consists of four research chapters; where each of the first three chapters is intended to be published as a journal article while the fourth chapter covered four supplementary topics to explain the thesis content more in detail.

The first chapter of the thesis presented a sensing scheme using Fabry Perot Interferometry. Fabrication, modeling, and assessment steps of an elastic cavity-based sample were introduced. The displacement in the thickness of the elastic cavity layer due to the static loadings was determined experimentally, as a change in the optical spectrum through the spectrophotometer measurements. The outcome of this research work was published in Ceramics International with the title *Fabrication, Modelling, and Assessment of Hybrid 1-D Elastic Fabry Perot Microcavity for Mechanical Sensing Applications.*

Further research and fabrication afford for implementation of this Fabry Perot structure also for detection of vibration changed the direction of the research into an innovative fabrication technique that enabled the deposition of thin-film optical filters on flexible substrates. Thus, that development gave a birth to new sensing method based on flexible optical components.

In the second chapter, a new optical sensing approach based on tunable spectral filters using flexible optical components was presented. An extended work in analytical modeling, simulation, design, and realization of a proof-of-concept sensor was demonstrated. Furthermore, characterization studies were shown to determine the static and dynamic response of the proof-of-the-concept device. The result of this research work was submitted in Optical Materials with the title: *Design, Fabrication and Assessment of an Optomechanical Sensor for Pressure and Vibration Detection using Flexible Glass Multilayers*.

All of the research work that is mentioned above aims to contribute to the development of a future acoustic emission sensor that can be a replacement for current PZT commercial sensors. Thus, the understanding of the current sensor technologies applyed through the real-world problems plays an important role in new device developments.

Therefore, the third chapter of the thesis presented seismic vulnerability analysis of a coupled tank-piping system using traditional PZT acoustic emission sensors for the detection of the most vulnerable components. A methodology based on a stochastic seismic ground motion model, hybrid simulation, and acoustic emission studies were demonstrated. The real-time acoustic emission monitoring of a tank-piping system is presented. Deformation levels of each vulnerable component were investigated. Processing of acoustic emission signals provided a more in-depth view of the damage level of the analyzed components. The result of this research work was published in Experimental Techniques with the title: *Seismic Vulnerability Analysis of a Coupled Tank-Piping System by Means of Hybrid Simulation and Acoustic Emission*.

The last part of the thesis presented four supplementary topics to contribute to the overall thesis and provide a deeper understanding of some subjects.

In the first topic, the theory and mathematical derivation of the transfer matrix method (TMM) were covered; they are widely used in this thesis for the modeling of thin-film optical filters.

In the following topic, an optimization framework was introduced by integrating TMM simulation into the Genetic algorithm. In this framework, an automated design process was demonstrated for finding a proper design configuration to exhibit a specific optical response. This topic covered three different case studies for a different types of applications including sensor development.

The third topic showed a structured design as the continuation of the sensor study that was demonstrated in the first chapter. A resonant Fabry Perot structure was designed and its structural dynamics response was investigated through finite element simulations. It was found that the working frequency of the structure can be increased by tuning the dimension parameters. Therefore, frequency values in the ultrasound range (above 20 kHz) can be achieved through that structure.

In the last topic, the frequency tuning was performed for the prototype device that was given in the second chapter. Dimensions and the material properties of the contact layer were designed to reach a higher frequency value. The structural dynamics behavior of the contact layer was investigated through simulations. In addition, the sensor performance mounted on a structure was also simulated. This work provided an idea for future development and implementation of the sensing approach in the second chapter.

Conclusions and Future Prospective

Acoustic emission technique is an effective tool to determine the structural health status of components in constructions such as bridges, railways, pipelines, pressure vessels, etc. With the help of real-time detection capabilities, the acoustic emission technique can avoid catastrophic events and save lives, time, and money. Thus, all of these benefits increase the popularity of the acoustic emission technique. In addition, the development of new sensing strategies for acoustic emission applications, in particular exploiting the optical sensing methods, can extend the variety of acoustic emission applications. Thus, in this thesis, the use of current acoustic sensors, as well as the development of new optical sensing approaches were presented for acoustic emission applications. In this respect, the achievements of the thesis can be summarized as follows:

In the first chapter.

i. A mechanical sensor consisting of 1-D photonic crystals was designed and fabricated using radio frequency sputtering. A wet fabrication protocol was developed and PDMS-based on an elastic microcavity layer was sandwiched between two equivalent Bragg reflectors.
ii. The Transfer Matrix Method simulations were performed for both the single Bragg and the sandwich sample by taking into account the wavelength-dependent refractive indices of the materials. The Transfer Matrix Method simulations and transmission measurements showed good agreement.
iii. The sandwich sample was tested under varying loading conditions. The optical response of the sample was studied as a function of the applied forces. The transmittance response of the sandwich structure showed that cavity peaks shift to higher wavelengths and increase their intensity due to an increase of applied force. This effect took place due to both changes in elastic microcavity thickness and change of PDMS refractive index. The viscoelastic material properties of the PDMS influenced the system response due to loading removal.
iv. This sensing approach can be applied for the detection of small-displacement changes at a nanometer scale. Thus, for future applications, fabrication of the elastic microcavity using different elastic materials would improve the sensing response of a structure.

In the second chapter.

i. An innovative sensing approach was introduced for force and vibration detection based on flexible photonic components.
ii. In order to fabricate the optical components, a fabrication protocol was developed through SiO_2/TiO_2 multilayers on a rigid, as well as a flexible substrate, using the RF-sputtering technique.
iii. The optical response of multilayers was evaluated using both the transfer matrix method simulations and spectrophotometer measurements. Optical microscopy and AFM measurements confirmed the good quality of the glass on the flexible substrates. No cracks were observed on the multilayer structure.
iv. A proof-of-concept optomechanical sensor was demonstrated using a flexible multilayer. The sensor performance was characterized by both static and dynamic conditions. It was found that the device is capable of detecting static loadings from 50 Pa to 235 Pa values. Moreover, the dynamic response of the sensor was detected at about 515 Hz by means of an impact test.
v. Additional analysis regarding the dynamic response of the sensor was also carried out through both analytical and finite element calculations.
vi. In order to couple mechanical deformations through the optical response, an optomechanical simulation framework has been developed. The interaction between the optical and the mechanical components was correlated by means of measurement data, geometric optics, transfer matrix simulations, and finite element analysis. Thus, the framework showed that the optomechanical response of the sensor device can be estimated through reliable simulations.
vii. In the future implementations of this work, the contact layer and optical parts can be designed together to reach very specific design objectives. More precisely, the wide design degrees of this system offers wide bandwidth detection applications.
viii. The given innovative fabrication technique on flexible optical components offers a broad range of application scope, including wearable sensing applications, integration of optical sensors through curved structures, etc. For this reason, investigation of the mechanical properties of the thin film coating would be beneficial for the mechanical reliability of future applications. In particular, nanoindentation studies can provide a deeper understanding of the film properties of the samples. In addition to that, bending tests can help to predict the lifetime and quality of structures.

In the third chapter.

i. A methodology is presented which is capable of assessing the vulnerability characteristics of a realistic tank-piping system based on hybrid simulation, synthetic ground motions, and acoustic emission analysis. In particular, the main focus was on the performance of vulnerable components of the piping network.
ii. As a first step of the study, a seismic scenario was considered that is associated with a geographical site using a probabilistic seismic hazard analysis. On this basis, the seismic input was identified by means of a stochastic ground motion model. In addition, in order to reach the collapse limit state of the piping system, a monotonic loading case was also considered.
iii. Throughout all the loading experiments, acoustic emission detection and damage localization were carried out. The performance evaluation of critical components based on acoustic emission events; the Tee joint resulted to be the most damaged component for the hybrid simulation case whilst Elbow #2 was the most damaged component for the monotonic case.
iv. The acoustic emission technique provided information to obtain more in-depth information about the damage level of critical components as well as the plasticity level of the piping system. This opens the way to collect a library of acoustic emission events for the classification of vulnerable components and to refine our FE models for future studies.
v. In future studies, investigation of the wave profile of each acoustic emission signal combined with trending machine learning approaches would reveal deeper information regarding the health status of the structures for predictive maintenance purposes.

In the fourth chapter.

i. The physical background of thin-film optical filters is reviewed and the mathematical derivation of the Transfer Matrix Method is presented. A programming scheme was developed supporting wavelength-dependent material properties, incident angle modifications, and complex refractive indices. The code structure was also constructed in the way of designing periodic as well as arbitrarily distributed layers.
ii. An automated design framework for thin-film optical filters is presented using a Generic algorithm together with a transfer matrix model. In total, three different types of design problems were addressed. A particular objective function was investigated for each design problem.
iii. The objective functions were tuned to determine the best combination of the design parameters which are layer thicknesses, material type, number of layers, layer distributions.
iv. As a supplementary design to the sensing approach given in Chapter 1, a both-end-fixed beam design was proposed. This structure was presented to detect high-frequency signals. Finite element simulation was performed to investigate the structural dynamics of the structure. A design for 65 kHz was demonstrated.
v. Another supplementary work was performed to the second sensing idea that was discussed in Chapter 2. A contact layer was designed to detect high-frequency signals. FE simulations were performed to investigate the dynamics properties of the structure. A design for 55 kHz was demonstrated.
vi. Overall, the given design framework in Subsection 4.2. showed promising results for the application of this framework to the development of future optical applications.
vii. The future developments in this framework, by taking into account not only the optical but also the thermal and mechanical behaviors, can enable the potential to design superior structures. In order to contribute the design efforts in metamaterial concepts, the design scope can be even extended by considering not only 1D but also 2D and 3D design approaches.

ISBN (paper): ..... ; ISBN (online): .....

University of Trento

Doctoral School in Civil, Environmental and Mechanical Engineering

http://web.unitn.it/en/dricam

Via Mesiano 77, I-38123 Trento

Tel. +39 0461 282670 / 2611 - *dicamphd@unitn.it*